ABSTRACT

Title of Dissertation: INDIUM PHOSPHIDE BASED
OPTICAL MICRO-RING RESONATORS
Rohit Grover, Doctor of Philosophy, 2003

Dissertation directed by: Prof. Ping-Tong Ho
Department of Electrical and
Computer Engineering

Micro-ring resonators are a strong candidate for the basic building blocks of very-large-scale-integrated optics. They can be used in many applications, such as filters, routers, switches, lasers, and amplifiers. They are simple in design and concept, can be made very small, and do not require exotic materials or fabrication techniques. In this thesis, I describe my work on indium phosphide based active and passive micro-ring resonators. To enable low-loss devices, I develop a dry-etching process for InP using the methane chemistry in a capacitively-coupled reactive-ion-etching machine. Using the etch process, I demonstrate single-mode micro-ring resonators in the vertically- and laterally-coupled geometries, all-optical logic, and a tunable micro-ring notch filter. The best devices in the vertically-coupled geometry have bandwidth as low as 0.24 nm, free spectral range of 24 nm, $Q = 6200$, and finesse of 100 while the laterally-coupled micro-rings have bandwidth as low as 0.25 nm, free

spectral range of 8 nm, Q = 6250, and finesse of 32. Some of the laterally-coupled devices have free spectral ranges as high as 28 nm, though the corresponding Q is low. In collaboration with Tarek Ibrahim, I demonstrate all-optical logic (AND operation) using carrier-induced refractive index change by two-photon-absorption with switching speed of 100 ps, dominated by ambipolar diffusion. Finally, I demonstrate tuning by 100 GHz (0.8 nm) with 8 V reverse bias of an InP-based micro-ring resonator with a p-i-n structure using the quadratic electro-optic effect, obtaining 1.5 GHz/V^2 of tuning.

INDIUM PHOSPHIDE BASED OPTICAL MICRO-RING RESONATORS

by

Rohit Grover

Dissertation submitted to the Faculty of the Graduate School of the
University of Maryland, College Park in partial fulfillment
of the requirements for the degree of
Doctor of Philosophy
2003

Advisory Committee:

Prof. Ping-Tong Ho, Chair
Professor Reza Ghodssi
Professor Julius Goldhar
Professor Wendell T. Hill, III
Doctor Kenneth J. Ritter
Doctor Marshall Saylors

Into the great wide open
Under them skies of blue
Out in the great wide open
A rebel without a clue

– *Tom Petty, "Into the Great Wide Open"*

DEDICATION

To Priya

ACKNOWLEDGMENTS

I thank my advisor, Prof. Ping-Tong Ho, who has been a patient guide these past few years, and has bought me many meals. Of the management and staff at the Laboratory for Physical Sciences, I am especially grateful to L. Calhoun, J. B. Dottellis, R. Frizzel, D. Hinkel, S. Horst, F. Johnson, S. Kanakaraju, O. King, R. Krause, L. Lorenz, L. Lucas, L. Olver, B. Preston, M. Saylors, F. Seiferth, and K. Ritter. My co-workers have been key to this work, particularly P. Absil, K. Amarnath, T. N. Ding, J. Hryniewicz, T. Ibrahim, L.-C. Kuo, Y. Leng, and V. Van. Thanks are also due to my external collaborators, A. Bleier and J. Treichler (CNF), M. Raburn (UCSB), and Y.-S. Lee and D. Lishan (Unaxis). Finally, and most importantly, I owe a debt of gratitude to my family - Mummy and Papa, for all their love and support over the years, my brother Ranjan, and my wife Priya - and many friends, who groaned at my jokes, and generally made life pleasant.

This work was supported by a Distinguished LPS-ECE Graduate Research Assistantship, a Graduate Student Fellowship from the IEEE's Lasers and Electro-Optics Society, and many loans from friends and family.

TABLE OF CONTENTS

LIST OF FIGURES

CHAPTER 1

INTRODUCTION

Micro-ring resonators are promising as the building blocks for future very-large-scale-integrated photonics. They can be used for diverse applications such as optical channel dropping filters (OCDFs), optical add/drop (de)multiplexers (OADMs), switches, routers, logic gates, lasers, and amplifiers. Although they are functionally similar to Fabry-Perot resonators, they do not require any on-chip facets. Unlike Fabry-Perot OCDFs, the reflected waves, and input waves in ring resonator OCDFs are separate (they are on different bus waveguides). Their small size means that many devices can be integrated on the same chip, making all-optical signal processing a possibility.

In this thesis, I will discuss the fabrication of passive and active InP-based single-mode micro-ring resonators. I will describe my work on indium phosphide based active and passive micro-ring resonators. I have demonstrated the first single-mode vertically-coupled micro-ring resonators in the InP system, the smallest ring resonators in any material system with laterally-coupled InP-based microring resonators, all-optical logic with InP-based micro-rings, and a tunable ultra-compact InP micro-ring notch filter.

The thesis is organized as follows: in this chapter, I will introduce the topic of ring resonators, after which I will go over the theory and the technology developed for this project. Next, I will discuss my work on the two geometries for passive micro-ring fabrication, followed by my work on active micro-rings.

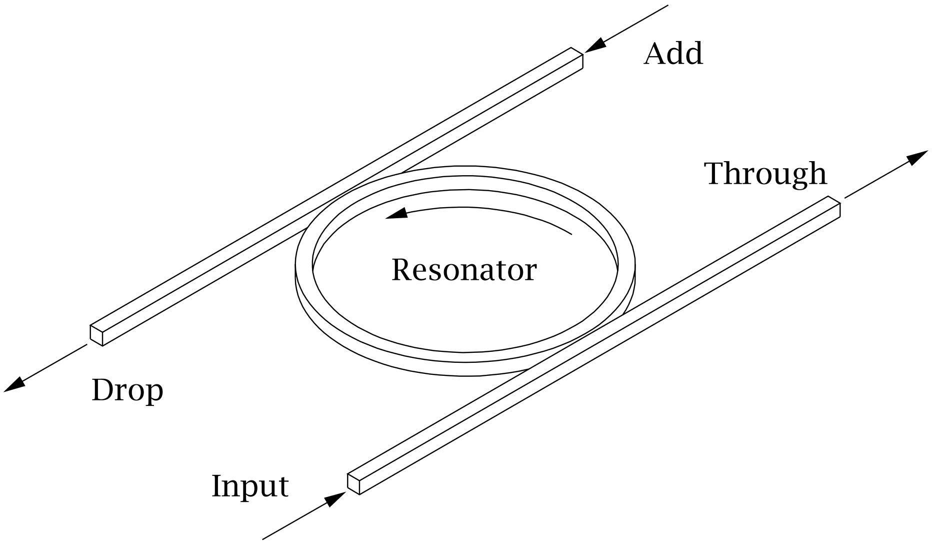

Figure 1.1: Schematic of an optical ring resonator add/drop filter.

Finally, I will present a summary of my work.

1.1 Ring resonators

A ring resonator consists of a waveguide in a closed loop. The loop can be any closed shape, such as a circle, ellipse, or racetrack. The ring is placed near one or two bus waveguides (Fig. 1.1). Typically, the input signal consists of one or more WDM channels. Signals on the input bus couple evanescently to the resonator. If a channel wavelength is resonant in the resonator, i.e., it encounters an integral multiple of 2π in phase over a round-trip, the signal intensity builds up in the ring, it couples to the output bus, and is “dropped.” At the same time, a signal on the same wavelength can be added via the add port. The resonator thus functions as an add/drop multiplexer. Similar functionality can be obtained by using a disk instead of a ring; however, disk resonators are typically multi-mode, which limits their usefulness.

1.2 Historical perspective

Disk and ring resonators for the microwave regime have been discussed and analyzed since the early 1960s. The analog of a disk resonator in acoustics was observed and analyzed (with the wave approach) as early as 1910 by Lord Rayleigh [1]. Integrated optical ring resonators were proposed in 1969 by Marcatili at Bell Labs [2]. Since then integrated optical ring, disk, and spherical resonators have been made in many material systems. In addition, several research groups have worked on ring resonators made with discrete components.

The first optical ring-resonator was demonstrated by Weber and Ulrich in 1971 [3–5]. Weber and Ulrich's device consisted of a 5 mm diameter glass-rod ($n = 1.47$) coated with Rhodamine-6G-doped polyurethane ($n = 1.55$), for a resonator circumference of 31.4 mm. They coupled light into and out of it with a prism. By pumping the polymer with light from a N_2 laser ($\lambda = 337.1$ nm), they obtained laser operation. The chief drawback of their device was the large size and the use of prism coupling, rendering it unsuitable for integrated optics.

The next demonstration was by Haavisto and Pajer in 1980 [6]. Their device was the first to incorporate integrated bus waveguides, and was made with a doped poly(methyl methacrylate) film on quartz substrate. A significant feature of their work was that the device was fabricated without lithography by using direct-writing with a 325 nm He-Cd laser. Although they demonstrated low-loss waveguides and rings, the ring was quite large (circumference 28.3 cm). Also, while the coupling to the ring was via evanescent coupling to integrated bus waveguides, the coupling to the bus waveguides was through prism couplers, probably because it is difficult to achieve good facets when cleaving quartz substrates.

In 1982, Stokes, Chodorow, and Shaw [7] demonstrated the first fiber ring-resonator, operating at $\lambda = 632.8$ nm. Fibers do not lend themselves to compact integrated optics; their resonator had a circumference of 3 m.

Between 1982-1990, numerous groups demonstrated ring resonators based on glass. Early efforts used ion-exchange from $AgNO_3$, KNO_3 and similar compounds, which modifies the index of the glass, to make the waveguide core. Walker and Wilkinson demonstrated a ring resonator with silver-ion exchanged glass in 1983 [8] (circumference 3.1 mm, operating at $\lambda = 632.8$ nm), as did Mahapatra and Connors in 1986 [9, 10] (circumference of 4.1 mm, operating at $\lambda = 632.8$ nm). Honda, Garmire, and Wilson demonstrated a ring-resonator with potassium-ion exchanged glass in 1984 [11] (circumference 25.1 cm). A related effort by Naumaan and Boyd, 1986 [12] used CVD phosphosilicate glass films. The common feature of the demonstrations cited above was the size of the ring: much larger than the small sizes (circumferences of tens of μm) required for large-scale optical integration.

Other efforts used Ti-exchanged $LiNbO_3$ (Tietgen, 1983 [13]), and proton-exchanged $LiNbO_3$ (Mahapatra and Robinson, 1985 [14]). Tietgen's work is especially significant as it represents the first demonstration of a tunable ring resonator. Instead of a circular ring, he used a waveguide loop with two 3 dB couplers. His device used electro-optic tuning, had a circumference of a little over 24 mm, and operated at $\lambda = 790$ nm.

Since the early efforts outlined above, there have been numerous works in various doped and undoped silica-based glasses [15–25], Si-(Si_3N_4, SiON, SiO_2) [26–37], and polymers [38–41] in the past decade. Many of these have reported multi-ring filters, temperature-insensitive operation, etc. Of these, Oda's work with TiO_2-doped silica-glass rings represents the first demonstration of serially cascaded rings, with increased FSR over single-ring devices. Rabiei's work with polymer rings represents the first passive and active polymer ring resonator; however, his active rings are extremely large.

III-V micro-ring resonators are quite new; the first GaAs-AlGaAs micro-ring resonator was demonstrated by Rafizadeh et al. in 1997 at Northwestern University, Evanston, IL [42, 43]. Their smallest ring had a circumference of 32.8 μm. Since then, Hryniewicz, Absil, and co-workers at the Laboratory for Physical Sciences (LPS), College Park, MD, have demonstrated laterally and vertically coupled rings in GaAs-AlGaAs with similar circumferences; more significantly, they have demonstrated multi-ring devices, switches, routers, and mux/demux operation [44–52].

Several groups have demonstrated optically-pumped micro-disk lasers in both GaInAsP-InP and III-Nitrides using the whispering-gallery; the smallest reported disks had circumferences of ~ 15 μm [53–61]. However, most early efforts did not incorporate bus waveguides and relied on fibers to directly collect light from the disk.

The GaInAsP-InP material system has proved problematic for passive micro-rings because of processing problems; in active devices, chip losses can be compensated by incorporating gain. The first vertically-coupled passive InP-based rings were demonstrated by our group [50, 62, 63] (chapter 4). Other groups have concentrated on disk resonators; the group at University of Southern California has demonstrated active and passive vertically-coupled micro-disk resonators [64, 65]. However, disk resonators are inherently multi-mode, which limits their usefulness as filters.

The lateral-coupling approach in III-V semiconductors usually requires e-beam lithography, or multi-mode interference couplers. In 2000, Griffel and co-workers at Sarnoff Corp., Princeton, NJ, and Riverside Research Institute, New York, NY, demonstrated a laterally-coupled ring laser with integrated bus waveguides with stepper lithography by employing a bi-level etching technique [66], and demonstrated devices with circumferences of 1000 μm or more. In 2001, Rabus and co-workers at the Heinrich-Hertz Institute (HHI), Berlin, Germany, demonstrated MMI-coupled rings in GaInAsP-InP, and in 2002 they demonstrated active rings by integrating semiconductor optical amplifiers and on-chip platinum heaters [67–69]. The HHI work features very large ring circumference; their smallest rings had circumferences as large as 928 μm, which resulted in extremely narrow free spectral range (around 0.8 nm). Laterally coupled ring resonators in GaInAsP-InP were also demonstrated by Rommel and co-workers from University of Illinois, Urbana-Champaign, IL, and Sarnoff in 2002 [70]. They demonstrated a ring resonator with circumference 274.2 μm and free spectral range a little over 2 nm. Our group recently demonstrated micro-ring resonator notch filters, both passive and electro-optically tuned, with the smallest turning radius to date [71–73]. Our smallest device had a circumference of just 20.1 μm (an order of magnitude smaller than the smallest device previously reported), with a free spectral range much greater than 30 nm (chapters 5 and 7).

1.3 Putting the “micro” in “micro-ring”

A critical factor in the fabrication of small ring resonators is controlling the loss in the ring. Loss in micro-rings and pedestal waveguides comes from leakage to the substrate, scattering or contra-directional coupling due to surface roughness [74, 75], and bending [2, 76–78]. I will examine the origin of bending loss and its dependence on the lateral index contrast in the next chapter (section 2.1).

Scattering due to leakage to the substrate can be solved by waveguide design, and that from surface roughness can be solved with process improvements, such as high-resolution lithography, vertical photoresist sidewalls, and hard masks. However, bending losses are dictated by the choice of materials, and prescribe a minimum size for ring resonators in a material system, so there is no way of getting around them short of changing the choice of materials. The index contrast which determines the minimum bending radius is that in the lateral direction (the plane of the ring). The cladding in the plane of the ring, for a pedestal waveguide, is air, a low-index polymer, like amorphous Teflon ($n = 1.33$) or benzocyclobutene ($n = 1.51$), SiO_2 ($n \sim 1.5$), spin-on glasses ($n \sim 1.5$), SiON ($n \sim 1.5 - 2.1$), or polyimides ($n \sim 1.7$). Since the core in the case of III-V waveguides typically has a refractive index > 3, the minimum bend radius possible is < 1 μm, and bending losses are rarely a concern, if ever. The origin of bending loss is examined in the next chapter.

Initial efforts toward the fabrication of integrated ring resonators produced very large devices because the index contrast, Δn, between the core and cladding was small, and a large radius of curvature minimizes bending losses [2, 76–78]. For example, the device fabricated by Honda et al. had $0.052 < \Delta n < 0.067$, and a radius of 4.5 cm [11]. Also, the device was multimode, and there was considerable mode mixing, leading to a large background of non-resonant light and the convolution of resonances from multiple modes.

To minimize bending losses, we require high index contrast pedestal waveguides, which are made with anisotropic etching. In addition, small ring resonators (few to tens of microns in size) require small coupling gaps fabricated lithographically or by material growth. In the past decade, many such technologies have reached maturity. The confluence of the many mature and maturing technologies has led to the demonstration of single-mode micro-ring resonators laterally or vertically coupled to a bus waveguide in GaAs-AlGaAs and Si-SiO$_2$ [21, 42]. Advanced functions, such as high-order filtering for dense wavelength division multiplexing applications, notch filters and wavelength-selective mirrors, have been demonstrated [46, 48, 51]. In particular, Absil et al. demonstrated a 1×4 MUX/DEMUX in GaAs-AlGaAs [49]. They are promising building blocks for very large-scale integrated optics because of their small size, which will allow the integration of signal processing and logic functions on one chip.

1.4 Coupling approaches

Optical ring resonators require a way to couple light in and out. This is accomplished by evanescent coupling to bus waveguides in close proximity. Ring resonators can be made with laterally (in-plane) or vertically (out-of-plane) coupled bus waveguides; in the former case, the device is referred to as a ‘laterally-coupled (micro-)ring resonator,’ while in the latter case, it is referred to as a ‘vertically-coupled (micro-)ring resonator’ (Fig. 1.2).

III-V semiconductor devices based on lateral coupling require the use of advanced fabrication technologies (high resolution e-beam lithography, facet-quality-dry-etching with etch rate independent of trench width) to achieve reproducible filter bandwidths and high dropping efficiencies. In the lateral coupling case, the separation between the waveguides and the ring, typically less than 0.3 μm, is achieved by e-beam lithography. E-beam lithography is affected by processing conditions (humidity, temperature), the age of the cathode, and time taken by the machine to be stable. These problems are exacerbated by the requirements of small gaps, which can be difficult to etch (section 3.14) making reproducible bandwidth and high dropping efficiency

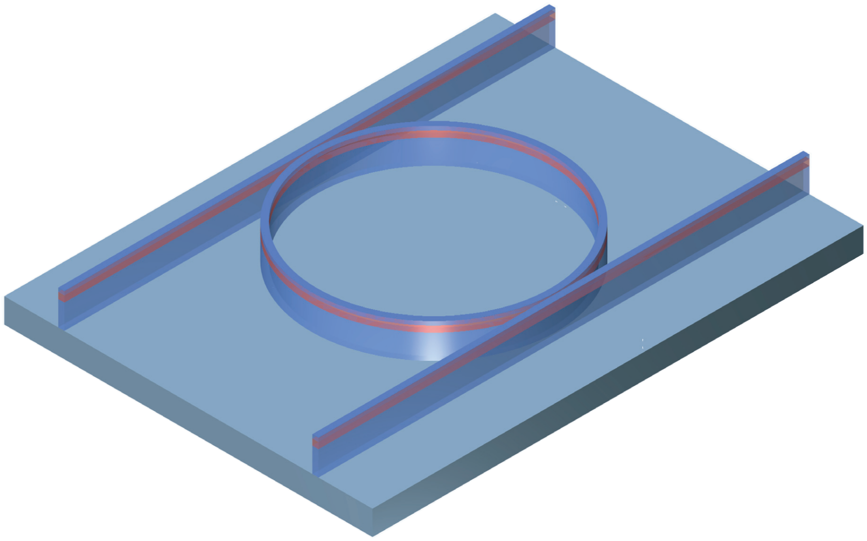

(a) Lateral coupling

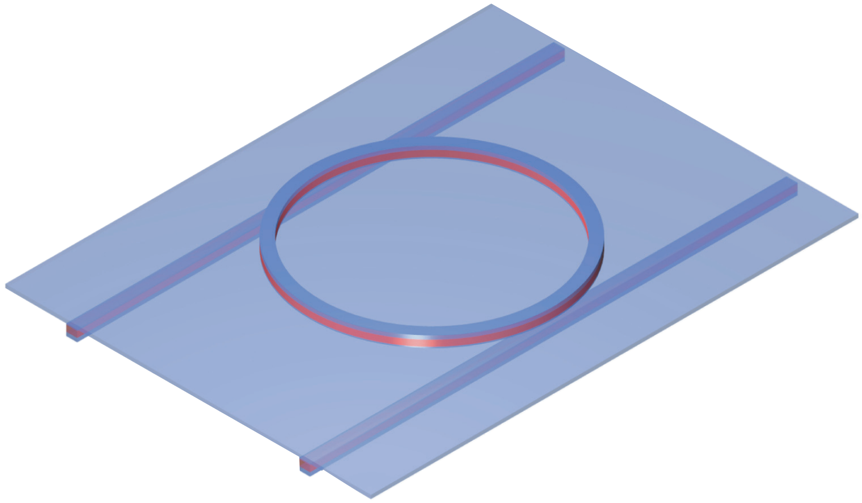

(b) Vertical coupling

Figure 1.2: Schematic of a micro-ring with (a) laterally, and (b) vertically coupled bus waveguides. The waveguide core is shown in red, and the cladding is blue.

difficult to achieve.

Vertical coupling is a better way to couple from the micro-ring resonator to the waveguide, as it can be done with standard optical lithography. In the vertical coupling approach, the coupling gap is defined by material growth or deposition. Further, the inherently symmetric structure with respect to resonator input and output coupling can result in better transfer efficiency, as demonstrated in glass with a process that requires redeposition and planarization [21]. Vertical coupling does require wafer bonding and growth-substrate removal, which can be a problematic step, and may limit yield in commercial applications by dictating a maximum size for void-free bonding. Wafer bonding can be achieved with polymers like benzocyclobutene or polyimides [79], planarization followed by solders like Pb-Sn [80] Pd [81], Au-Sn [82], or Pd-In [83, 84], and wafer fusion [85]. The use of solders and wafer fusion provides a conducting interface, which is advantageous for active devices, as contacts can be made to the (doped) substrate.

Laterally-coupled ring resonators remain important for integrating active and passive devices on the same chip. By combining the vertical- and lateral-coupling approaches, all the passive elements can be made with lateral coupling on the same layer as the bus, and the active elements can be coupled to the bus vertically.

1.5 Active rings

Most devices demonstrated so far have been passive. Passive devices can function only at certain wavelengths, which cannot be changed once the device has been fabricated. This is a serious limitation, because it isn't always possible to fine-tune the fabrication process for the exact filter wavelength.

Even small variations (tens of nm) in waveguide width can affect the resonance wavelength.

However, if it were possible to modify the wavelength of operation after fabrication – say, when the device is part of an optical network – we could compensate for fabrication errors. We will be able to change the wavelength of operation to match the desired wavelength. Also using gain and loss modulation, we could use the devices as switches, amplifiers, and routers. So active micro-ring resonator-based devices are an important topic of research.

The first active ring resonator was demonstrated by Tietgen in 1984 [13]. Since then, Rabiei et al. have demonstrated active polymer ring resonators [40], Rabus et al. have demonstrated active GaInAsP-InP ring resonators [69], and Grover et al. have demonstrated active GaInAsP-InP micro-ring resonators [73].

1.6 III-V semiconductors for active and passive micro-rings

III-V semiconductors have high refractive indices (> 3) compared to competing material systems such as glass/silica (~ 1.5), silicon oxynitride ($1.45 - 2.1$), and $LiNbO_3$ (~ 2.2). This allows the fabrication of very high (lateral) index contrast waveguides, which allows the bend radius to be as small as 1 μm before bending losses cause unacceptable deterioration in performance (sections 2.1 and 2.7).

Lattice matched III-V ternaries and quaternaries can be grown on both indium phosphide and gallium arsenide with a wide variety of bandgaps and refractive indices [86–91]. Using an appropriate choice of materials, we can make slab waveguides in both materials; patterning shallow-etched ridges produces loosely confined waveguides, and deeply-etched pedestals give us strongly confined waveguides. Since III-V semiconductors have been the subject of studies since the 1960s, there exists a vast body of knowledge on fabrication technologies such as chemo-mechanical polishing [92] and selective wet-chemical etching [93–95].

Most III-V compound semiconductors have a direct bandgap. Therefore, the waveguide core and/or cladding can be active, allowing us to make optically active semiconductor devices. Modern optical communication systems operate around 1550 nm because silica optic fibers have the lowest loss around 1550 nm. InP-based materials can be used to make amplifiers, lasers, and related devices, making it the system of choice for active integrated semiconductor optical devices for the C band.

So III-V semiconductors - InP and its quaternaries, and GaAs and its ternaries, are ideal for the fabrication of micro-ring resonators if other fabrication requirements (smooth, vertical, deep, anisotropic etching, and lithography) are met. Recent demonstrations of devices in this material system at LPS have been driven by the development of technologies for in-house wafer growth by solid-source molecular beam epitaxy [96, 97], smooth, vertical dry-etching of both GaAs and InP [98–102], and high-resolution electron-beam lithography (via a collaboration with the Cornell NanoScale Facility, using the Leica VB6 HR).

Commercial acceptance of III-V semiconductors for passive filters is currently hampered by the high materials cost, high equipment costs, and high optical losses in the material when compared with glass. However, III-V semiconductors are important for the development of ultra-compact monolithically integrated all-optical systems because they are optically active, so this material system is an important target for research and development.

1.7 Objectives

The objectives of this thesis were the development of an etch recipe for smooth, vertical, deep dry-etching of InP-based materials, and the fabrication and characterization of active and passive InP-based micro-ring resonator devices using vertical and/or lateral coupling.

CHAPTER 2

THEORETICAL OVERVIEW

In this chapter, I will describe the theoretical background for this thesis. To begin, I will discuss light-guiding in optical dielectric waveguides. Since a ring resonator is composed of two sets of coupled waveguides (Fig. 1.1), before examining a ring resonator, I will describe the coupling of waveguides. Following this, I will discuss optical ring resonators, characteristics of ring resonators, and parameter extraction from experimental data. Next, I will discuss higher-order filters and their realization with parallel cascaded ring resonators, nonlinear optics with ring resonators, which will be used to demonstrate all-optical logic, and electro-optic tuning, which will be used to demonstrate tunable micro-rings.

2.1 Optical dielectric waveguides

This discussion is adapted from Tien [103], Agrawal [104], and Madsen and Zhao [105].

2.1.1 Total internal reflection and confinement

Dielectric waveguides guide light by confining it in a dielectric 'core,' surrounded by a 'cladding' of lower refractive-index; the cladding may be another dielectric material, or air. A simple way to describe light-guiding in such waveguides is to consider the phenomenon of total internal reflection. Light which enters the core at an angle smaller than the ‘acceptance angle’ of the waveguide experiences total internal reflection at the boundary between the core and the cladding. The result is that the light can be routed to the destination of choice, hence the term ‘optical waveguide.’

In Fig. 2.1, light guiding by total internal reflection is illustrated by considering the light propagating in a slab waveguide as a plane wave. The dotted line represents the direction of the wave-vector. The wave vector can be decomposed into a component parallel to the slab, and another perpendicular to the slab (solid lines). For constructive interference, the wave must experience a phase of $2\pi M$, where M is an integer, in one round-trip between the two core-cladding interfaces; the total phase determines the field distribution in the film. The round-trip phase for a core thickness of a is $2kn_2a\cos\theta + 2\psi$, where k is the free-space wavenumber, and θ is the angle of incidence on the core-cladding interface. The factor of 2ψ comes from the so-called Goos-Hänchen shift. Since the exponentially-decaying tail of the wave extends into the cladding, the effective boundary is inside the cladding, and must be taken into account in calculations of the phase. The perpendicular component is oscillatory; the parallel component propagates and determines the wave velocity.

The round-trip phase requirement means that only certain discrete directions are allowed for the **k**-vector; each direction of the **k**-vector is a waveguide mode.

2.1.2 Mathematical approach

A rigorous mathematical description starts with Maxwell’s equations for light in the core and cladding, and reduces them to the wave equation. We as-

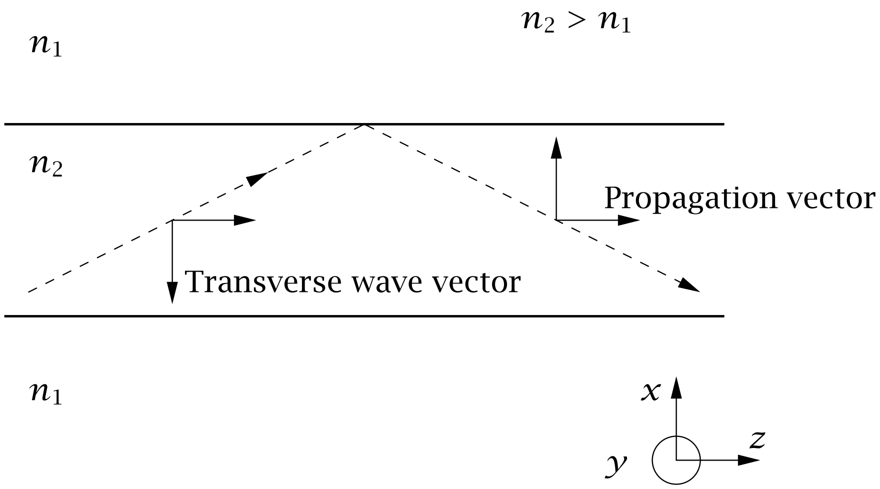

Figure 2.1: Light confinement and guiding by total internal reflection. The zig-zag path can be decomposed into a transverse wavevector describing an oscillatory behavior and a propagation vector.

sume that the direction of propagation is along the z axis and that the field is harmonic in time, t. The z and t dependence is of the form $\exp[j(\beta z - \omega t)]$, where β is the propagation constant in the waveguide (similar to the wavenumber or propagation constant, k_0, in free-space). We use this form with Maxwell's equations and solve in the core and cladding with the appropriate boundary conditions to get β. If $\beta < k_0 n$, the solution is oscillatory, otherwise the solution is an exponential decay. For guided waves, the solution must decay outside the core, and be oscillatory within, which allows us to assume an appropriate form and solve for U.

For a guided wave, $n_{\text{eff}} = \beta/k_0$ is called the 'effective index' of the waveguide, since it represents the ratio of the speed of light in vacuum to that in the waveguide. The exponentially decaying wave outside the waveguide core is called the evanescent wave.

2.1.3 Slab waveguides

For a slab waveguide, where there is confinement only in one direction, say, along the x axis, the boundary conditions would require that the field decay to 0 at $x \to \pm\infty$, and that the wave be a sinusoid of the form $U_0 \exp(\pm j\kappa x)$ in the core, where κ is the transverse wave vector; $\kappa = \sqrt{k_0^2 n^2 - \beta^2}$. Outside the core, $U = U_0 \exp(\pm \gamma x)$, where the attenuation coefficient, γ, is $\sqrt{\beta^2 - k_0^2 n^2}$. Using the boundary conditions on perpendicular and tangential electric and magnetic fields, we can solve for different polarizations.

For the polarization in the plane of the waveguide, E_y, the electric field, is continuous at the core-cladding interface, as is the magnetic field. The continuity of the magnetic field implies the continuity of the derivative of the electric field. Then, for a symmetric slab, we can show that the modes can be classified as even or odd based on the symmetry about the center of the waveguide core. Even modes satisfy the eigenvalue equation

$$\tan\left(\kappa \frac{a}{2}\right) = \frac{\gamma}{\kappa}, \tag{2.1}$$

and odd modes satisfy

$$\tan\left(\kappa \frac{a}{2}\right) = -\frac{\kappa}{\gamma}, \tag{2.2}$$

where a is the thickness of the waveguide. The above equations can be solved numerically to obtain β or n_{eff}.

2.1.4 Rectangular waveguides

In the case of waveguides with rectangular cross-sections, there are no analytical solutions, though there are approximate methods of varying degree of accuracy, notably Marcatili's method [2], and the effective index method [106, 107]. In practice, the problem is best solved numerically. In the past few years, numerous software packages have become available for this purpose; they provide the user with the mode profile as well as the effective refractive index of the waveguide. The software used for the waveguide designs in this work was Optical Waveguide Mode Solver Suite from Apollo Photonics, Inc. The mode profiles for two types of rectangular guides are discussed in the next section.

2.1.5 Weak confinement versus strong confinement

In the previous chapter, I described how bending loss evolves with index contrast (section 1.3). Before delving into the origin of bending loss, let us examine the effect of index contrast and waveguide type (strip-loaded versus pedestal) on the mode profile (intensity distribution across the waveguide); the next section establishes the connection between the index contrast and bending loss.

For optical fibers, which have a (doped) silica core, the index contrast is very small, around a few tenths of a percent. For strip-loaded III-V semiconductor waveguides, the index contrast is quite high along the direction of wafer growth (typically designated as x), around $5 - 10$ %. Along the in-plane direction (usu. y), the index contrast is provided by the presence of three slab-like regions with small effective-index difference, with the central slab having slightly higher effective index than the outer slabs. The confinement in the y direction is, therefore, weak (Fig. 2.2(a)). The waveguide mode is very asymmetric and elliptical in shape. Finally, in the case of pedestal waveguides, the index contrast is high in both the x and y directions, and the mode is well-confined in the waveguide core (Fig. 2.2(b)).

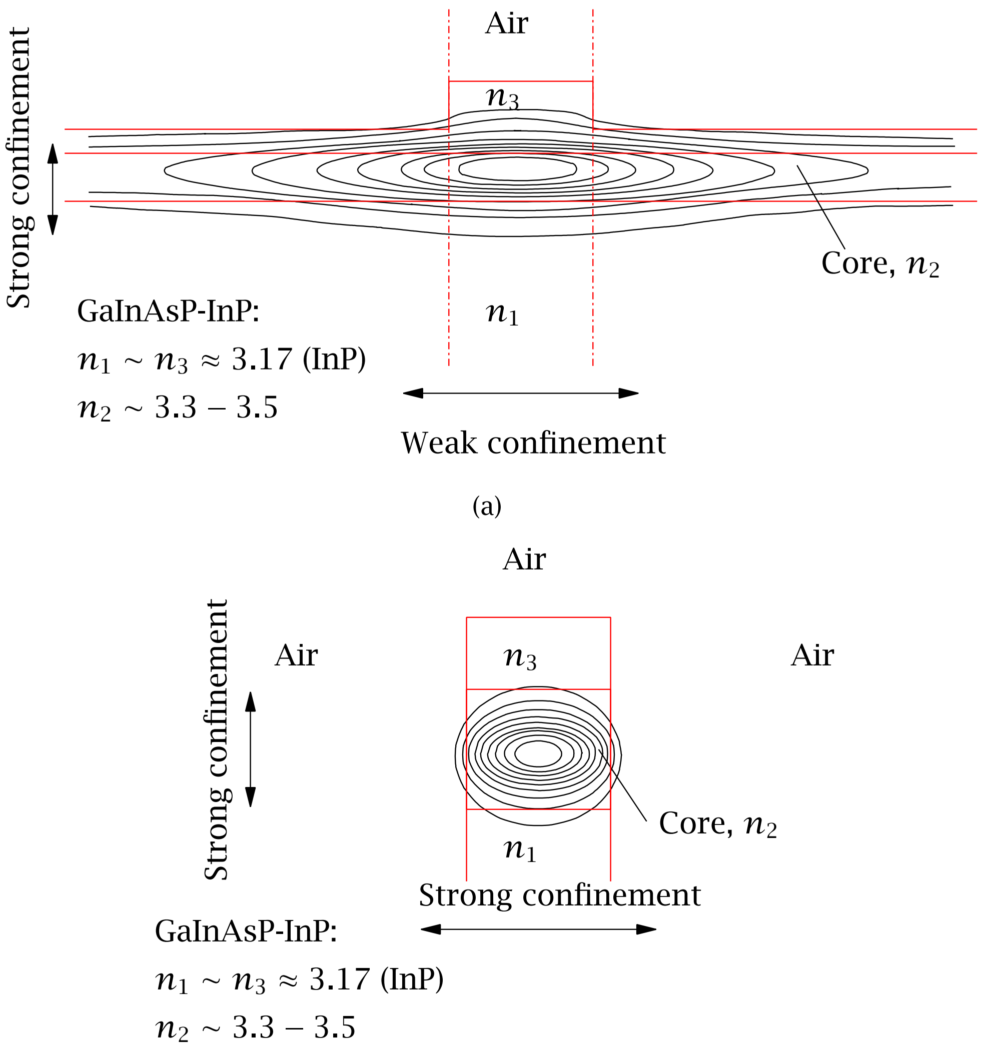

(a)

(b)

Figure 2.2: (a) Schematic of strip loaded waveguide and corresponding mode shape. (b) Pedestal waveguide and corresponding mode shape. In each case, I have shown nine contours, with the innermost representing the locus of points where the intensity falls to 0.9 times the maximum, and the outermost representing the locus of points where the intensity falls to 0.1 times the maximum.

2.1.6 The origin of bending loss

Consider the ray-optics picture shown in Fig. 2.3. The input rays in Fig. 2.3(a) and 2.3(b) enter at the same angle. The ray in Fig. 2.3(a) is incident on the core-cladding interface at the same angle each time, experiences total internal reflection, and is confined. However, the angle of incidence on the core-cladding interface for the ray in Fig. 2.3(b) decreases in the bent section and it is only partially reflected. The critical angle for total internal reflection decreases with index contrast. Then, the stronger the index contrast, the steeper the bend can be while maintaining total internal reflection.

Waveguide modes in optical waveguides can be described by a superposition of plane waves. In a straight waveguide, the plane waves which make up the mode consist of all the directions (for the same wavelength) that can be confined by total internal reflection while meeting the boundary conditions. However, when the mode reaches a bent section, some of the plane waves that make up the mode are no longer guided, and are radiated away. A strong index contrast means that the loss due to such radiation will be minimal.

Analytical solutions to the problem of bending loss can be obtained by using a conformal transformation to convert the problem to an equivalent slab waveguide with a graded index [76]. Marcuse uses a different approach to provide an analytical form; he calculates the loss from the radial component of the field at large distances from the waveguide [78].

Marcuse's analytical form is used to plot Fig. 2.4 for slab waveguides with the largest core-width allowed for single-mode operation. This width can be found by considering the cutoff condition for all modes except the lowest-order mode. Then, we use Marcuse's formula:

$$\alpha = \frac{\kappa^2 \gamma^2 \exp(2\gamma d)}{\beta(1+\gamma d)(\kappa^2+\gamma^2)} \exp\left(-\frac{2\gamma^3}{3\beta^2} R\right), \tag{2.3}$$

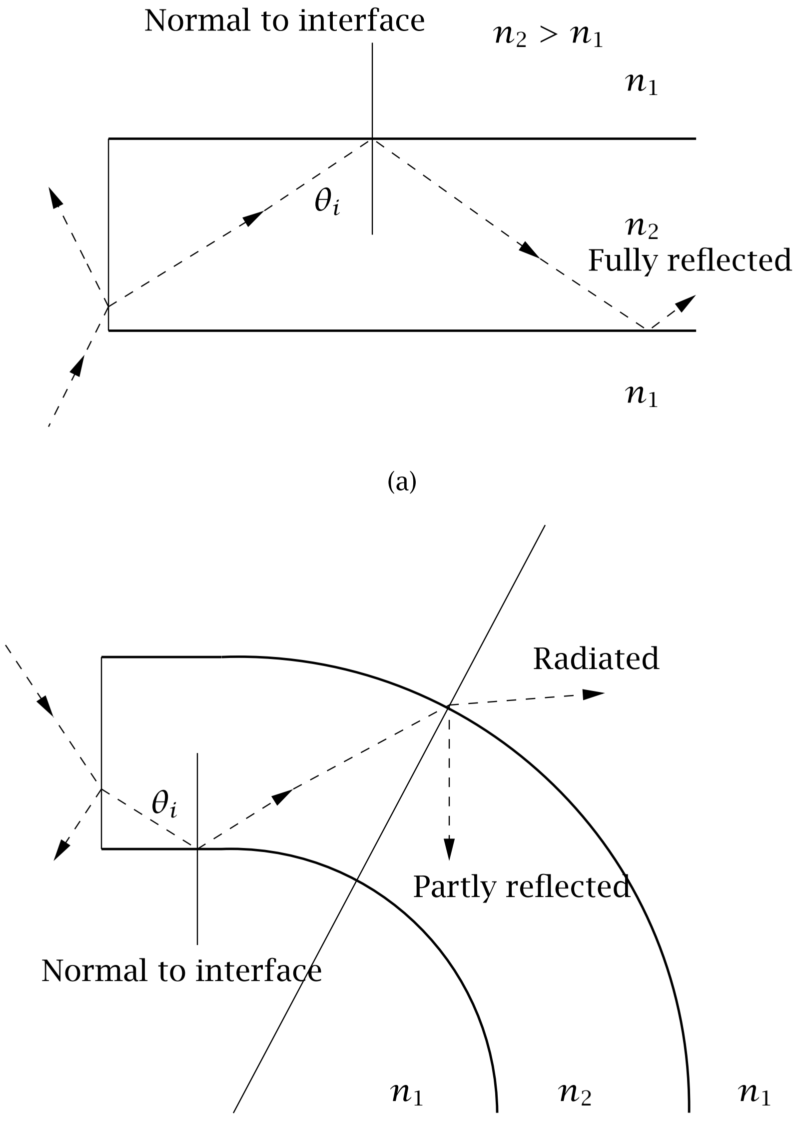

(a)

(b)

Figure 2.3: The origin of bending loss.

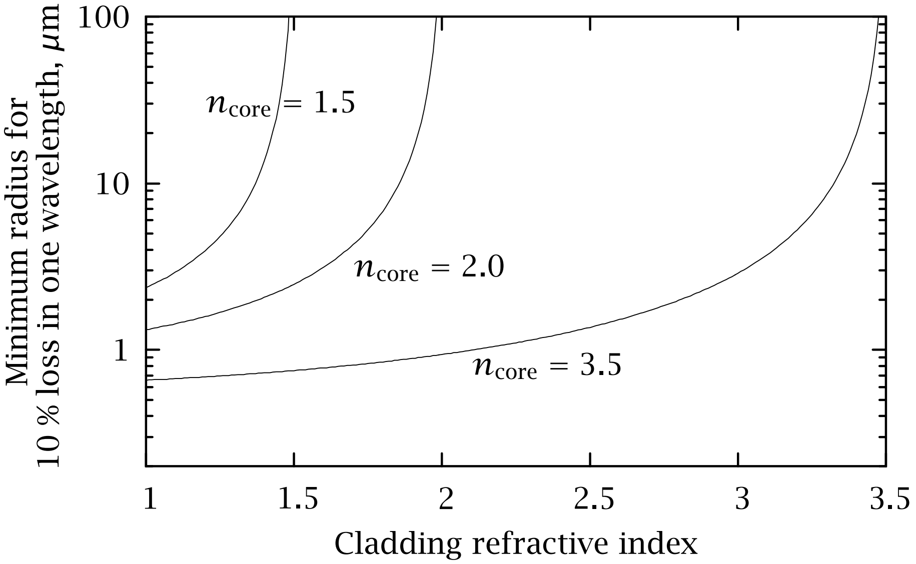

Figure 2.4: Minimum radius for 10 % loss in one wavelength versus cladding index for various core indices.

where κ, γ are as described earlier in this section, β is the propagation constant, d is the width of the waveguide, R is the radius of curvature, and α is the bending loss. A core index of $\sim 1.5 - 2$ is typical of polymers, polyimides, glass, SiO_2, and SiON ~ 2.2 is typical of $LiNbO_3$ and related materials, and $3 - 3.5$ is typical of III-V semiconductors.

Regardless of the approach used, we can predict trends in waveguide behavior from index contrast (the difference in index between core and cladding). Since pedestal waveguides provide the strong index contrast necessary for minimizing bending loss, they are preferred for photonic circuits with very small bending radii. Pedestal waveguides are referred to as ‘tight-confining’ or ‘strong-confining’ because of the corresponding mode shape (see previous section). Although it may seem like a good idea to use ever-higher index contrasts, in practice, high index contrast waveguides pose serious problems.

Fabrication tolerances are more critical because these waveguides must be much smaller than low-index-contrast waveguides to maintain single-mode behavior, and since the modes are much smaller than in fibers, coupling losses become significant, requiring various tricks to be employed to improve coupling efficiency to fibers.

2.2 Coupled waveguides

2.2.1 Coupling of waves in adjacent waveguides

When two waveguides are close to each other, light can be guided in both waveguides, and the problem must be solved all over again. When there is light only in one waveguide, it is eventually transferred to the other waveguide, which couples it back to the first. The coupling of waveguides occurs via the evanescent wave. This is the tail of the wave outside the core of the waveguide which has an imaginary propagation constant along the x-axis outside the first core. In the second core, the propagation constant is no longer imaginary, and the optical version of 'quantum tunneling' occurs. Although the ray-optics picture fails to predict this, it does tell us why coupling cannot occur with a traveling wave: for a traveling wave, there is no angle of incidence that will cause total internal reflection in the second guide. Another point illustrated by the ray optics approach is that the propagation constants of the two waveguides must be the same, otherwise it will not maintain a constant phase with the power transferred.

We can simplify the problem by considering the modes of the two waveguides to be a superposition of the modes of the individual guides. If we use only the lowest-order even-mode, we can get a symmetric or antisymmetric solution. It can be shown that the symmetric and antisymmetric modes have different effective indices. If all the power is in one waveguide, we can represent it as the superposition of the symmetric and antisymmetric modes. Since the two modes have different speeds, over some length (the "beat" length), the power is transferred to the other waveguide and keeps sloshing back and forth while the two waveguides are coupled (Fig. 2.5). The beat length depends on the separation of the two waveguides; if the waveguides are far apart, for all practical purposes, they do not couple.

Coupling coefficients can be calculated from the effective indices of the even and odd modes or by using the modes of the individual waveguides and applying a perturbation-based approach. The perturbation theory method works well for weakly-coupled waveguides, and is treated in detail elsewhere [108]. The phase relationship between the wave in the first waveguide and the part coupled to the second waveguide is not obvious in the preceding arguments. That is described in the following section.

2.2.2 The scattering matrix

Consider a set of coupled waveguides (Fig. 2.6). The output fields are $\mathbf{b} = [b_1, b_2]^{\mathrm{t}}$, and the input fields are $\mathbf{a} = [a_1, a_2]^{\mathrm{t}}$. The scattering matrix $\mathbf{S} = s_{ij}$, which relates the output fields to the input fields, is

$$\mathbf{b} = \mathbf{Sa}. \tag{2.4}$$

Then, using power conservation and time-reversal, we can show that the scattering matrix is symmetric, and has the form [108] (appendix A)

$$\mathbf{S} = \begin{bmatrix} \tau_{\mathrm{C}} & \kappa_{\mathrm{C}} \\ \kappa_{\mathrm{C}} & -\tau_{\mathrm{C}}^{*} \frac{\kappa_{\mathrm{C}}}{\kappa_{\mathrm{C}}^{*}} \end{bmatrix}, \tag{2.5}$$

where

$$\tau_{\mathrm{C}}^{*} \tau_{\mathrm{C}} + \kappa_{\mathrm{C}}^{*} \kappa_{\mathrm{C}} = 1. \tag{2.6}$$

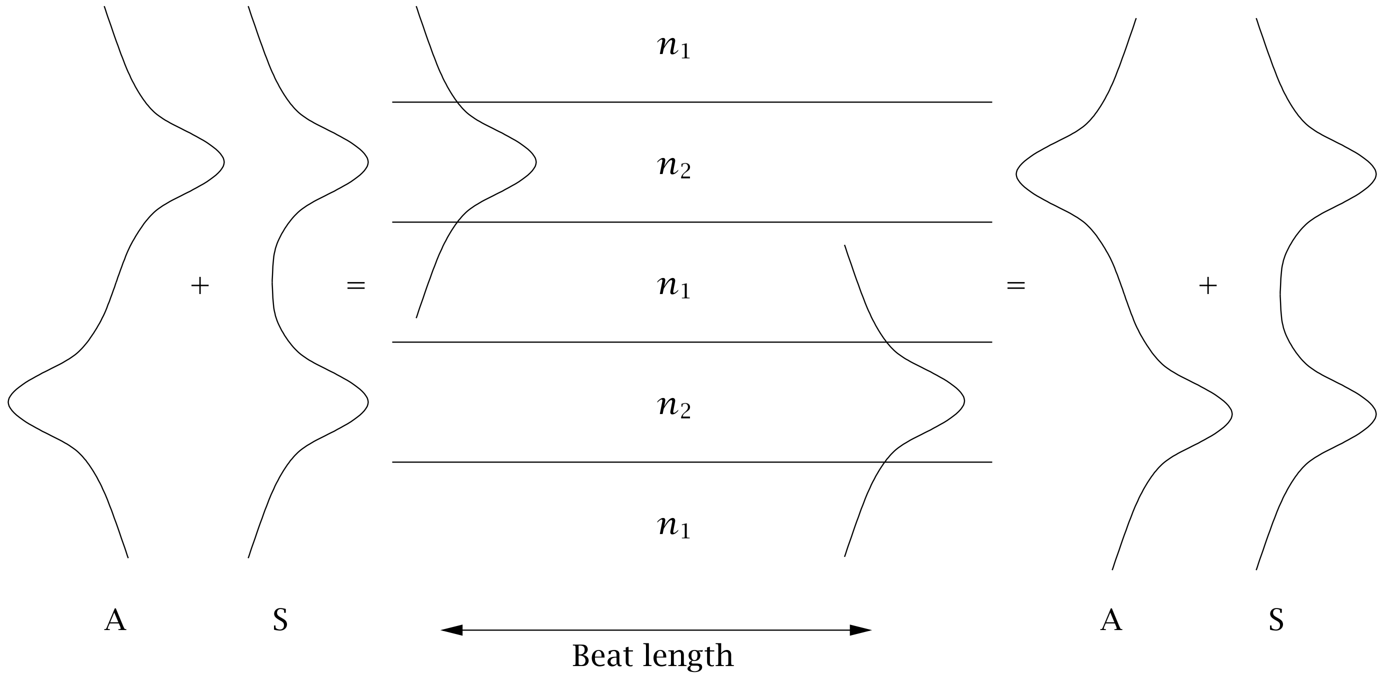

Figure 2.5: Coupling of two slab waveguides. The horizontal lines represent the interfaces between the core and cladding. The direction of propagation is left-to-right (or vice versa).

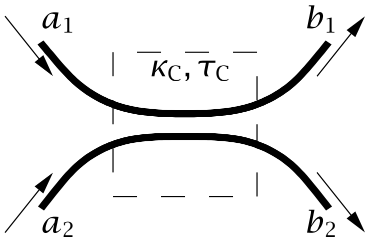

Figure 2.6: Coupling of fields.

If we impose $\tau_C = -\tau_C^* \kappa_C / \kappa_C^* = \tau \in \mathcal{R}$ (where $\mathcal{R}$ is the set of real numbers), we can define $\kappa \in \mathcal{R}$ such that $\kappa_C = \pm j\kappa$. Then $\tau^2 + \kappa^2 = 1$ for lossless coupling, and eq. 2.5 becomes:

$$\mathbf{S} = \begin{bmatrix} \tau & -j\kappa \\ -j\kappa & \tau \end{bmatrix}, \tag{2.7}$$

where I have chosen $-j$ as the phase factor.

2.3 Basic ring resonator operation

In this section, I will describe the operation of a ring resonator optical channel dropping filter (OCDF). A ring resonator OCDF is composed of two sets of coupled waveguides, as shown in Fig. 2.7. The coupling equations outlined in the previous section show that there is a relative phase of $\pi/2$ between the signal coupled to the ring and the signal in the input bus. Similarly, the signal coupled to the drop port, and the signal coupled to the through port, both acquire a phase of π with respect to the signal on the input port. This means that if we engineer the coupling coefficients appropriately, the field coupled to the through port on resonance would completely extinguish the resonant wavelength, and all power would be coupled to the drop port. I will show that

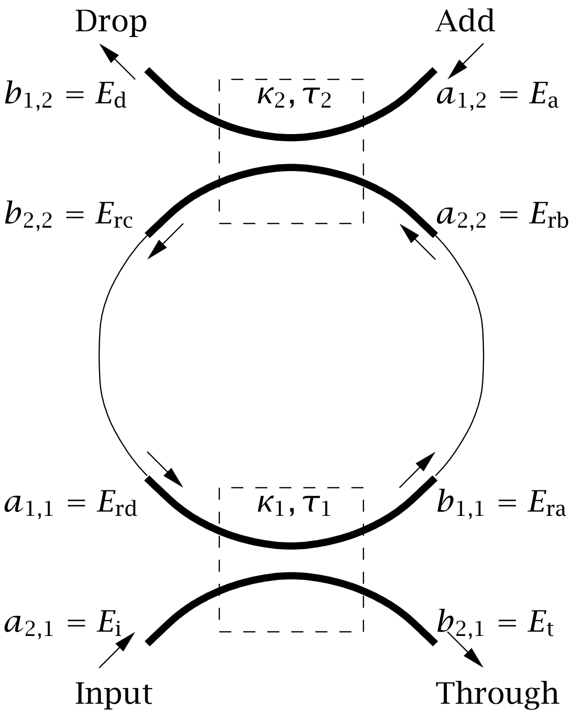

Figure 2.7: Schematic of a ring resonator.

this is possible in later in this section.

Using eq. 2.7 with the assumption that the add-port input, E_a, is zero, we get

$$
\begin{aligned}
E_\mathrm{ra} &= -j\kappa_1 E_\mathrm{i} + \tau_1 E_\mathrm{rd}, && (2.8)\\
E_\mathrm{rb} &= \exp(j\omega T/2)\exp(-\alpha_\mathrm{ring} L/4) E_\mathrm{ra}, && (2.9)\\
E_\mathrm{rc} &= \tau_2 E_\mathrm{rb}, && (2.10)\\
E_\mathrm{rd} &= \exp(j\omega T/2)\exp(-\alpha_\mathrm{ring} L/4) E_\mathrm{rc}, && (2.11)\\
E_\mathrm{t} &= \tau_1 E_\mathrm{i} - j\kappa_1 E_\mathrm{rd}, && (2.12)\\
E_\mathrm{d} &= -j\kappa_2 E_\mathrm{rb}, && (2.13)
\end{aligned}
$$

where E_i is the input field, E_t is the throughput field, E_d is the dropped field,

$E_{\text{ra}} \ldots E_{\text{rd}}$ are the fields in the ring at the points a…d, κ_1 is the field coupling coefficient between the input bus and the ring, κ_2 is the field coupling coefficient between the ring and the output bus, L is the circumference of the ring, T is the time taken for one round trip, and α_{ring} is the power loss in the ring per unit length. We assume lossless coupling, i.e., $\tau_{1,2} = \sqrt{1-\kappa_{1,2}^2}$. T is the round-trip time; $T = Ln_{\text{eff}}/c$.

Solving for E_{d}, E_{t}, we get:

$$\begin{aligned} \frac{E_{\text{d}}}{E_{\text{i}}} &= \frac{-\kappa_1\kappa_2 A_{1/2}\Phi_{1/2}}{1-\tau_1\tau_2 A\Phi}, \text{ and} \qquad (2.14)\\ \frac{E_{\text{t}}}{E_{\text{i}}} &= \frac{\tau_1 - \tau_2 A\Phi}{1-\tau_1\tau_2 A\Phi}, \qquad (2.15) \end{aligned}$$

where $A_{1/2} = \exp(-\alpha_{\text{ring}}L/4)$ (the half-round-trip amplitude), $A = A_{1/2}^2$, $\Phi_{1/2} = \exp(j\omega T/2)$ (the half-round-trip phase contribution), and $\Phi = \Phi_{1/2}^2$.

A signal at the add port, i.e., $E_{\text{a}} \neq 0$, appears as an input for which the drop port above is a through port, etc. Then, by inspection, we have

$$\begin{aligned} E_{\text{d}} &= \frac{-\kappa_1\kappa_2 A_{1/2}\Phi_{1/2}}{1-\tau_1\tau_2 A\Phi}E_{\text{i}} \\ &\quad + \frac{\tau_2 - \tau_1 A\Phi}{1-\tau_1\tau_2 A\Phi}E_{\text{a}}, \text{ and} \qquad (2.16)\\ E_{\text{t}} &= \frac{\tau_1 - \tau_2 A\Phi}{1-\tau_1\tau_2 A\Phi}E_{\text{i}} \\ &\quad + \frac{-\kappa_1\kappa_2 A_{1/2}\Phi_{1/2}}{1-\tau_1\tau_2 A\Phi}E_{\text{a}}. \qquad (2.17) \end{aligned}$$

Per eq. 2.17, we can extract all the power from the input bus on resonance when $\tau_1 = \tau_2 A$. If the resonator is lossless, i.e., $A = A_{1/2} = 1$, we can fabricate a resonator with symmetric coupling ($\kappa_1 = \kappa_2$). Since all the input power is extracted on resonance, we can add a signal at the resonant wavelength on the add-port while simultaneously extracting a signal at the resonant wavelength from the input bus at the drop port, without cross-talk between the dropped and added signals. However, practical resonators are lossy, so simultaneous addition isn't usually possible.

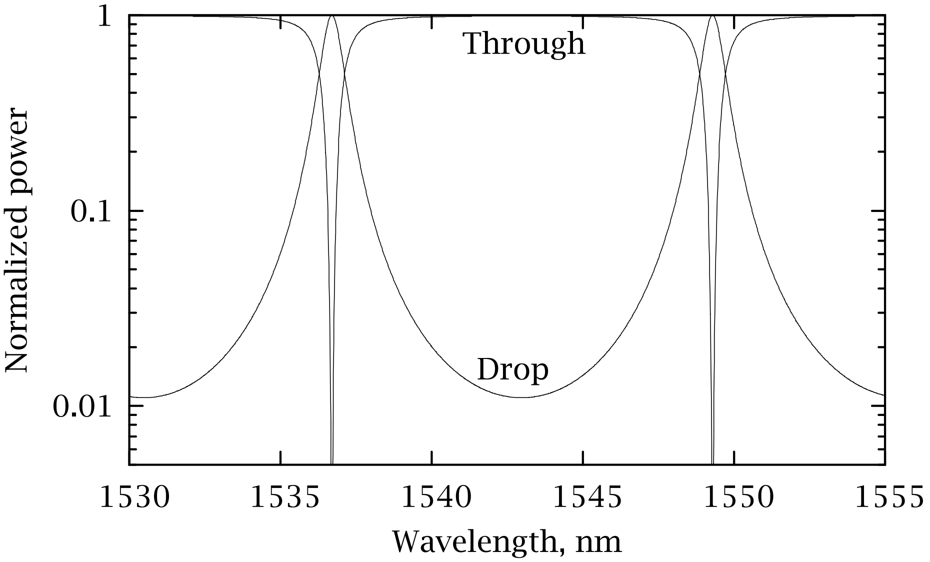

Figure 2.8: Spectral response of an optical channel dropping filter with a lossless ring. $L = 2\pi \times 9.55\ \mu$m, $n_{\text{eff}} = 3.15$, $\tau_1 = A\tau_2 = 0.9$. On resonance, all the power is transferred to the drop port.

The spectral response at the through and drop ports for a single ring OCDF is shown Figs. 2.8 and 2.9. The structure in Fig. 2.8 is symmetric and lossless. On resonance, all the power is dropped from the input port to the drop port. The same holds for a signal on the add port all the power is transferred to the through port from the add port on resonance, allowing the addition of a signal to replace the dropped channel via the add port. Although it is possible to drop all the power from the input port to the drop port in the case of asymmetric coupling, it does not allow the addition of a signal to replace the dropped channel via the add port, since not all the power from the add-port is transferred to the through-port (Fig. 2.9).

Intensity enhancement is another feature of the ring resonator; the intensity in the ring is much larger than that in the input and output bus waveg-

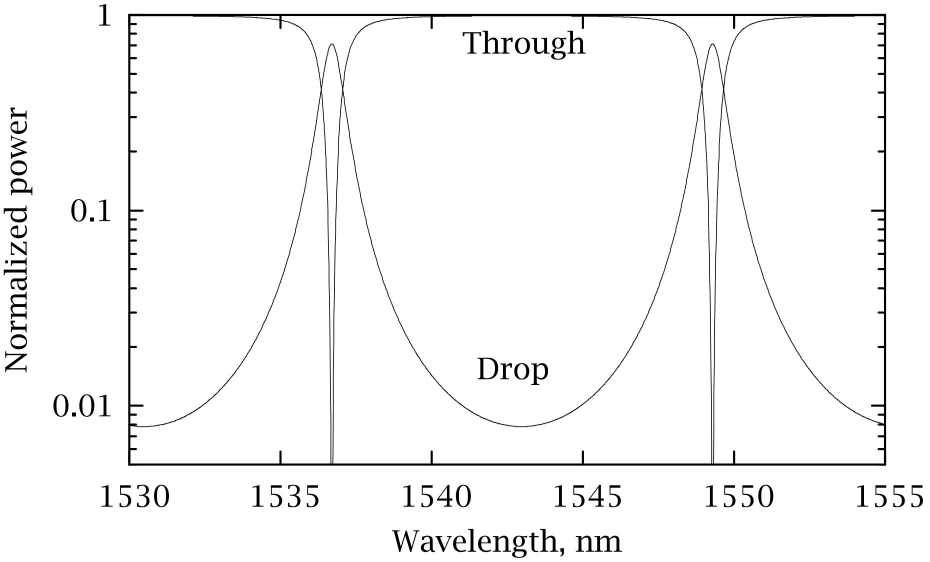

(a) Signal on input port.

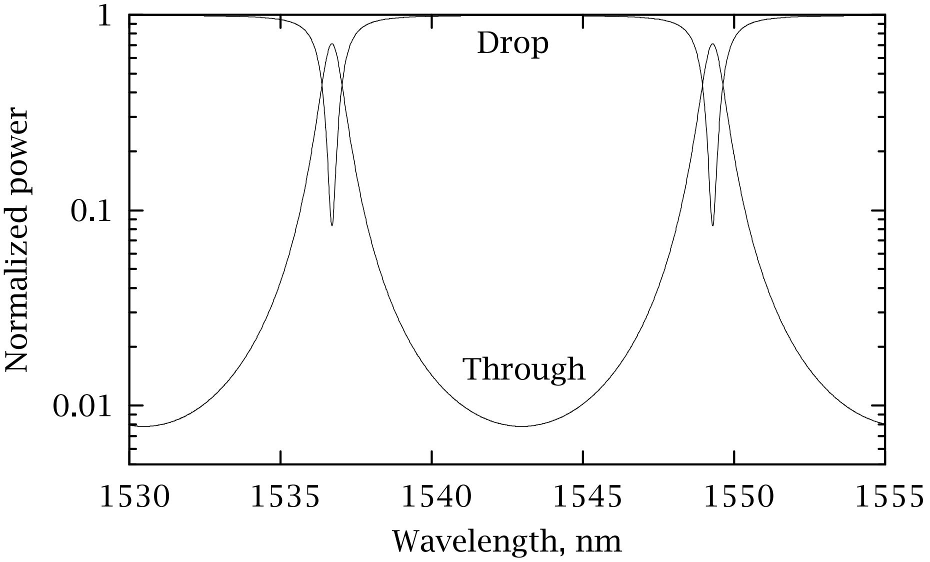

(b) Signal on add port.

Figure 2.9: Spectral response of an optical channel dropping filter with asymmetric coupling, $L = 2\pi \times 9.55\ \mu$m, $n_{\text{eff}} = 3.15$, $\tau_1 = A\tau_2 = 0.9$, $A = 0.97$.

uides. This is discussed in section 2.5.

2.4 The all-pass configuration

In the all-pass configuration, there is only one bus waveguide. Since there is no drop port, $\kappa_2 = 0$ and $\tau_2 = 1$. Then,

$$\frac{E_\mathrm{t}}{E_\mathrm{i}} = \frac{\tau - A\Phi}{1 - \tau A\Phi}. \tag{2.18}$$

In the all-pass configuration, the ring resonator can be used as a phase filter, or as a notch filter. The phase filter represents true all-pass behavior; all the power is passed to the through port, with a phase change on resonance.

2.4.1 Phase filter

For use as a phase filter, the internal loss must be negligibly small, i.e., $A \approx 1$. Then,

$$\frac{E_\mathrm{t}}{E_\mathrm{i}} = \frac{\tau - \Phi}{1 - \tau\Phi}. \tag{2.19}$$

At resonance, $\Phi = 1$, and the RHS is -1, so the signal acquires a π phase shift on resonance. To find the behavior away from resonance, we consider two limiting cases.

Near resonance, we use $\Phi = \exp(j\phi) = \exp[j(2M\pi + \phi')] \equiv 1 + j\phi'$, where $\phi' \to 0$ as we approach the resonance on the ϕ axis, and M is an integer. Then, retaining terms of order ϕ',

$$\begin{aligned} \frac{E_\mathrm{t}}{E_\mathrm{i}} &= \frac{\tau - (1 + j\phi')}{1 - \tau(1 + j\phi')} && (2.20) \\ &= -\frac{(1-\tau)^2 + j\phi'(1-\tau^2)}{(1-\tau)^2}. && (2.21) \end{aligned}$$

Equating the imaginary part with $\sin\theta_\mathrm{out}$,

$$\sin\theta_\mathrm{out} = -\frac{\phi'(1-\tau^2)}{(1-\tau)^2} \tag{2.22}$$

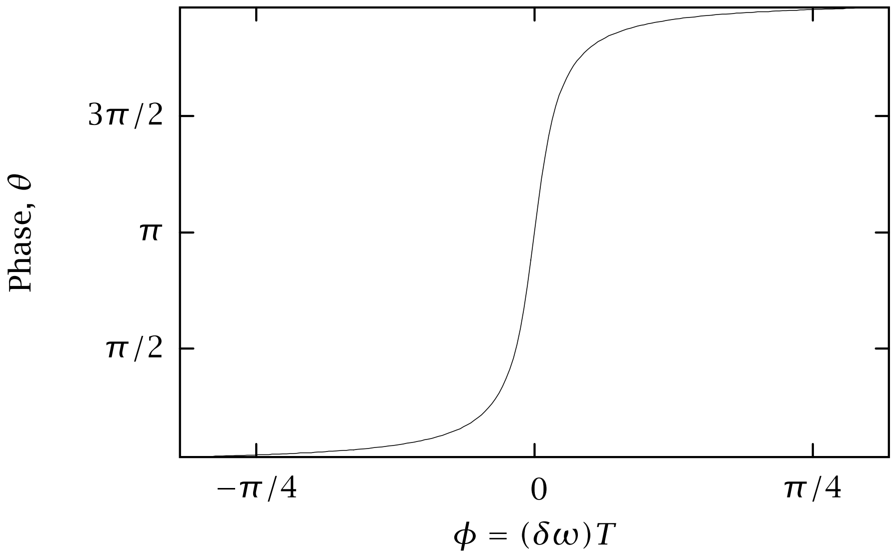

Figure 2.10: Change in phase across a resonance.

$$\Rightarrow \cos\theta_{\text{out}} \frac{\mathrm{d}\theta_{\text{out}}}{\mathrm{d}\phi} = -\frac{1-\tau^2}{(1-\tau)^2} \tag{2.23}$$

$$\Rightarrow \left.\frac{\mathrm{d}\theta_{\text{out}}}{\mathrm{d}\phi}\right|_{\phi=2M\pi} = \frac{1+\tau}{1-\tau} \tag{2.24}$$

$$\Rightarrow \lim_{\phi\to 2M\pi,\kappa\to 0} \frac{\mathrm{d}\theta_{\text{out}}}{\mathrm{d}\phi} = \infty, \tag{2.25}$$

i.e., the phase change has a positive slope and increases extremely fast around a resonance. Fig. 2.10 illustrates the phase change across a resonance.

To find the behavior away from a resonant frequency, we note that $\phi = (2M+1)\pi$ is mid-way between two successive resonances, and write $\phi = (2M+1)\pi + \phi'$, where $\phi' \to 0$ as we approach the point mid-way between two resonances on the ϕ axis. Then, retaining terms of order ϕ',

$$\frac{E_{\text{t}}}{E_{\text{i}}} = \frac{\tau + (1 + j\phi')}{1 + \tau(1 + j\phi')} \tag{2.26}$$

$$= \frac{(1+\tau)^2 + \tau\phi'^2 + j\phi'(1-\tau^2)}{(1+\tau)^2 + (\tau\phi')^2} \tag{2.27}$$

From above, we can get the behavior of the slope of the output phase, θ_{out}, midway between two successive resonances:

$$\sin\theta_{\text{out}} = \frac{\phi'(1-\tau^2)}{(1+\tau)^2} \tag{2.28}$$

$$\Rightarrow \left.\frac{\mathrm{d}\theta_{\text{out}}}{\mathrm{d}\phi}\right|_{\phi=(2M+1)\pi} = \frac{1-\tau^2}{(1+\tau)^2} \tag{2.29}$$

$$\Rightarrow \lim_{\phi\to(2M+1)\pi,\kappa\to 0} \frac{\mathrm{d}\theta_{\text{out}}}{\mathrm{d}\phi} = 0, \tag{2.30}$$

i.e., the output phase is flat between resonances.

2.4.2 Notch filter

For notch filter behavior, consider the ring on resonance, where $\Phi = 1$. If the round-trip amplitude, A, equals the fraction of input field coupled to the through port, τ, the numerator in eq. 2.18 becomes zero, giving us high extinction, or a notch filter. When the coupling condition is fulfilled, the resonator is said to be 'critically-coupled.' On either side of critical coupling, i.e., $A \neq \tau$, the extinction decreases; the device functions as a phase filter for low loss ($A \to 1$), and the resonator doesn't support any resonances when it is very lossy ($A \to 0$). In the case of a lossy resonator, the energy going through the bus is just attenuated to τ^2 of the input value. Fig. 2.11 illustrates the spectral response for critical-coupling, where $A = \tau$, and the response for $A = 0.9\tau$.

At this stage, it is worth pointing out that, mathematically, the ring resonator is no different from a Fabry-Perot filter. Indeed, if we examine a Fabry-Perot filter with mirror reflectivities of κ_1 and κ_2, and cavity length L, we find that the transmitted wave of the Fabry-Perot is the drop-port response of the ring resonator, and the reflected wave of the Fabry-Perot is the through-port response of the ring resonator. The all-pass case corresponds to a Fabry-Perot in which one of the mirrors has 100 % reflectivity.

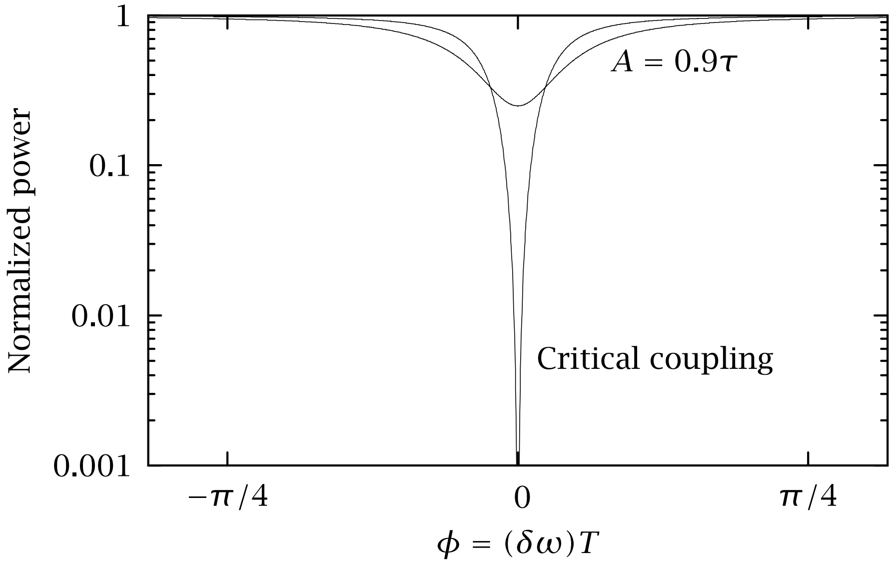

Figure 2.11: Spectral response of an all-pass configuration.

2.5 Characterizing a resonator

Resonators are characterized by their resonance width ($\Delta\omega$ or $\Delta\lambda$), free spectral range (FSR), finesse ($\mathcal{F}$), quality factor (Q), and intensity enhancement ($\mathcal{I}$).

2.5.1 Resonance width, $\Delta\omega$ or $\Delta\lambda$

The resonance width is defined as the full-width at half-maximum of the resonance lineshape. Using the expression for the drop-port output, we can write the drop intensity as

$$\left|\frac{-\kappa_1\kappa_2 A_{1/2}\Phi_{1/2}}{1-\tau_1\tau_2 A\Phi}\right|^2 = \frac{1}{2}\left|\frac{\kappa_1\kappa_2 A_{1/2}}{1-\tau_1\tau_2 A}\right|^2 \tag{2.31}$$

$$\frac{(\kappa_1\kappa_2 A_{1/2})^2}{1-2\tau_1\tau_2 A\cos\phi+(\tau_1\tau_2 A)^2} = \frac{1}{2}\frac{(\kappa_1\kappa_2 A_{1/2})^2}{1-2\tau_1\tau_2 A+(\tau_1\tau_2 A)^2}, \tag{2.32}$$

where $\phi = \Delta\omega T/2$. Then,

$$2(1 - \tau_1\tau_2 A)^2 = 1 - 2\tau_1\tau_2 A\cos\phi + (\tau_1\tau_2 A)^2. \tag{2.33}$$

Per the Euler formula, for small ϕ, $\cos\phi = 1 - \phi^2/2$, so

$$\phi^2 = \frac{(1 - \tau_1\tau_2 A)^2}{\tau_1\tau_2 A}. \tag{2.34}$$

In the case where the loss is negligible, i.e., $A = 1$, and the coupling is symmetric, i.e., $\kappa = \kappa_1 = \kappa_2$, the RHS of eq. 2.34 is $(1 - \tau^2)^2/\tau^2$ ($\tau^2 = 1 - \kappa^2$). Then,

$$\begin{aligned} \phi &= \left[\frac{(1 - \tau^2)^2}{\tau^2}\right]^{1/2} && (2.35)\\ \Rightarrow \Delta\omega &= \frac{2(1 - \tau^2)}{\tau T}, && (2.36) \end{aligned}$$

so, for weak coupling,

$$\Delta\omega = \frac{2\kappa^2 c}{L n_{\text{eff}}}. \tag{2.37}$$

Translating to wavelength,

$$\Delta\lambda \approx \frac{\lambda_0^2}{2\pi c}\Delta\omega, \tag{2.38}$$

where λ_0 is the free-space wavelength, and we have assumed $\lambda_0 \gg \Delta\lambda$. Then,

$$\Delta\lambda \approx \frac{\kappa^2\lambda_0^2}{\pi L n_{\text{eff}}}. \tag{2.39}$$

A more elegant expression for $\Delta\omega$ may be obtained by treating the coupling to the bus waveguides as a distributed loss. We define α_{dis} as $\alpha_{\text{dis}} = \alpha_{\text{ring}} + \alpha_{\text{through}} + \alpha_{\text{drop}}$, $\exp(-\alpha_{\text{through}}L) = \tau_1^2 = 1 - \kappa_1^2$, and $\exp(-\alpha_{\text{drop}}L) = \tau_2^2 = 1 - \kappa_2^2$. Then, eq. 2.34 gives

$$\frac{\Delta\omega T}{2} = \frac{1 - \exp(-\alpha_{\text{dis}}L/2)}{\exp(-\alpha_{\text{dis}}L/4)} \tag{2.40}$$

If $\alpha_{\text{dis}}L \ll 1$, we get

$$\begin{aligned}\Delta\omega &= \frac{2}{T}\frac{\alpha_{\text{dis}}L}{2} \\ &= \frac{\alpha_{\text{dis}}L}{T} = \frac{c\,\alpha_{\text{dis}}}{n_{\text{eff}}}.\end{aligned} \tag{2.41}$$

The above reduces to eq. 2.37 for $\kappa_1 = \kappa_2 = \kappa \ll 1$ since

$$\exp(\alpha_{\text{dis}}L) = 1 - \alpha_{\text{dis}}L \Rightarrow \alpha_{\text{dis}}L = 2\kappa^2. \tag{2.42}$$

2.5.2 Free spectral range, FSR

The FSR is the separation of successive channels. At resonance, $\omega T = 2\pi M$, where T is the round-trip time, and M is an integer. Two successive resonances, ω_1 and ω_2, are then related as

$$\begin{aligned}\text{FSR}_{\text{frequency}} &= \omega_2 - \omega_1 = \frac{2\pi}{T} \\ &= \frac{2\pi c}{L n_{\text{eff}}}.\end{aligned} \tag{2.43}$$

Translating to wavelength, we get

$$\text{FSR}_{\text{wavelength}} = \frac{\lambda_0^2}{L n_{\text{eff}}}. \tag{2.44}$$

2.5.3 Finesse, $\mathcal{F}$

The finesse, $\mathcal{F}$, is defined as the ratio of FSR and resonance width. Using eqs. 2.41 and 2.43,

$$\begin{aligned}\mathcal{F} &= \frac{1}{\frac{c\alpha_{\text{dis}}}{n_{\text{eff}}}}\frac{2\pi c}{L n_{\text{eff}}} \\ &= \frac{2\pi}{\alpha_{\text{dis}}L}\end{aligned} \tag{2.45}$$

In the case where internal loss is negligible and coupling to the bus waveguides is symmetric and weak ($\kappa_1 = \kappa_2 = \kappa \ll 1$), using eq. 2.42, we get

$$\mathcal{F} = \frac{\pi}{\kappa^2}. \tag{2.46}$$

2.5.4 Quality factor, Q

The quality factor of a resonator is a measure of the sharpness of the resonance. The Q is defined as

$$Q = \omega_0 \frac{\text{Stored energy}}{\text{Power loss}}. \tag{2.47}$$

Here, we must use the transient response, since power loss is a temporal phenomenon. Let us consider the behavior of a ring which has been charged to an intensity $|E_0|^2$, at which time the input is switched off. The location at which we measure the intensity is arbitrary. The intensity after the n-th round-trip is:

$$\begin{aligned} |E_n|^2 &= \exp(-\alpha_{\text{dis}}L)|E_{n-1}|^2 && (2.48) \\ &= \exp\left(-n\alpha_{\text{dis}}L\right)|E_0|^2. && (2.49) \end{aligned}$$

If n is large, we can treat it as a continuous variable, and get

$$\frac{\mathrm{d}|E_n|^2}{\mathrm{d}n} = -\alpha_{\text{dis}}L|E_n|^2. \tag{2.50}$$

We can now relate this to the power loss, as each round-trip takes time T. Since the power loss is energy lost per unit time, $\mathrm{d}|E_n|^2/\mathrm{d}t = (1/T)\mathrm{d}|E_n|^2/\mathrm{d}n$. Therefore,

$$\begin{aligned} Q &= \omega_0 \frac{|E_n|^2}{-\mathrm{d}|E_n|^2/\mathrm{d}t} \\ &= \frac{\omega_0 T}{\alpha_{\text{dis}}L}. && (2.51) \end{aligned}$$

From eqs. 2.41 and 2.51,

$$Q = \frac{\omega}{\Delta\omega} \approx \frac{\lambda}{\Delta\lambda}. \tag{2.52}$$

For negligible internal loss and $\kappa_1 = \kappa_2 = \kappa \ll 1$, using eq. 2.42

$$Q = \frac{\omega_0 T}{2\kappa^2}, \tag{2.53}$$

or

$$\begin{aligned} Q &= \frac{\omega_0 L n_{\text{eff}}}{2\kappa^2 c} && (2.54)\\ &\approx \frac{\pi L n_{\text{eff}}}{\lambda_0 \kappa^2}. && (2.55)\end{aligned}$$

A more rigorous approach uses the Laplace transform to go from the steady-state frequency response to the transient response. The field E_{ra} in the ring is given as:

$$\frac{E_{\text{ra}}}{E_{\text{i}}} = \frac{-j\kappa_1}{1 - \tau_1\tau_2 A\Phi}. \tag{2.56}$$

Although the choice of E_{ra} is arbitrary, for a low-loss ring, E_{ra} is a reasonable approximation to the field everywhere in the ring. We can identify $j\delta\omega$ as s, and use the Euler formula to write $\Phi = \exp[j(\delta\omega)T] = \exp(sT) = 1 + sT$. Then,

$$\frac{E_{\text{ra}}}{E_{\text{i}}} = \frac{-j\kappa_1/T}{(1 - A')/T - A's}, \tag{2.57}$$

where $A' = \tau_1\tau_2 A$. If we switch off the input, the transient response is given by $\mathcal{L}^{-1} 1/[(1 - A')/T - A's]$, so that

$$\begin{aligned} E_{\text{ra}}(t) &\sim \mathcal{L}^{-1}\frac{1}{(1 - A')/T - A's} && (2.58)\\ &\sim \exp\left(-\frac{1 - A'}{A'T}t\right). && (2.59)\end{aligned}$$

Identifying the coupling to the bus waveguides as a distributed loss, we get $A' = \exp(-\alpha_{\text{dis}}L/2) = 1 - \alpha_{\text{dis}}L/2$. The Q is then

$$\begin{aligned} Q &= \omega_0 \frac{|E_{\text{ra}}|^2}{\mathrm{d}|E_{\text{ra}}|^2/\mathrm{d}t}\\ &= \omega_0 \frac{A'T}{2\,(1 - A')}\\ &= \frac{\omega_0 T}{\alpha_{\text{dis}} L}, && (2.60)\end{aligned}$$

which is the same as eq. 2.51.

2.5.5 Intensity enhancement, $\mathcal{I}$

When a resonator is on resonance, the field experiences a phase-shift of an integral multiple of 2π in one round-trip. In other words, the signal in the ring interferes constructively with the input signal, and the amplitude builds up. Therefore, the intensity in the ring can be significantly higher than that in the bus waveguides. If we consider E_{ra} as the field in the ring, the field enhancement may be written as

$$\frac{E_{\mathrm{ra}}}{E_{\mathrm{i}}} = \frac{-j\kappa_1}{1 - \tau_1 \tau_2 A \Phi}. \tag{2.61}$$

My choice of E_{ra} is fairly arbitrary; for a low-loss ring, the location at which we consider the field doesn't matter as the difference in amplitude will be minimal. At resonance $\Phi = 1$, and

$$\frac{E_{\mathrm{ra}}}{E_{\mathrm{i}}} = \frac{-j\kappa_1}{1 - A \tau_1 \tau_2}. \tag{2.62}$$

Then, for $\kappa_1 = \kappa_2 = \kappa \ll 1$ and negligible internal loss,

$$\frac{E_{\mathrm{ra}}}{E_{\mathrm{i}}} = \frac{-j}{\kappa}, \tag{2.63}$$

and the intensity enhancement may be written as,

$$\mathcal{I} = \left| \frac{E_{\mathrm{ra}}}{E_{\mathrm{i}}} \right|^2 = \frac{1}{\kappa^2} = \frac{\mathcal{F}}{\pi}. \tag{2.64}$$

For values of κ^2 circa 0.1, the intensity in the ring is then 10 times that in the input waveguide. Since the intensity in the ring can be much higher then in the bus, ring resonators can be used for nonlinear optics experiments with moderate input intensities. In the all-pass configuration, on resonance,

$$\mathcal{I} = \frac{1 + \tau}{1 - \tau}. \tag{2.65}$$

Since $0 < \tau < 1$, the intensity enhancement is between 1 and $4/\kappa^2$ for the all-pass configuration. Usually $\kappa \ll 1$, so $\mathcal{I} \approx 4/\kappa^2$ for an all-pass configuration.

2.6 Physical significance of $\mathcal{F}$ and Q

To find the physical meaning of the finesse and Q, we consider the number of round-trips made by the energy in the ring before being lost to internal loss and the bus waveguides. If we define N as the number of round-trips required to reduce the energy to $1/e$ of its initial value, we get

$$\begin{aligned} \exp\left(-\alpha_{\text{dis}} N L\right) &= \frac{1}{e} & (2.66)\\ \Rightarrow N &= \frac{1}{\alpha_{\text{dis}} L} & (2.67)\\ \Rightarrow \mathcal{F} &= 2\pi N. & (2.68) \end{aligned}$$

Eq. 2.68 tells us that the finesse represents, to a factor of 2π, the number of round-trips made by light in the ring before the power is depleted to $1/e$ of its initial value. Similarly,

$$Q = \omega_0 T N, \tag{2.69}$$

which tells us that Q represents the number of oscillations of the field before being depleted to $1/e$ of the initial energy.

We can define the photon lifetime as $\tau_{\text{photon}} \equiv NT$ from above, which tells us that the $\mathcal{F}$ and Q are directly proportional to, hence represent metrics for, the photon lifetime in the cavity.

Comparing eq. 2.64 with eqs. 2.46 and 2.53, we see that

$$\mathcal{I} = \frac{\mathcal{F}}{\pi} = \frac{1}{\omega_0 T} Q. \tag{2.70}$$

Therefore, the finesse and Q also represent metrics for the intensity enhancement in a ring resonator.

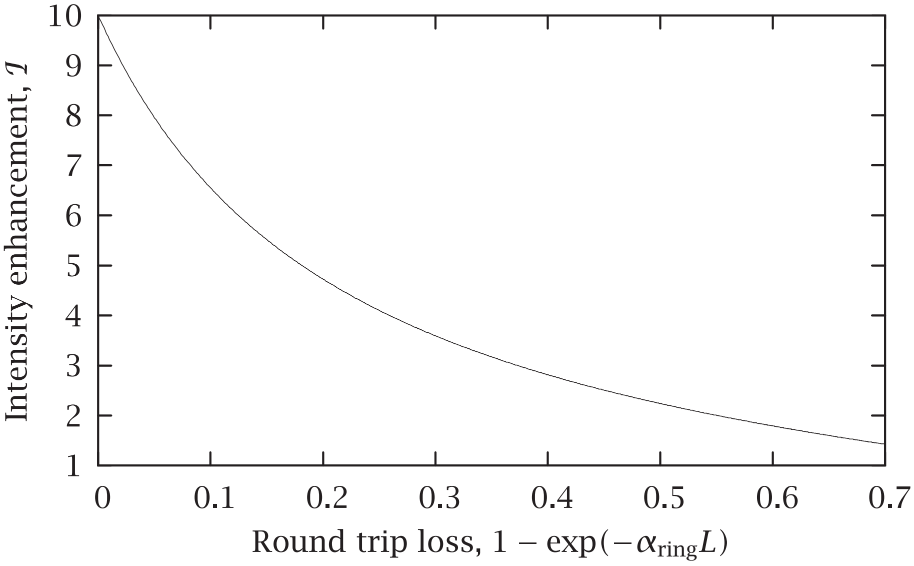

Figure 2.12: Effect of loss on intensity enhancement for 10 % input coupling.

2.7 Effect of loss

Loss can seriously degrade the characteristics of a ring resonator, since the resonance width increases, and the Q and $\mathcal{F}$ decrease. In section 2.3, I described how excessive ring loss can prevent the addition of a signal on a resonant wavelength while simultaneously dropping a channel. For fixed input/output coupling, loss decreases the intensity enhancement, $\mathcal{I}$ (Fig. 2.12). Since nonlinear phenomena depend on $\mathcal{I}$, more power is needed to observe nonlinear phenomena in the ring (section 2.11).

2.8 Filter characteristics needed for communication systems

Modern communication systems use multiple wavelengths on the same fiber; this is referred to as wavelength-division multiplexing (WDM). Each wavelength is referred to as a channel, and the typical channel spacing in state-of-the-art systems is 100 GHz or less. Most current optical WDM systems operate in the regime where erbium-doped fiber amplifiers provide gain (called the EDFA band), which roughly spans 1530 – 1570 nm. So the ideal band-pass filter for today's communication systems would have one resonant wavelength in the EDFA band, with resonance bandwidth less than the channel spacing (< 100 GHz).

A channel spacing of 100 GHz dictates that $\Delta\omega = 2\pi \times 100$ GHz, or $\Delta\lambda \approx 0.8$ nm at 1550 nm. For a ring filter, this dictates a maximum loss (including coupling to bus waveguides) of around 30 %. If we relax the requirement on the FSR and consider a circular ring filter with radius 10 μm ($L = 62$ μm), $n_{\text{eff}} = 3.1$, $\mathcal{F} \approx 16$. These requirements are not unrealistic, and many of the filters from our group meet or exceed them.

For nonlinear optics experiments, the factor of interest is the intensity enhancement, and a finesse of 16 would provide $\mathcal{I} \approx 5$. Most nonlinear optical phenomena are enhanced in resonators to a power of $\mathcal{I}$, so even moderate values of $\mathcal{I}$ can provide a significant boost to such phenomena.

2.9 Extraction of filter characteristics

Having defined the filter characteristics of interest, we can now discuss the extraction of parameters from experimental data. Given a spectrum, we can use an automated routine in (say) Matlab, to find the resonance widths at each resonant frequency or wavelength. The resonant frequency of wavelengths are simply the local maxima in the spectrum and can be found by normalizing to the maximum power and searching for maxima above a threshold. (It is important to define a threshold otherwise noisy data will result in incorrect identification of resonant wavelengths.)

Since $Q = \omega/\Delta\omega \approx \lambda/\Delta\lambda$, we can then calculate Q. By finding the local maxima and noting their separation, we get the FSR of the device. Since we know the resonance widths, we can calculate the finesse as $\text{FSR}_\lambda/\Delta\lambda$, where FSR_λ refers to FSR measured on the wavelength scale.

Using simulations, we estimate the effective index of the ring waveguide, and refine the estimate with the resonance frequencies. We then use the Q to estimate the coupling coefficient, κ, and using the estimate as an initial guess, fit eq. 2.14 to the spectrum to get α_{ring} and κ. Although two pairs of α_{ring} and κ are obtained, usually, the loss measurement from straight waveguides can be used to select the appropriate pair. Since we know the n_{eff} at each resonance frequency, we can find the dispersion of the waveguide.

Extraction of material characteristics for electro-optically tuned devices is discussed in section 2.12.

2.10 Higher-order filters

The filter-order describes how the filter response behaves away from the resonant wavelength or frequency. The drop-port amplitude for a single-ring OCDF evolves as $1/\{1 - \tau_1\tau_2 A[1 + j(\omega - \omega_0)T]\}$ (eq. 2.14), so the drop-port intensity evolves as $1/[(\tau_1\tau_2 AT)^2(\omega - \omega_0)^2 + (1 - \tau_1\tau_2 A)^2]$ (near ω_0), which is a Lorentzian. By higher-order response, we refer to the roll-off compared to a single resonator device. A single-ring device has a roll-off of 20 dB/decade, and is referred to as a first-order filter, because the drop-port amplitude evolves as $1/j\omega$. In some applications, such as band-pass filters, we require improved rejection out-of-band (away from resonance). We can draw an analogy between the ring as a reactive optical element and an electronic filter with LC elements; cascading reactive elements makes the filter response steeper

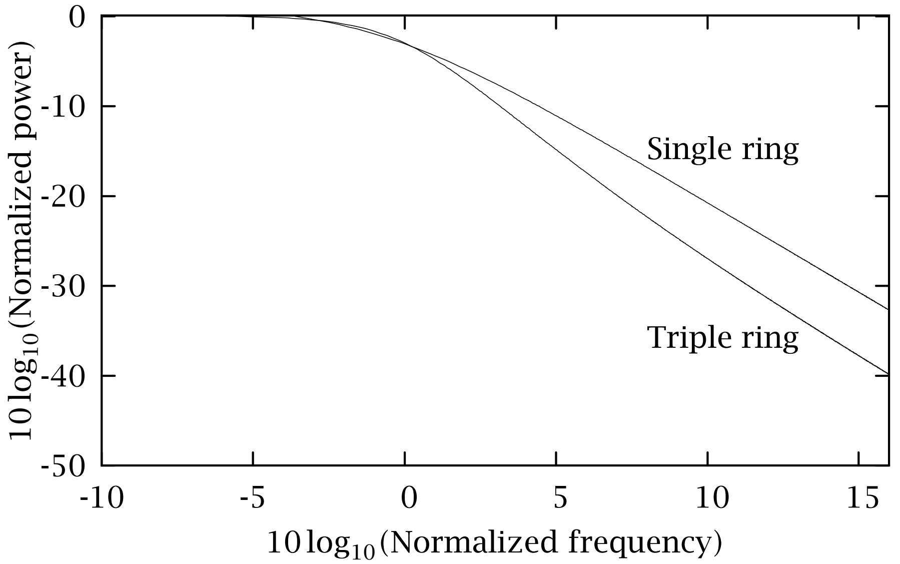

Figure 2.13: Roll-off for a first and third-order optical ring resonator filter.

away from resonance. Rings can be cascaded serially (Fig. 2.14) or in parallel (Fig. 2.15), allowing the fabrication of higher order filters with increased FSR and faster roll-off compared to a single ring resonator device. In both cases, the Vernier effect can boost certain resonances and suppress others, resulting in a wide free spectral range. In a serial cascade, the resonators are coupled directly to each other. In a parallel cascade the resonators

are coupled via the bus, and the filter response depends on the length of the bus waveguide between the rings. For example, Fig. 2.13 compares the roll-off of a parallel-cascade of three rings and a single-ring filter. The x-axis is normalized to the bandwidths of the two filters.

Mathematically, the response of some filters may be written as [105, 109]

$$H(s) = \frac{P_1(s)}{P_2(s)}, \tag{2.71}$$

where P_1 and P_2 are polynomials, and the filter response is evaluated near a

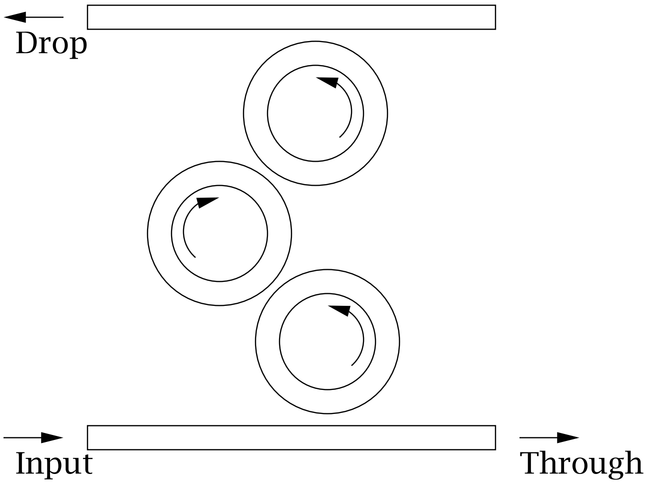

Figure 2.14: Serially cascaded rings.

resonance; $sT \ll 1$,

$s = j(\omega - \omega_0)$, where ω_0 is a resonant frequency. For a single-ring OCDF, the drop-port response in the above form can be obtained from eq. 2.14 as

$$\frac{E_\mathrm{d}}{E_\mathrm{i}} = \frac{-\kappa_1\kappa_2 A_{1/2}(1+s)}{(1-\tau_1\tau_2 A) - s\tau_1\tau_2 A}. \tag{2.72}$$

The zeros of P_1 are called the zeros of the filter, and the zeros of P_2 are called the poles of the filter. If we assume that P_1 and P_2 have no zeros in common, the filter-order is determined from the order of P_2; in a first-order filter, the polynomial P_2 is of the form $(s-p)$, i.e., a first-order polynomial; the single-ring OCDF response shown above, therefore, qualifies as a first-order response. For an n-th order filter, the polynomial P_2 is of the form $\prod_n (s - p_n)^n$, where the poles, p_n, may be degenerate. The asymptotic behavior of the filter is s^{-n}, so it has a sharper roll-off than a first-order filter. At the same time, by using interference effects between multiple filters, a flatter top compared to lower-order filters can be obtained. Sharper roll-off is desirable in applications such as band-pass filters for better isolation between channels.

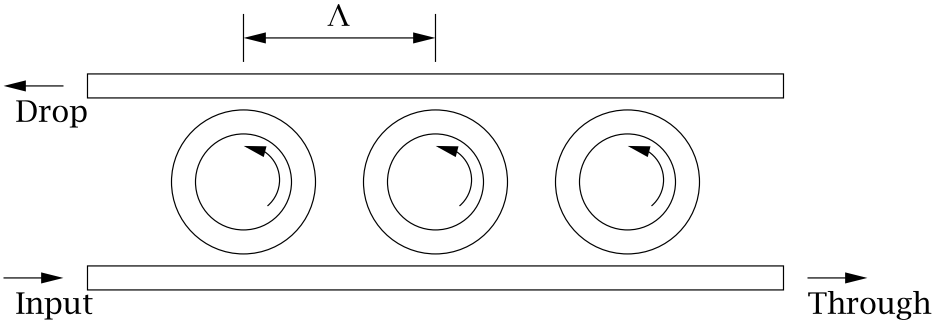

Figure 2.15: Rings cascaded in parallel.

A flat-top minimizes signal distortion in similar applications.

I will go over parallel-cascaded ring resonators here because we will encounter them in chapter 4. Serially coupled resonators have been analyzed elsewhere [15,105,110,111] and demonstrated by several groups [15,18,46]. Parallel cascaded ring resonators have been discussed by Little et al. [112], Griffel [113], Melloni [114], and Grover et al. [63], and demonstrated by a few groups [22,63]. My analysis follows [63].

The equations in section 2.3 allow us to treat the single micro-ring device with the transfer matrix approach as

$$\begin{bmatrix} E_\mathrm{i} \\ E_\mathrm{d} \end{bmatrix} = \begin{bmatrix} T_{11} & T_{12} \\ T_{21} & T_{22} \end{bmatrix} \begin{bmatrix} E_\mathrm{t} \\ E_\mathrm{a} \end{bmatrix}, \text{ where} \tag{2.73}$$

$$T_{11} = \frac{1-\tau_1\tau_2 A\Phi}{\tau_1-\tau_2 A\Phi}, \tag{2.74}$$

$$T_{12} = \frac{\kappa_1\kappa_2 A_{1/2}\Phi_{1/2}}{\tau_1-\tau_2 A\Phi}, \tag{2.75}$$

$$T_{21} = -T_{12}, \text{ and} \tag{2.76}$$

$$T_{22} = \frac{\tau_1\tau_2 - A\Phi}{\tau_1-\tau_2 A\Phi}. \tag{2.77}$$

Now, consider a parallel cascade of microresonators separated by Λ (Fig. 2.15).

The transfer matrix of each bus section of length Λ, $\mathbf{T}_{\phi}$, is

$$\mathbf{T}_{\text{bus}} = \begin{bmatrix} \Phi_{\text{bus}}^{*} \exp\left(-\alpha_{\text{bus}} \frac{\Lambda}{2}\right) & 0 \\ 0 & \Phi_{\text{bus}} \exp\left(-\alpha_{\text{bus}} \frac{\Lambda}{2}\right) \end{bmatrix}, \tag{2.78}$$

where $\Phi_{\text{bus}} = \exp(-j\beta_{\text{bus}}\Lambda)$, β_{bus} is the propagation constant in the bus waveguide, and α_{bus} is the loss per unit length in the bus. Using the transfer matrix defined in eq. 2.73,

$$\begin{bmatrix} E_{\text{i}1} \\ E_{\text{d}1} \end{bmatrix} = \mathbf{T}_1 \cdot \mathbf{T}_{\text{bus}} \cdot \mathbf{T}_2 \cdot \mathbf{T}_{\text{bus}} \ldots \mathbf{T}_N \begin{bmatrix} E_{\text{t}N} \\ E_{\text{a}N} \end{bmatrix}, \tag{2.79}$$

where $E_{\text{i}m}$ is the input-port field for the m-th resonator, $E_{\text{d}m}$ is the drop-port field, $E_{\text{t}m}$ is the through-port field, and $E_{\text{a}m}$ is the add-port field.

To show that the response of a multi-ring cascade has higher-order behavior, we only need to show that a double-ring cascade has second-order behavior; the behavior of cascades with more rings will follow by induction. The response for a double ring cascade is:

$$\begin{bmatrix} E_{\text{i}1} \\ E_{\text{d}1} \end{bmatrix} = \mathbf{T}_1 \cdot \mathbf{T}_{\text{bus}} \cdot \mathbf{T}_2 \begin{bmatrix} E_{\text{t}2} \\ E_{\text{a}2} \end{bmatrix}. \tag{2.80}$$

If we assume that the two rings are similar and assume that the bus waveguide has no loss, the net transfer function, $\mathbf{T}^{\text{2RP}}$, is given as:

$$\begin{aligned} \mathbf{T}^{\text{2RP}} &= \begin{bmatrix} T_{11} & T_{12} \\ T_{21} & T_{22} \end{bmatrix} \begin{bmatrix} \Phi_{\text{bus}}^{*} & 0 \\ 0 & \Phi_{\text{bus}} \end{bmatrix} \begin{bmatrix} T_{11} & T_{12} \\ T_{21} & T_{22} \end{bmatrix} \\ &= \begin{bmatrix} T_{11} & T_{12} \\ T_{21} & T_{22} \end{bmatrix} \begin{bmatrix} T_{11}\Phi_{\text{bus}}^{*} & T_{12}\Phi_{\text{bus}} \\ T_{21}\Phi_{\text{bus}}^{*} & T_{22}\Phi_{\text{bus}} \end{bmatrix} \\ &= \begin{bmatrix} (T_{11}^2 + T_{21}^2)\Phi_{\text{bus}}^{*} & (T_{11} + T_{22})T_{12}\Phi_{\text{bus}} \\ (T_{11} + T_{22})T_{21}\Phi_{\text{bus}}^{*} & (T_{22}^2 + T_{21}^2)\Phi_{\text{bus}} \end{bmatrix} \end{aligned} \tag{2.81}$$

Then

$$\begin{aligned}\frac{E_{\mathrm{d2}}}{E_{\mathrm{i2}}} &= \frac{T_{12}^{\mathrm{2RP}}}{T_{11}^{\mathrm{2RP}}}\\ &= \frac{(T_{11}+T_{22})T_{12}\Phi_{\mathrm{bus}}}{(T_{11}^2+T_{21}^2)\Phi_{\mathrm{bus}}^*}.\end{aligned} \tag{2.82}$$

We can now substitute the expressions for the various terms on the RHS from eq. 2.73 and see that the numerator and denominator on the RHS have no common factors. So the roll-off near a resonance is determined by the denominator. Since both T_{11} and T_{21} are polynomials of first-order in $\Phi = \exp(j\omega T) \approx 1 + j(\omega - \omega_0)T$, or $s = j(\omega - \omega_0)$, the denominator is a polynomial of second-order in s. Thus the double-ring parallel cascade behaves as a second-order filter. Similarly, a single ring cascaded in parallel with an n-ring cascade (with n-th order response) has a response of order $(n+1)$, etc. In other words, a parallel cascaded N-ring OCDF has a roll-off N-times faster than a single ring OCDF. The faster roll-off possible with a multi-ring cascade is shown in Figs. 2.13 and 2.16 for the case where there are three rings.

If the spacing, Λ, between the resonators is chosen such that

$$N_{\mathrm{r}} \cdot \mathrm{FSR}_{\mathrm{r}} = N_{\mathrm{b}} \cdot \mathrm{FSR}_{\mathrm{b}} = \mathrm{FSR}_{\mathrm{a}}, \tag{2.83}$$

where $\mathrm{FSR}_{\mathrm{r}}$ is the FSR of the resonator, $\mathrm{FSR}_{\mathrm{b}}$ is the FSR of the bus section between the resonators, and N_{r} and N_{b} are integers, then the Vernier effect causes the suppression of transmission peaks within the spectral range $\mathrm{FSR}_{\mathrm{a}}$, resulting in an N_{r}-fold increase of the effective FSR. Since $\mathrm{FSR}_{\mathrm{r}} = 2\pi c/n_{\mathrm{r}}L$, and $\mathrm{FSR}_{\mathrm{b}} = \pi c/n_{\mathrm{b}}\Lambda$, eq. 2.83 gives

$$\Lambda = \frac{N_{\mathrm{b}}}{N_{\mathrm{r}}}\frac{n_{\mathrm{r}}}{n_{\mathrm{b}}}\frac{L}{2} \tag{2.84}$$

for an effective N_{r}-fold increase in the FSR of the filter. The Vernier effect is illustrated in Fig. 2.17, and the simulated drop port response of a triple-ring parallel cascade OCDF is shown in Fig. 2.18.

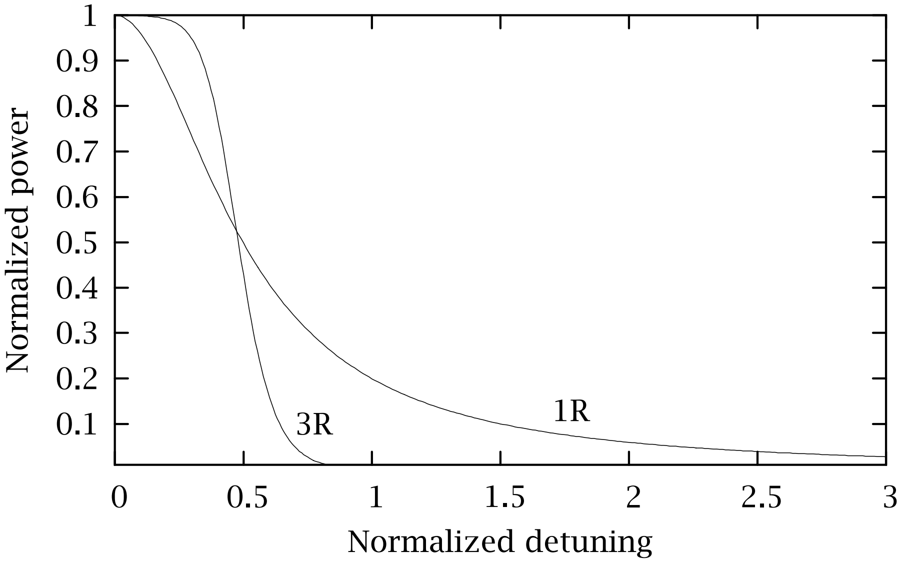

Figure 2.16: A triple ring parallel cascade (3R) has faster roll-off than a single ring (1R).

The simulation parameters are $\alpha_{\text{ring}} = 5 \times 10^{-8}$ nm^{-1}, $L = 60004$ nm, $\kappa_1 = \kappa_2 = \sqrt{0.1}$, $n_{\text{eff}}^{\text{ring}} = 3.1$, $\alpha_{\text{bus}} = 0$, $\Lambda = 39000$ nm, $n_{\text{eff}}^{\text{bus}} = 3.15$. The x-axis has been normalized to the bandwidths of the two filters.

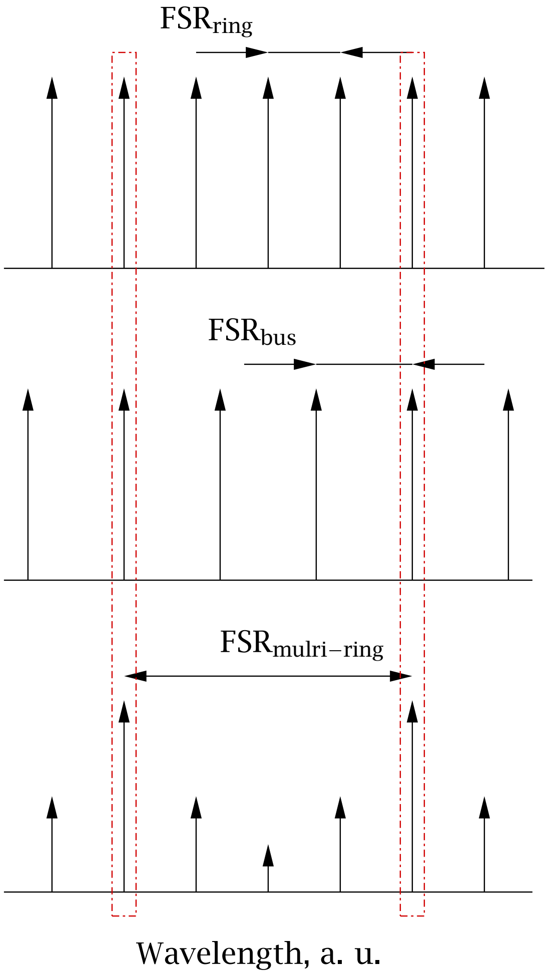

Figure 2.17: Vernier effect with a multi-ring cascade. The resonances of the rings which coincide with those of the bus are boosted and the others are suppressed.

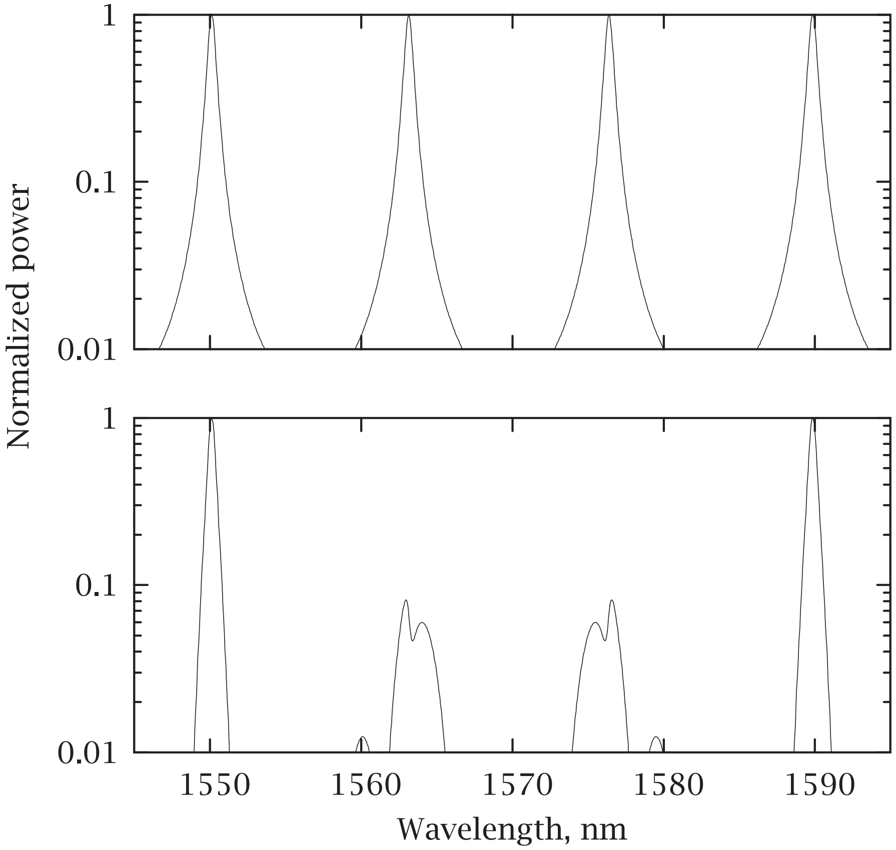

Figure 2.18: Simulated drop port response of triple ring parallel cascade OCDF (bottom) and single ring OCDF (top). The simulation parameters are $\alpha_{\mathrm{ring}} = 5 \times 10^{-6}$ nm^{-1}, $L = 60004$ nm, $\kappa_1 = \kappa_2 = 0.1$, $n_{\mathrm{eff}}^{\mathrm{ring}} = 3.1$, $\alpha_{\mathrm{bus}} = 10^{-6}$ nm^{-1}, $\Lambda = 39368$ nm, $n_{\mathrm{eff}}^{\mathrm{bus}} = 3.15$. With appropriate choice of bus length, it is possible to suppress some resonances, giving a wide FSR.

There are significant practical limitations to the number of resonators that can be cascaded in parallel or series. Both resonator and bus loss limit the number of resonators, as does the fabrication accuracy, which affects the ability to exactly tailor resonator and bus response for using the Vernier effect. In a parallel cascade, if the loss in the bus is high, the amount of light reaching the rings down the cascade will not be enough to enable them to affect the filter response; in that case, the response will be of a lower order than designed. In a serial cascade, if the loss in the ring is high, no power will reach the output bus.

A triple-ring parallel cascaded micro-ring OCDF is demonstrated in section 4.3.2.

2.11 Nonlinear optics with micro-ring resonators

When a signal resonates in a micro-ring, the signal intensity in the ring can be substantially higher than that in the input waveguide (section 2.5). The increase in signal intensity can boost non-linear phenomena, such as carrier generation by two-photon absorption, and change in refractive index due to the intensity dependence of refractive index and/or due to carrier generation.

Let us define an optical logic where high transmission corresponds to a logical 1, and a low transmission corresponds to a logical 0. Then, using the refractive index change from two-photon absorption, in a simple all-pass configuration (notch filter), we can go from $0 \rightarrow 1$ if initially on-resonance, or $1 \rightarrow 0$ if initially off-resonance. By combining two input signals, co-propagating at two different wavelengths, or counter-propagating at the same wavelength (to allow separation), we can switch on or switch off a control signal when the input signal pulses coincide spatially and temporally, giving us a (N)AND operation, and hence, optical logic.

If the refractive index change is caused by carrier generation (via single or two photon absorption), the speed of switching depends on the lifetime of carriers in the ring. Since the width of the ring waveguide is usually $<$ 1 μm, carriers can diffuse to the surface and surface recombination becomes important. The carrier lifetime can be approximated by the time taken to reach the surface. Holes have much lower mobility than electrons, and in intrinsic materials, the carrier lifetime (hence, switching) is dominated by the hole lifetime. This phenomenon is known as 'ambipolar diffusion' [115, 116]. There are a number of methods that can be used to shorten carrier lifetime: a bias to sweep the carriers out of the waveguide core and a p-doped core, among others [117].

If the pump pulse is longer than the cavity lifetime, a quasi-steady-state analysis can be used to solve for the interaction between the pump and probe pulses. To find the change in refractive index due to two-photon absorption, we must first find the change in index from carriers, i.e., the contribution of free carriers to refractive index. My analysis here follows [118, 119].

The refractive index, n is given as

$$n^2(\omega) = \epsilon(\omega) = \epsilon_{\mathrm{b}} + 4\pi\chi_{\mathrm{f}}, \tag{2.85}$$

where ϵ is the relative permittivity of the medium, and $\epsilon_{\mathrm{b}} = 1 + 4\pi\chi_{\mathrm{b}}$; χ_{b} is the contribution of bound charges to the susceptibility, and χ_{f} is the contribution of free charges. The equation of motion for carriers in a harmonic electric field, $\mathbf{E}\exp(j\omega t)$, is [119]

$$m^*\ddot{\mathbf{x}} = -e\mathbf{E}\exp(j\omega t), \tag{2.86}$$

where m^* is the effective mass of the carrier, and e is the electron charge. I have assumed that the damping term is negligible. The solution to this equation is

$$\mathbf{x} = \frac{e\mathbf{E}}{m^* \omega^2} \exp(j\omega t). \tag{2.87}$$

The corresponding contribution to polarization may be written as

$$\begin{aligned} \mathbf{P} &= -\frac{4\pi N_{\mathrm{free}} e^2 \mathbf{E}}{m^* \omega^2}. \qquad (2.88) \\ &= 4\pi \chi_{\mathrm{f}} \mathbf{E}, \qquad (2.89) \end{aligned}$$

where N_{free} is the free carrier density. We define the plasma frequency, ω_{p}, as:

$$\omega_{\mathrm{p}}^2 = \frac{4\pi N_{\mathrm{free}} e^2}{m^*}, \tag{2.90}$$

which gives

$$4\pi \chi_{\mathrm{f}} = -\frac{\omega_{\mathrm{p}}^2}{\omega^2}, \tag{2.91}$$

so

$$n^2 = \epsilon(\omega) = \epsilon_{\mathrm{b}} - \frac{\omega_{\mathrm{p}}^2}{\omega^2}, \tag{2.92}$$

Since there is no imaginary term above, the refractive index is real. Then,

$$\begin{aligned} n^2 &= \epsilon_{\mathrm{b}} - \frac{\omega_{\mathrm{p}}^2}{\omega^2} \qquad (2.93) \\ \Rightarrow 2n \frac{\mathrm{d}n}{\mathrm{d}\omega_{\mathrm{p}}} &= -2\frac{\omega_{\mathrm{p}}}{\omega^2}. \qquad (2.94) \end{aligned}$$

Since $\omega_{\mathrm{p}} \ll \omega$ for optical frequencies,

$$\begin{aligned} \frac{dn}{d\omega_{\mathrm{p}}} &= -\left(\frac{1}{\epsilon_{\mathrm{b}} - \omega_{\mathrm{p}}^2/\omega^2}\right)^{1/2} \left(\frac{2\omega_{\mathrm{p}}}{\omega^2}\right) \qquad (2.95) \\ &= -\frac{1}{\sqrt{\epsilon_{\mathrm{b}}}} \left(\frac{2\omega_{\mathrm{p}}}{\omega^2} + \frac{\omega_{\mathrm{p}}^3}{\epsilon_{\mathrm{b}} \omega^4}\right). \qquad (2.96) \end{aligned}$$

Now that we know the dependence of refractive index on carriers (via the plasma frequency), we have to consider the dependence of carrier concentration on intensity for two-photon absorption, which is the effect of interest. The absorption cross-section for two-photon absorption increases linearly with laser intensity, so the atomic transition rate increases as the square of intensity [120]. If we define a two-photon absorption coefficient, α_2, we can write the rate equation for the free carrier density, N_{free}, as

$$\frac{\mathrm{d}N_{\mathrm{free}}(t)}{\mathrm{d}t} = \frac{\alpha_2}{2\hbar\omega} I^2_{\mathrm{pump}}(t) - \frac{N_{\mathrm{free}}(t)}{\tau_{\mathrm{free}}}, \tag{2.97}$$

where ω is the pump beam frequency, I_{pump} is the pump beam intensity, and τ_{free} is the free carrier lifetime. From eqs. 2.90, 2.96, and 2.97,

$$\frac{\mathrm{d}n}{\mathrm{d}P_{\mathrm{bus}}} \propto \mathcal{I}^3. \tag{2.98}$$

Since the change in refractive index scales as $\mathcal{I}^3$, the switching power can be reduced dramatically for moderate intensity enhancements. I will make use of this to demonstrate all-optical logic in chapter 6.

A similar analysis can be used to show that the intensity enhancement in micro-rings boosts four-wave mixing as $\mathcal{I}^4$ [47].

2.12 The electro-optic effect

Microresonators can be tuned with temperature [43,67], refractive index change by carrier injection [65,121], and the electro-optic effect. I will use the electro-optic (EO) effect later in this work for demonstrating tuning. I chose to use the EO effect because it has the best potential for low-loss and high-speed operation. The electro-optic effect is related to the nonlinear susceptibility of the material, so we can use the values of $\chi^{(2)}$ or r (the linear EO coefficient), and $\chi^{(3)}$ or s (the quadratic EO coefficient) to choose the material system (GaAs or InP in the case of III-V semiconductors) for operation at the signal wavelength. For GaInAsP, Adachi and Oe provide analytical expressions for the linear electro-optic effect in [122], and the quadratic electro-optic in [123]. However, published data is of limited usefulness because of the wide range of parameters in the material and waveguide design, and the detuning of signal wavelength from the bandgap. As we go closer to the bandgap, the electro-optic effect becomes stronger, albeit at the expense of increased insertion loss. Nevertheless, the published data can prove useful as a sanity-check on experimental results. My analysis here is adapted from Boyd [120].

The general form of the nonlinear polarization is [120]

$$P_i^{\mathrm{NL}}(t) = 4\pi \left(\chi_{ijk}^{(2)} E_j E_k + \chi_{ijkl}^{(3)} E_j E_k E_l\right), \tag{2.99}$$

where repeated indices imply summation and c.g.s. units are used. InP and its quaternaries have a tetragonal structure, and belong the crystal class 422. The non-vanishing elements of the tensor $\chi^{(2)}$ for this class are $xyz = -yxz, xzy = -yzx, zxy = -zyx$. Of the 81 elements of the tensor $\chi^{(3)}$, 21 are nonvanishing, which are:

$$\begin{gathered}
xxxx = yyyy, zzzz \\
yyzz = xxzz, \quad yzzy = xzzx, \quad xxyy = yyxx, \\
zzyy = zzxx, \quad yzyz = xzxz, \quad xyxy = yxyx, \\
zyyz = zxxz, \quad zyzy = zxzx, \quad xyyx = yxxy.
\end{gathered}$$

Consider the case where the direction of propagation is z, which is in-plane for the wafer, and the x-axis is the direction of crystal growth, (100), i.e, out-of-wafer-plane. In the presence of a constant electric field along $\mathbf{e}_1$, and harmonic field, $E_\mathrm{i}\cos(\omega t)\mathbf{e}_1$, the nonlinear polarization, $P_1^{\mathrm{NL}}(t)$, has the form

$$\begin{aligned}
P_1^{\mathrm{NL}}(t) &= 4\pi \left\{\chi_{111}^{(2)} E_1(t)^2 + \chi_{1111}^{(3)} E_1(t)^3\right\} \\
&= 4\pi \left\{\chi_{111}^{(2)} \left[E_\mathrm{i}\cos(\omega t) + E_\mathrm{dc}\right]^2 + \chi_{1111}^{(3)} \left[E_\mathrm{i}\cos(\omega t) + E_\mathrm{dc}\right]^3\right\} \\
P_1^{\mathrm{NL}}(\omega, t) &= 4\pi \left\{\chi_{111}^{(2)} \left[2E_\mathrm{dc}E_\mathrm{i}\cos(\omega t)\right] + \chi_{1111}^{(3)} \left[3E_\mathrm{dc}^2 E_\mathrm{i}\cos(\omega t)\right]\right\}. \qquad (2.100)
\end{aligned}$$

In the last equation above, I have used $P_1^{\mathrm{NL}}(\omega, t)$ to indicate that I am considering only that part of the polarization which oscillates at the signal frequency; the other components oscillate at 2ω or just add a constant background.

The nonlinear polarization has two terms: the first is linear in E_{dc}, and gives rise to the linear electro-optic effect. The second is quadratic in E_{dc}, and causes the quadratic electro-optic effect.

We can now use the properties of $\chi^{(2)}$ for the InP system: since $\chi^{(2)}_{111} = 0$, the relevant effect for the polarization and direction of electric field chosen is the quadratic effect. Then,

$$P_1^{\mathrm{NL}}(\omega, t) = 4\pi \left\{ \chi^{(3)}_{1111} \left[3E_{\mathrm{dc}}^2 E_{\mathrm{i}} \cos(\omega t) \right] \right\}. \tag{2.101}$$

Since $n^2 = 1 + 4\pi\chi_{\mathrm{eff}}$,

$$n(\omega) = n_0(\omega) + \frac{6\pi\chi^{(3)}_{1111} E_{\mathrm{dc}}^2}{n_0(\omega)}, \tag{2.102}$$

for the direction of the constant electric field and the polarization chosen. This is referred to as the quadratic electro-optic effect since the refractive index can be varied as the square of the electric field.

Near the band-edge, the quadratic effect is caused primarily by the Franz-Keldysh effect in bulk, and the quantum-confined Stark effect (QCSE) in multiple-quantum-well (MQW) waveguides. The two effects are related; Miller and co-workers have shown that the Franz-Keldysh effect is a limiting case of the QCSE [124]. Typical values of $\chi^{(3)}$ for InP are $\sim 10^{-13}$ cm^2/W [125]. The quantum-confined quadratic electro-optic effect, or the QCSE, arises from bandgap shrinkage, which shifts the excitonic resonance closer to the signal wavelength [119, 126]. The resultant change in the absorption coefficient causes a change in refractive index via the Kramers-Krönig relations. The Franz-Keldysh effect has a similar mechanism, except that excitons aren't involved; when a bias is applied, the carriers move apart in bulk materials, which destroys the exciton resonance. The exciton resonance is maintained in quantum wells due to carrier confinement [127]. The quantum-confined effect is stronger than the bulk effect.

Although both the linear and quadratic electro-optic effect can be described by the nonlinear susceptibility, they have traditionally been described in terms of the linear and quadratic electro-optic coefficients. We have [120, 128]

$$\Delta n_1 = -\frac{1}{2}\Gamma n_{0,1}^3 r_{11} E_1 - \frac{1}{2}\Gamma n_{0,1}^3 s_{1111} E_1^2, \tag{2.103}$$

where $E_1\mathbf{e}_1$ is the electric field, $n_{0,1}$ is the refractive index in the absence of field for the out-of-plane polarization, Γ is the confinement factor, r_{11} is the linear electro-optic coefficient (contracted notation), and s_{1111} is an element of the quadratic electro-optic coefficient tensor. For the InP system, $r_{11} = 0$. If we choose to define s for the waveguide (which may be composed of more than one material, as in the case of multiple-quantum-well guides), we can use $\Gamma \approx 1$ because most of the light is in the core for the high-index-contrast waveguides we use in this work. However, in general, s is defined for the material. The quadratic electro-optic coefficient, s_{1111}, can be found with a quadratic fit to the measured data on refractive index versus electric field.

CHAPTER 3

ANISOTROPIC DRY-ETCHING

Etching of semiconductors or other materials refers to a process of removing material from an exposed surface. By masking a portion of the chip or wafer surface (using a lithography tool), we can write a desired pattern on the surface of the semiconductor. Etching can be achieved with physical or chemical means. In either case, the etching can be described by its directional nature as anisotropic or isotropic. In the case of isotropic etching, the rate of removal of the semiconductor material – the etch rate – is the same in all directions. In anisotropic etching, the etch rate is direction dependent. Specifically, if the etch rate is much higher in one direction than the other, we can get deeply-etched columnar structures, or pedestals. Therefore, anisotropic etching is important for the fabrication of pedestal waveguides.

Anisotropy can be achieved by the use of stop-etch crystal planes in some semiconductors [129], but, in general, anisotropy is achieved using dry-etching. In dry-etching, highly reactive uncharged and charged species are formed from a gas mixture using a high-frequency field, and are accelerated toward the target by a bias and appropriately positioned vacuum pumps. The unmasked regions of the target sputter off, or adsorb the reactive species, a reaction occurs, and the (usually gaseous) by-products desorb from the surface [130].

For vertical sidewalls, the gas pressure must be low enough to prevent scattering of the reactive species from collisions with other reactive and non-reactive species, i.e., the mean free path should be large. The bias should be high to ensure the reactive and non-reactive species impinge upon the surface with sufficient energy to initiate sputtering, adsorption, and/or a chemical reaction. The flow-rate should be high enough to ensure that adequate amounts of reactive species are present so that the reaction is rate limited.

Process development revolves around choice of reactants, gas pressure, flow-rate, bias and/or power, choice of platen (based on insulating or conducting, hardness, reactivity, etc.), and choice of mask materials. In some cases, such as inductively-coupled-plasma-reactive-ion-etching (ICP-RIE), it is possible to select both the bias and the power coupled into the plasma, while in others, such as parallel-plate (capacitively-coupled-plasma) reactive-ion-etching (RIE), the user can select either the bias or power. Obviously, the number of experiments needed to optimize processes in such experiments is quite high, so usually the parameter space is restricted by fixing one of more variables, and investigating the others with a design-of-experiment approach [99, 100].

In this chapter, I will discuss the indium phosphide etching capability developed for this project. The discussion will concentrate on the InP etch process; details of all the processes used are in the appendix B. Although dry-etching of indium phosphide is by no means a unique achievement, the variation in reaction chambers used in various clean-room facilities means that processes have to be tailored for the machine in use. I optimized the surface morphology based on scanning electron micrographs of the etched sidewalls, which is a qualitative assessment, so a design-of-experiment approach was not used; quantification of sidewall morphology requires an atomic-force microscope with the capability of scanning vertical surfaces, which was not available. The gas mixture, choice of carrier (anodized aluminum), and gas pressure were based on recommendations from the manufacturer. I varied the etch-time-to-clean-time ratio to achieve the results shown.

The etch results from the best process available prior to process development for this project for the Plasmatherm 790 Series RIE are shown in Fig. 3.1.

3.1 Dry-etching of indium phosphide

Indium phosphide can be etched by RIE, ICP-RIE, reactive ion beam etching (RIBE), or chemically assisted ion beam etching (CAIBE), using a suitable combination of gases such as methane, hydrogen, chlorine, silicon tetrachloride, hydrogen bromide, nitrogen, argon, and xenon. When optimized, most processes provide good surface and sidewall morphology. Methane-hydrogen-argon-based processes are typically slow, can be carried out at room temperature. The slow etch rate can be a mixed blessing: although it may take a long time to achieve the desired depth, it affords excellent control. Chlorine-based chemistries require high temperature for the desorption of indium trichloride, a reaction by-product, which is a non-volatile liquid at room temperature. They have high etch rates and are better suited if the machine in use has automatic end-point detection systems (a spectrometer and/or laser interferometer), or the device design allows greater latitude in etch depths.

Chlorine-based dry-etching of indium phosphide was first reported in 1980 by Coldren et al. [131–133]. Methane-hydrogen-argon-based etching of indium phosphide was first proposed and demonstrated by Niggebrügge in 1986 [134]. Since then, there have been many studies of methane- and methane-chlorine-based chemistries, with RIE, ICP-RIE, RIBE, and CAIBE, notably those by Hayes et al. [135, 136], Pearton et al. [137–139], Constantine et al. [140, 141], McNabb et al. [142], Matsutani [143–150], Schramm et al. [151, 152], Qiu

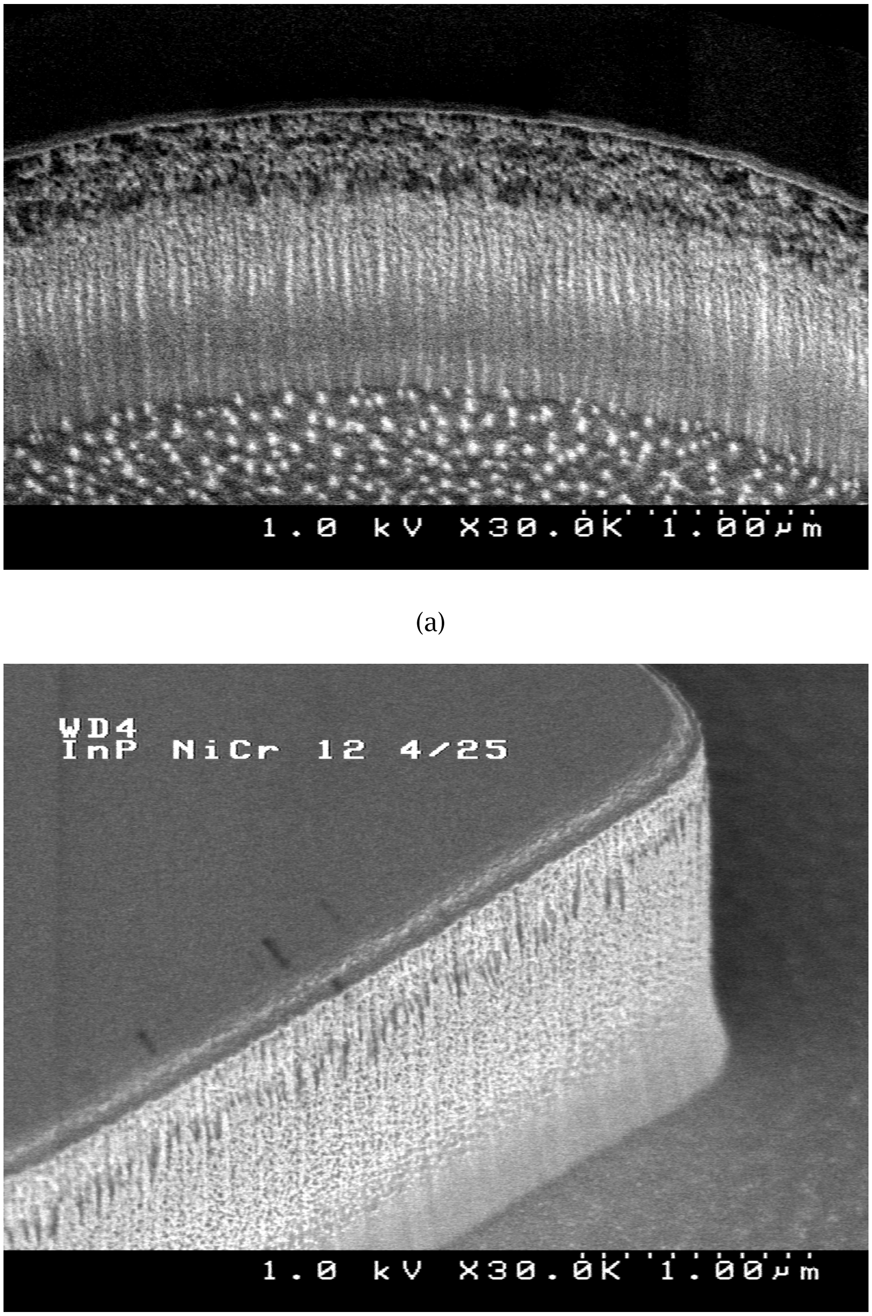

(a)

(b)

Figure 3.1: LPS InP etch prior to process development for this project. (a) Ni mask. (b) NiCr mask.

et al. [153], and Feurprier et al. [154–158].

3.2 Requirements for indium phosphide micro-ring devices

Indium phosphide micro-ring devices require facet-quality vertical sidewalls. Low-loss operation requires roughness of few tens of nm or less (usually designated as $\lambda/20$, where λ is the wavelength of operation in the material), otherwise, power may be coupled into a contra-directional mode [74] or may be lost due to scattering [75]. Polarization-preserving operation requires high verticality, usually less than 5 deg from vertical [159]. The target etch depths during process development were $\sim 1\ \mu$m (for vertically-coupled devices, chapter 4), $\sim 3\ \mu$m (for laterally-coupled devices, chapter 5), and $\sim 4.5\ \mu$m (for active laterally-coupled devices, chapter 7).

3.3 Indium phosphide etch process

For the devices fabricated during the course of this work, I chose the methane chemistry due to availability of the gases and equipment. Before the fabrication of devices for this work, I optimized an indium phosphide etch recipe for surface morphology on a Plasmatherm 790 series RIE [102].

The process uses a CH_4-H_2(-Ar) plasma for etching, alternated with an O_2 plasma for polymer removal, both with an 8 inch anodized aluminum platen. The etching was initially performed by subjecting exposed areas of the InP sample to a CH_4-H_2-Ar plasma; later, I used only CH_4-H_2. Argon sputters the holder and the sputtered material lands on the sample; using only methane and hydrogen helps avoid this problem (determined using EDS by William Vanderlinde).

The etch mechanism and the cause of anisotropy have been studied by Hayes et al. [135]. A recent study of the etch by-products by Feurprier et al. [156] using mass spectrometry found them to be organo-indium compounds, charged hydrocarbon species of the form C_nH_m and ionized phosphine. The hydrocarbon species form a polymer on the sidewalls, which acts to protect them and maintain verticality, but can cause problems if allowed to build-up. So it is important to cycle the etch and clean steps; the etch-to-clean time ratio is an important parameter and the quality of the etch is related to this ratio. A separate report by Lee et al. [160] used X-ray microanalysis and Auger electron spectroscopy to study the etched InP surface, which was found to have deposits of In-Si-P oxides, which could be removed by dilute HF. This is consistent with my experience of the effect of cleaning the sample with buffered hydrofluoric acid (BHF).

3.4 Plasmatherm 790 Series RIE

The Plasmatherm 790 Series RIE used for this project is a parallel-plate, single-chamber, manual loading RIE with a 13.56 MHz RF source and an 8 inch electrode. Power is coupled to the plasma by capacitive-coupling. There are two holders, made of graphite and anodized aluminum. The gases available are CHF_3, O_2, SF_6, CH_4, H_2, and Ar. Low pressure operation is usually between 20 – 50 mT, and is used for anisotropic etching.

3.5 Chamber conditioning

Most dry-etching processes require a conditioned, or ‘seasoned’ chamber. Chamber conditioning affects the plasma physically and/or chemically [161]:

1. Physical: The insulating or conducting nature of coatings on the chamber walls affects the electromagnetic boundary conditions, which changes the fields, resulting in changes in the current and power density in the discharge. In addition, other properties, such as the secondary electron emission coefficient, work function and wall impedance are affected.
2. Chemical: Radicals form and recombine on the chamber wall, and the wall can act as a source and sink for radicals, affecting the radical lifetime, and hence, reaction rate.

Methane-based etching of InP is very sensitive to the chamber condition and contaminants. I found that if the chamber had been exposed to other chemistries, the result of the etch step was inconsistent. For consistent results, it was important that prior to etching the sample, the chamber be exposed to a conditioning step, which deposits polymer on the chamber walls [135]. This serves to stabilize the chamber chemistry by coating the chamber walls and the holder and 'tacking' down any contaminants, in addition to affecting the plasma as noted above. In the absence of chamber conditioning, there would be a very rough grass-like feature on the unmasked regions of the sample, which obscured the features being defined.

A typical preparation run would involve wiping the chamber walls with 2-Propanol, followed by wiping with deionized water, running a 3 hr. or longer O_2-plasma chamber clean process, followed by at least 33 cycles of the etch-and-clean process, all with the same anodized aluminum platen which was later used for the etch process. This is an essential step in the absence of a dedicated chamber for etching InP, as materials as diverse as photoresists, polyimides, Si, SiO_2, SiON, Si_3N_4, Ti, various polymers, and InP are all etched or used as masks in the same chamber with multiple etching chemistries and multiple platen. Some processes have solid by-products, which must be removed mechanically. For example, when SF_6 and H_2 are used together, one by-product is sulfur, which covers all exposed surfaces in the chamber, and must be wiped off the chamber walls.

Note: Since this work was done, Kuldeep Amarnath has found that the long conditioning step above can be replaced with a 20 min. run of the etching step.

3.6 Mask materials

I studied various masks, such as Ni, NiCr, Ti, SiO_2, and bilayer masks of Ti-SiO_2, and Cr-SiO_2. I patterned the masks on 15×15 mm^2 epi-ready InP chips. Nickel and nichrome are popular masks because they have small grain size, are very hard, and resistant to most chemistries. The mask materials are reviewed in greater detail in [139, 141, 162–167]. The Cr-SiO_2 mask is not described here, but is used in chapters 5 and 7.

3.7 Mask patterning

I patterned Ni and NiCr masks by liftoff using OiR 908 20HC positive photoresist, which was spun on the samples at 3500 RPM, followed by a pre-bake at 90 °C for 60 s. Next, I exposed a standard pattern in a 10× i-line stepper, performed a post-exposure bake at 120 °C for 60 s, and developed the pattern in OPD 4262 for 60 s, followed by rinsing in deionized (DI) H_2O. After treatment with H_2SO_4 diluted with DI H_2O as $1 : 20$ for 60 s to remove any native oxide, followed by rinsing with DI H_2O, I evaporated the metal onto the samples. The Ni was evaporated with a CHA Mark 40 electron-beam evaporation system, and the NiCr with a home-made resistive-thermal evaporation system. Finally, the chips were immersed overnight in 2-Propanone (Acetone) for liftoff, rinsed successively in Methanol, 2-Propanol, DI H_2O, and 2-Propanol, and dried with N_2.

Ti, SiO_2 and Ti-SiO_2 masks were patterned in RIE with a photoresist mask. I cleaned the InP test samples with 2-Propanone, Methanol, 2-Propanol and deionized water and immersed them in OPD 4262 to improve the adhesion of the subsequently deposited SiO_2. I deposited SiO_2 by plasma enhanced chemical vapor deposition (PECVD) in an Oxford Plasmalab PECVD system at 300 °C for a thickness of 120, 300, and 500 nm for various samples. 100 nm Ti was deposited on some of the 500 nm SiO_2-covered samples. I deposited only 100 nm Ti on other InP test samples. The samples were coated with photoresist and patterned as before. Following this, I transferred the pattern to the SiO_2-only samples by RIE with CHF_3-O_2, to the Ti-SiO_2 samples by etching Ti with SF_6 and SiO_2 with CHF_3-O_2 and to the Ti-only samples by etching Ti with SF_6. To remove the photoresist, I subjected the sample to a short oxygen plasma clean, followed by immersion in warm 1-Methyl-2-Pyrrolidone for $>$ 15 min., and rinsing successively with 1,1,1-Trichloroethane, 2-Propanone, Methanol, 2-Propanol, deionized water, and 2-Propanol, followed by blow-drying with nitrogen.

3.8 NiCr masks

I carried out initial process development using a NiCr mask, which I abandoned later in favor of SiO_2 and Ti-SiO_2 masks; the NiCr liftoff was not very reliable due to the lithography equipment available then at LPS. Also, both NiCr and Ni are difficult to remove, so are best suited to applications where leaving the mask in place is not detrimental to device performance; using a sacrificial layer of silicon dioxide under the Ni or NiCr can ease mask removal. A more serious problem occurs due to the high temperatures involved in metal deposition, which hard-bakes or chemically breaks-down the (photo)resist liftoff mask so it doesn't dissolve in the solvent used for liftoff. It then acts as a micro-mask, resulting in unwanted grass-like structures around the edges of the pattern (Fig. 3.2). The nano-grass obscures the sidewalls and is usually close enough to the sidewalls to couple light out of the waveguide and cause loss. Ti and SiO_2 on the other hand, can be patterned by RIE with fluorinated chemistries (usually SF_6, CF_4 or CHF_3, and O_2). If the selectivity between the resist and the underlying titanium or silicon dioxide is high enough, we can get good pattern transfer. Although Ti and SiO_2 masks suffer from erosion [163], using a bilayer mask or a thick mask is usually enough to ensure mask erosion does not cause problems.

The first etch was carried out with seven cycles of 10 min. etches alternated with 1 min. oxygen plasma to remove polymer from sidewalls. The process pressure was 30 mT with D.C. bias of 440 V and gas flow rates of 8 sccm methane and 32 sccm hydrogen. This ratio was chosen based on the manufacturer's recommendation of a process for etching InP. The etch depth was 2.1 μm. The sidewall was extremely rough. I attributed this to the buildup of polymer on the sidewall during the etch step, which was not adequately removed.

In order to decrease the effect of polymer formation, I added 12.5 sccm of argon. Argon ions serve to sputter the InP off the sample ('ion-milling'). Also, I increased the clean time to 5 min.. Increasing the clean time gives better verticality but the effect of 'micro-masking' was still apparent.

To alleviate this, I decreased the etch time to 5 min. and ran the process for fourteen cycles, but there was little or no perceptible improvement. There was

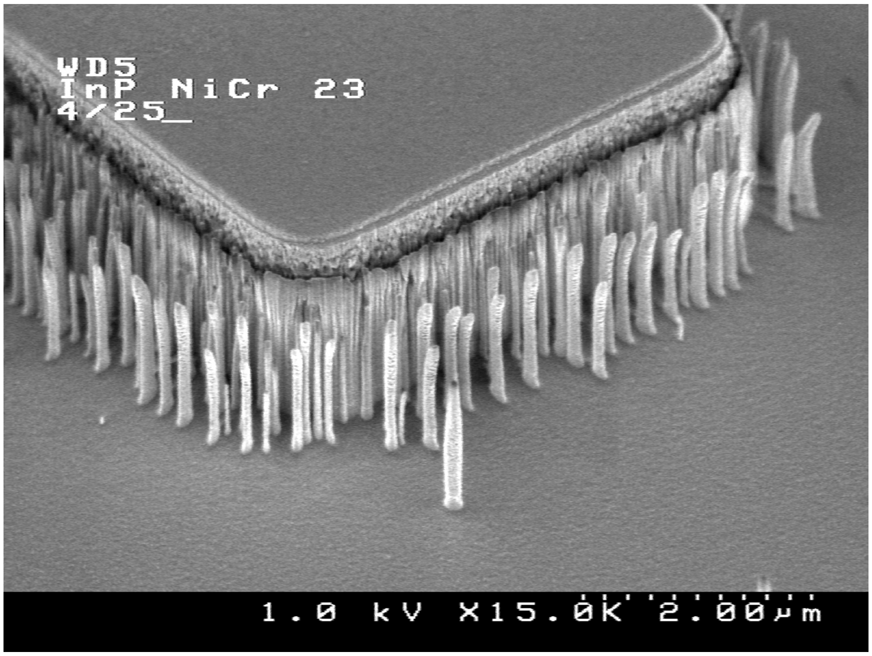

Figure 3.2: Micro-masking results in nano-grass (NiCr liftoff mask).

also some undercut of the mask on the sample, which may be due to excessive cleaning steps (which would remove too much of the protective polymer). I, therefore, decreased the cleaning step to 3 min. to get the result in Fig. 3.3, which shows a vertically grooved but otherwise smooth sidewall. The grooved feature is believed to be from the mask; this effect is not seen with other masks. I was thus able to get enough information from the NiCr-mask-based etching to show that the process would work if the mask definition problems were overcome, as shown in Fig. 3.3. Later, I used Ni masks, but it wasn't possible to deposit Ni in thicknesses of > 80 nm reliably as it delaminates. At the thickness of 80 nm, I found that Ni masks suffer from mask erosion.

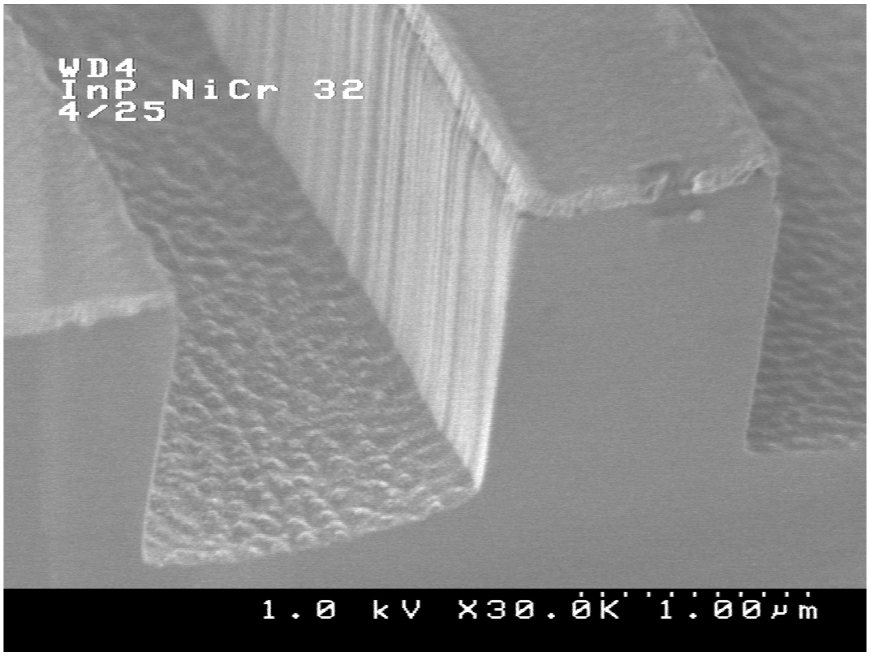

Figure 3.3: 3 μm-deep InP etch with NiCr mask.

3.9 Ti masks

Ti is a promising mask material for low-depth etches. Pattern transfer to Ti involves the use of SF_6 and a photoresist mask. The etch rate of Ti is very low for the anisotropic Ti-etch I studied for pattern transfer, which limited the thickness of Ti for this study to around 100 nm. Like SiO_2, it suffers from mask erosion for etches to depths > 1 μm. Also, Ti sometimes sputters and redeposits around the features being etched, causing the formation of a low fence-like structure around the waveguide sidewalls.

3.10 SiO_2 masks

It has previously been observed that SiO_2 is prone to erosion during dry-etching [165, 168]. Erosion becomes a problem at the mask edge as it introduces sidewall roughness. However, SiO_2 has the advantage that it can be patterned easily in an RIE with CHF_3-O_2 plasma, and can be removed in the same way after the etching is complete. Alternately, it may be removed in buffered hydrofluoric acid, which does not affect InP. I tested SiO_2 masks of thicknesses 120, 300 and 500 nm.

I found that the 120 nm thick SiO_2 mask had problems of mask erosion, beginning at 1 μm, and severe at the target of 3 μm (Fig. 3.4). This is alleviated to some extent by the use of a 300 nm thick film, but there is still some roughness just below the mask for a 3 μm deep etch. For a 1 μm-deep etch, however, a 300 nm thick film performs satisfactorily (Fig. 3.5). If this mask is used to etch deeper (4.8 μm), mask erosion becomes a big problem (Fig. 3.6).

By using a 500 nm-thick film, I could etch close to 5 μm depth with very little mask erosion (Fig 3.7), and demonstrate that the process does afford good verticality. It may be possible to keep increasing the thickness of SiO_2 masks to etch deeper. However, since I used a photoresist mask to pattern the SiO_2, erosion of the photoresist becomes a problem for very thick SiO_2 films. Therefore, in order to get good results for very deep etches, it became necessary to look at alternate masks.

3.11 Ti-SiO_2 masks

Ti-SiO_2 is the most promising of the masks tested for etches greater than 5 μm. Both Ti and SiO_2 can be patterned in an RIE (with SF_6 and CHF_3-O_2, respectively). The 100 nm-thick Ti film on top of the 500 nm SiO_2 film de-

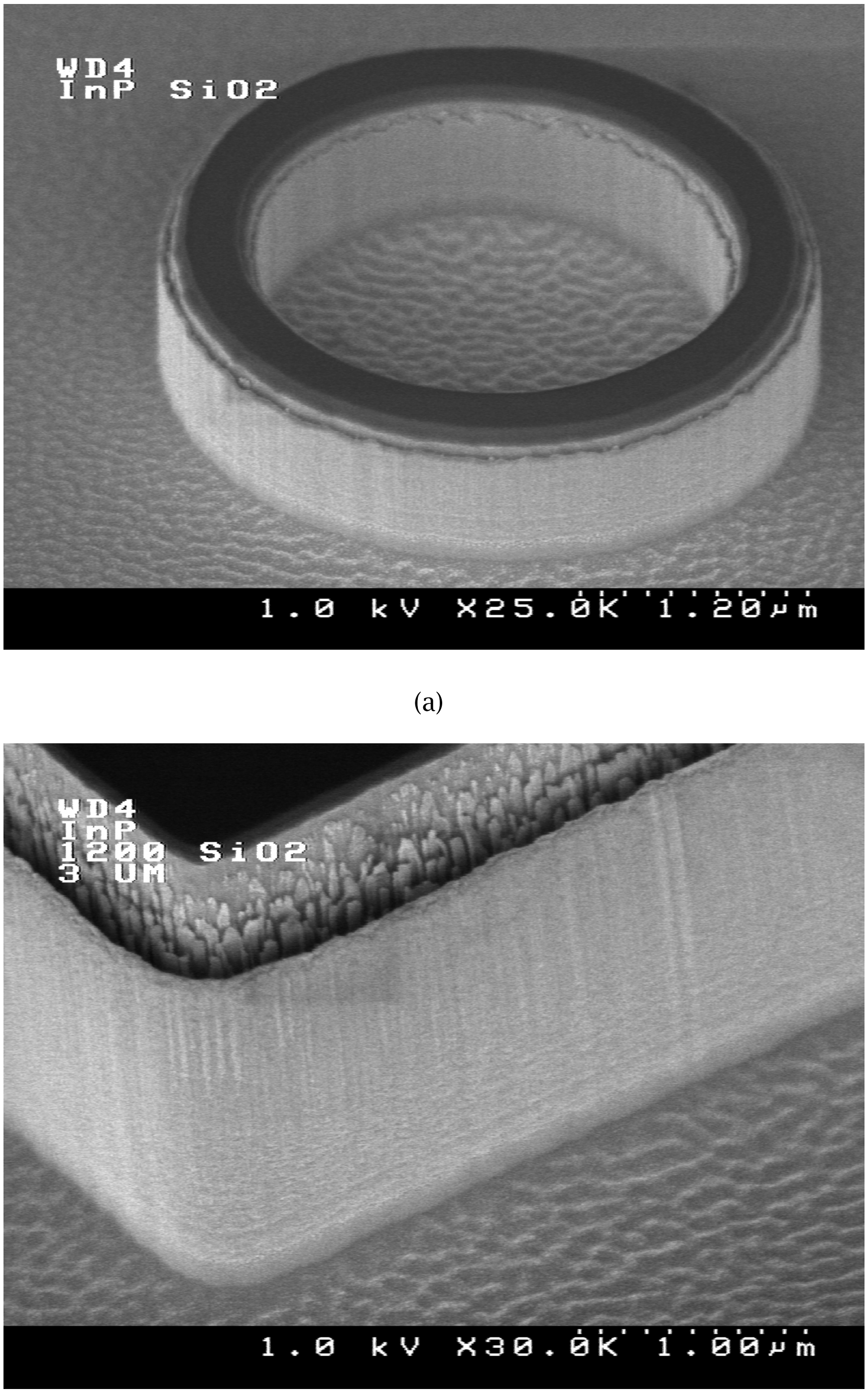

(a)

(b)

Figure 3.4: Mask erosion with a 120 nm-thick SiO_2 mask for different etch depths. (a) 1 μm. (b) 3 μm.

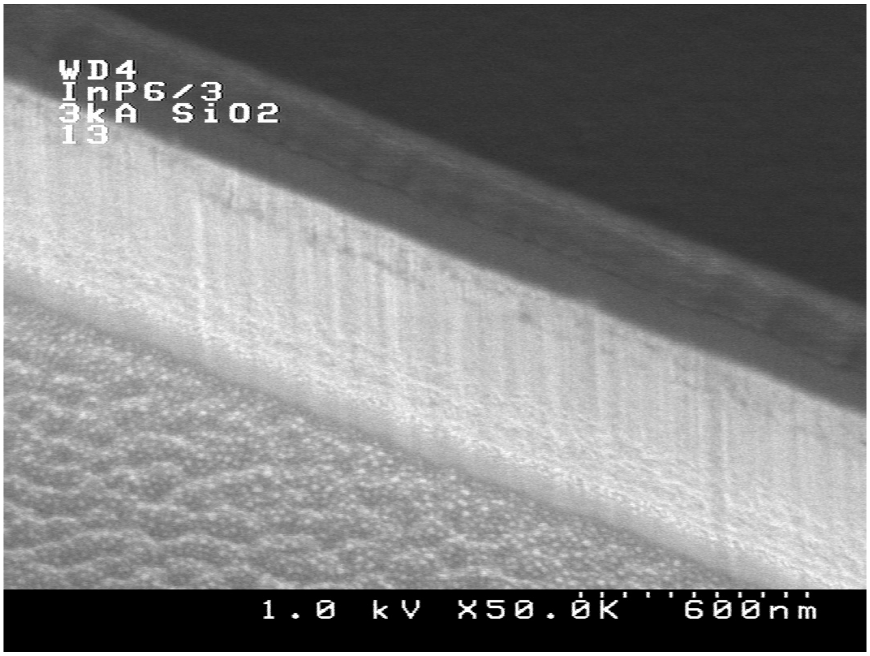

(a)

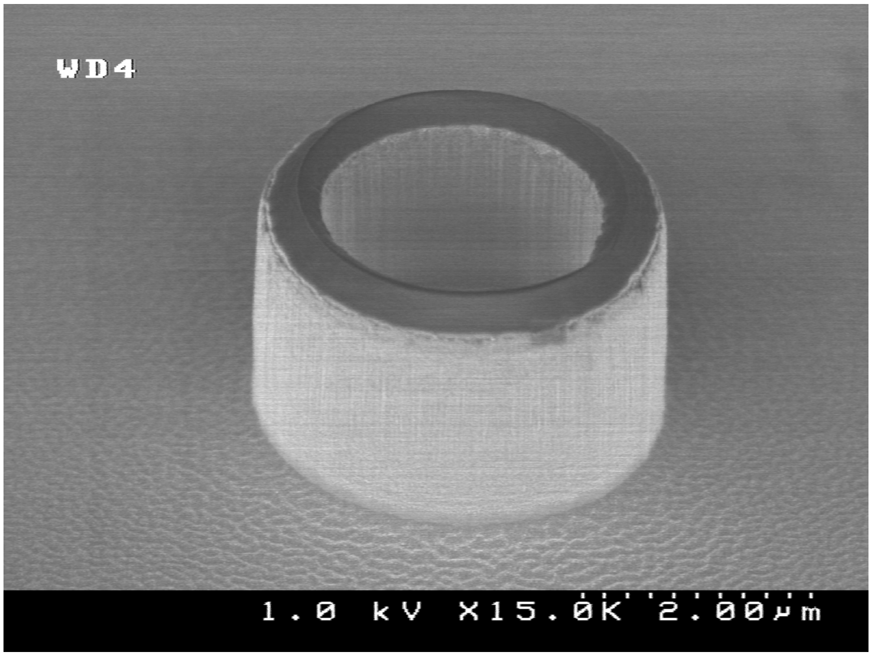

(b)

Figure 3.5: InP etch with 300 nm-thick SiO_2 mask. (a) 1 μm. (b) 3 μm.

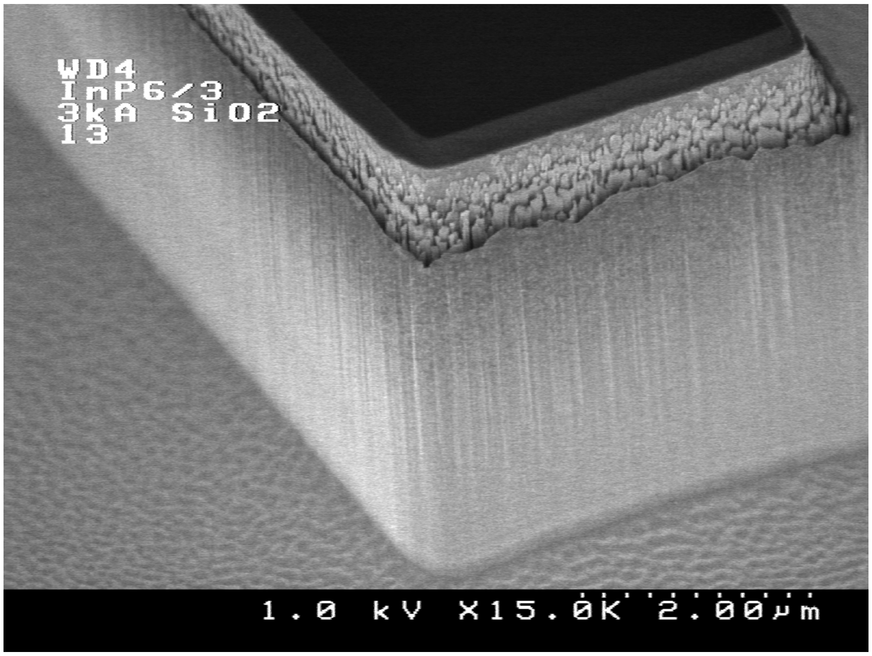

Figure 3.6: Severe mask erosion with 300 nm-thick SiO_2 mask.

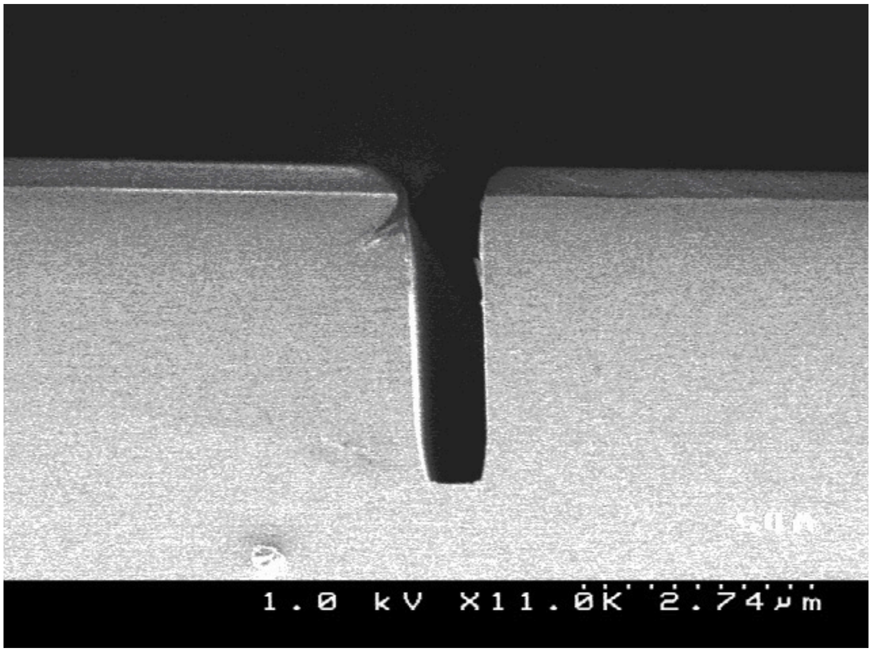

Figure 3.7: Illustration of etch verticality - the trench is 1 μm-wide.

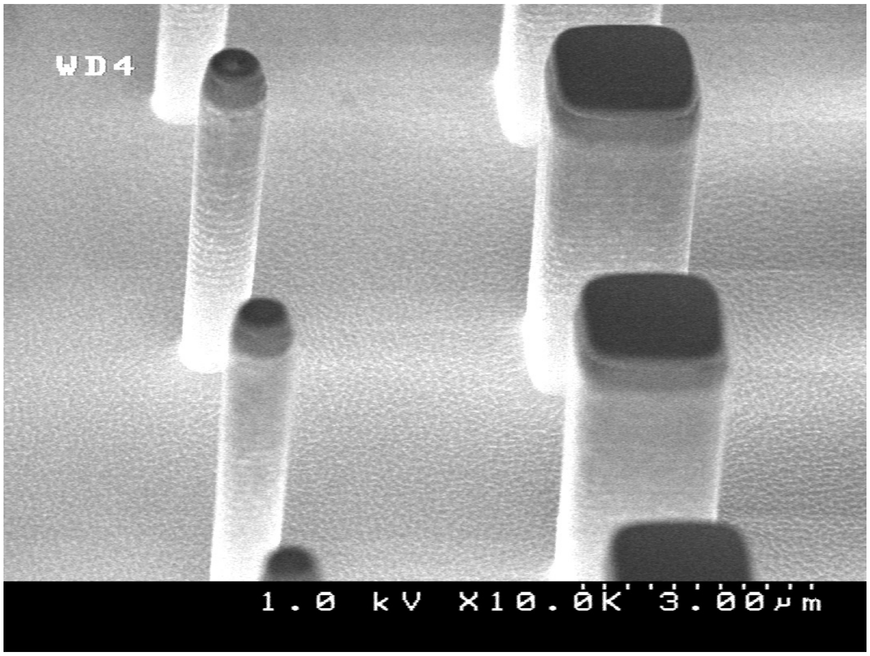

Figure 3.8: 5.5 μm-deep InP etch with Ti-SiO$_2$ mask.

creases mask erosion and the result is a very smooth etch for depths as high as 5.8 μm with little or no degradation of the mask (Figs. 3.8, 3.9, 3.10, 3.11). I have shown the sidewalls both with and without the mask, as polymer deposition and/or the formation of In-Si-P oxides during the etch process can obscure sidewall morphology (section 3.3). Removal of the mask also allows a better examination of the top surface, where mask erosion may have caused roughness. Since it is possible to fabricate very high aspect-ratio structures with this process, it may be useful for fabricating III-V MEMS [169, 170].

The choice of this bi-level mask is due to previous process development with SiO$_2$ masks and because it allows us to avoid using very thick Ti and SiO$_2$ films. Previously, Ti-Si$_3$N$_4$ bi-level masks have been studied by Qian et al. [167], who reported that the Ti film tends to sputter during the etch.

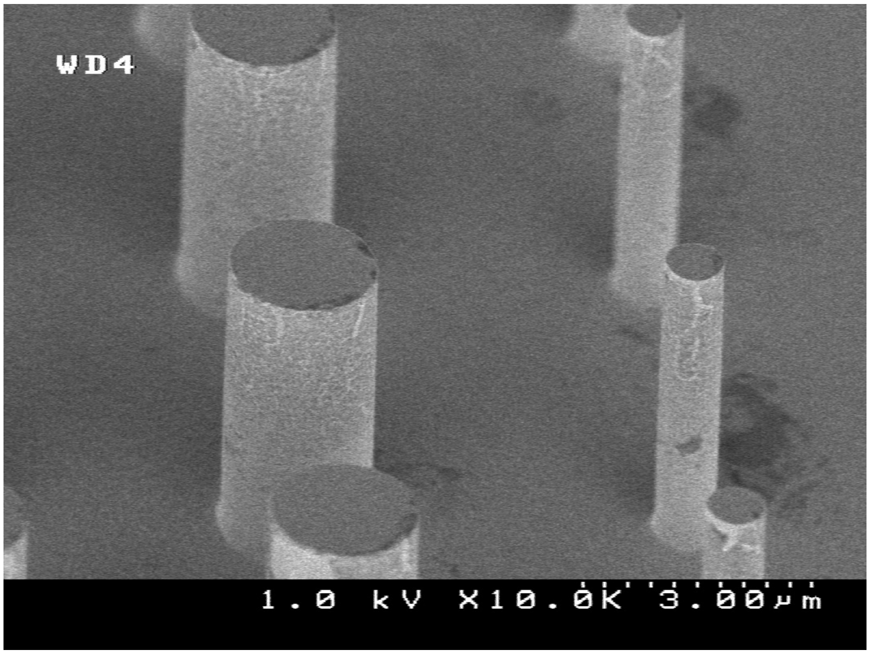

Figure 3.9: The same as Fig. 3.8, but after stripping the mask in BHF.

I do not observe any perceptible degradation of the Ti film with my process.

3.12 Mask selectivity

The selectivity between InP and SiO_2 in the processes using SiO_2 masks was around 50 : 1. Metallic masks and Ti-SiO_2 bi-level masks showed little or no degradation and the selectivity could not be measured for them.

3.13 Modified process

Although the CH_4-H_2-Ar-based etch process was quite successful, over time, the argon eroded the anodized aluminum plate in the RIE chamber and started sputtering aluminum onto the samples being etched. The result was that the

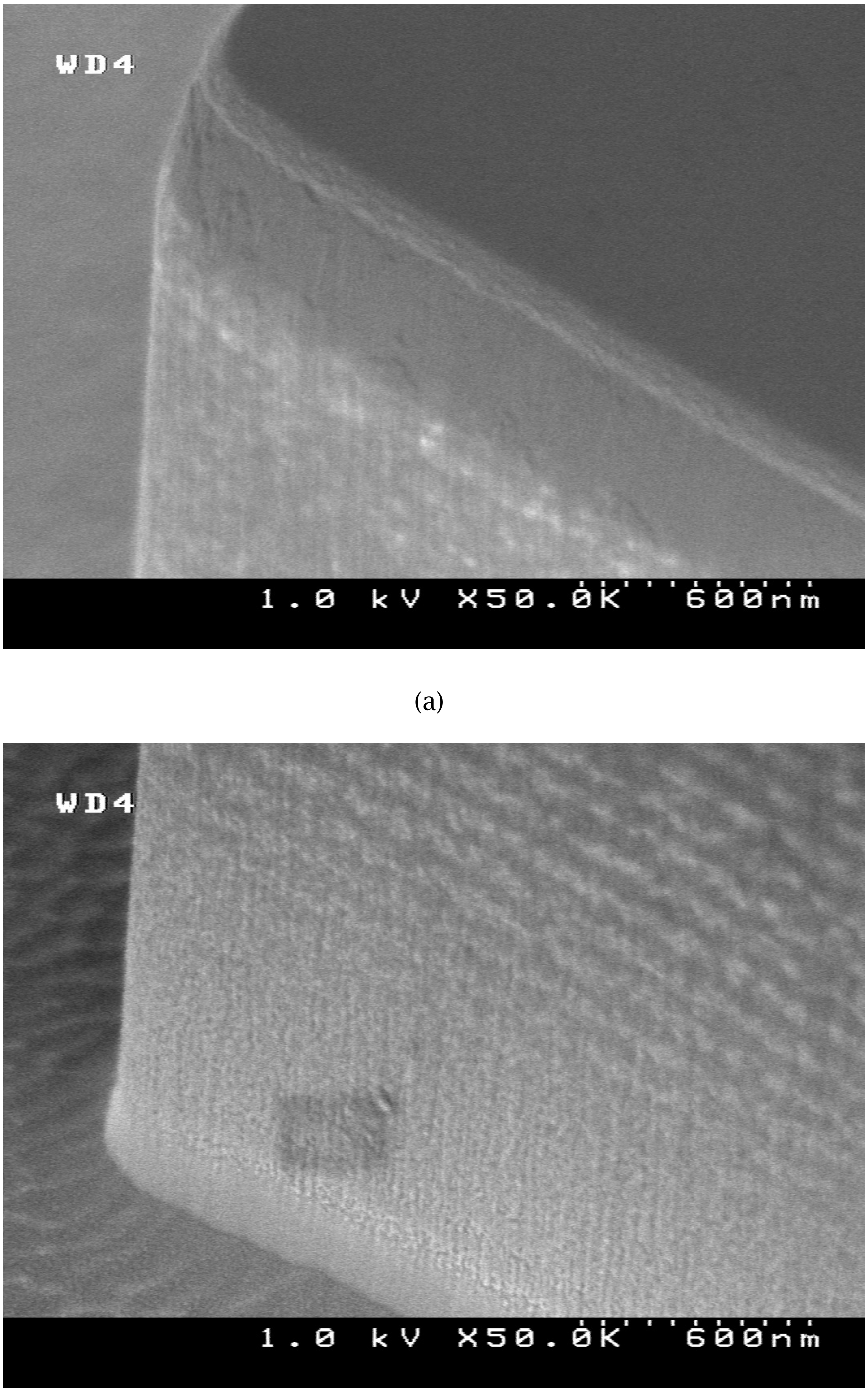

(a)

(b)

Figure 3.10: Detail of 5.5 μm-deep etch with Ti-SiO_2 mask. (a) Top of ridge. (b) Bottom of ridge.

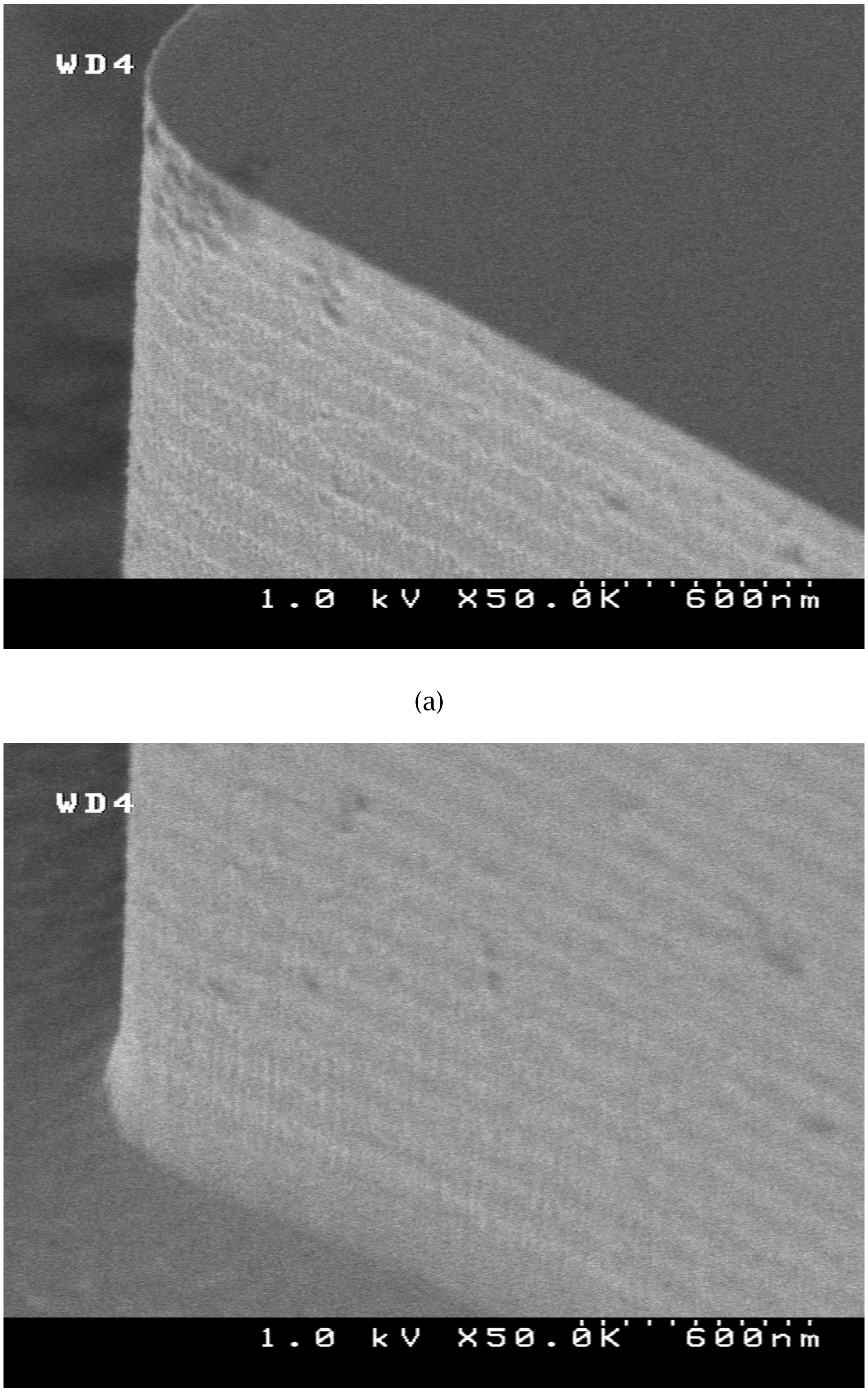

(a)

(b)

Figure 3.11: The same as Fig. 3.10, but after stripping the mask in BHF. (a) Top of ridge. (b) Bottom of ridge.

samples would be covered with nano-grass as the aluminum particles would act as masks. Replacing the plate with a freshly anodized one did not improve matters, possibly because of the quality of the replacement. So the etch step was modified to a CH_4-H_2 plasma with the same flow-rates, pressure, and bias; the etch rate did not change significantly, though the sidewall angle deteriorated to around 88 deg (Fig. 3.12).

3.14 Aspect-ratio dependence

Although during process development the aspect-ratio dependence of the etch process was not obvious, later results with small trench widths showed that the etch rate or depth was strongly dependent on the trench width for trench widths below 1 μm. This is summarized in Fig. 3.13. While this is not a problem for vertically-coupled devices (where there are no small gaps), it shows that the fabrication of laterally-coupled devices (which have small coupling gaps of the order of a hundred nm) will be affected because the coupling between the ring and the bus will be changed.

3.15 Comments

In this work, I used SiO_2 or Ti masks for vertically-coupled devices as the etch depth required was quite small (around 1 μm). Both masks were deposited first and then patterned by dry-etching with a photolithographically-patterned photoresist mask, the SiO_2 mask with a CHF_3-O_2 plasma, and the Ti mask with an SF_6 plasma. The laterally coupled devices were made with a Cr-SiO_2 mask. First a layer of SiO_2 was deposited, followed by patterning of a bilayer film of poly(methyl methacrylate) by electron-beam lithography. Then the Cr was

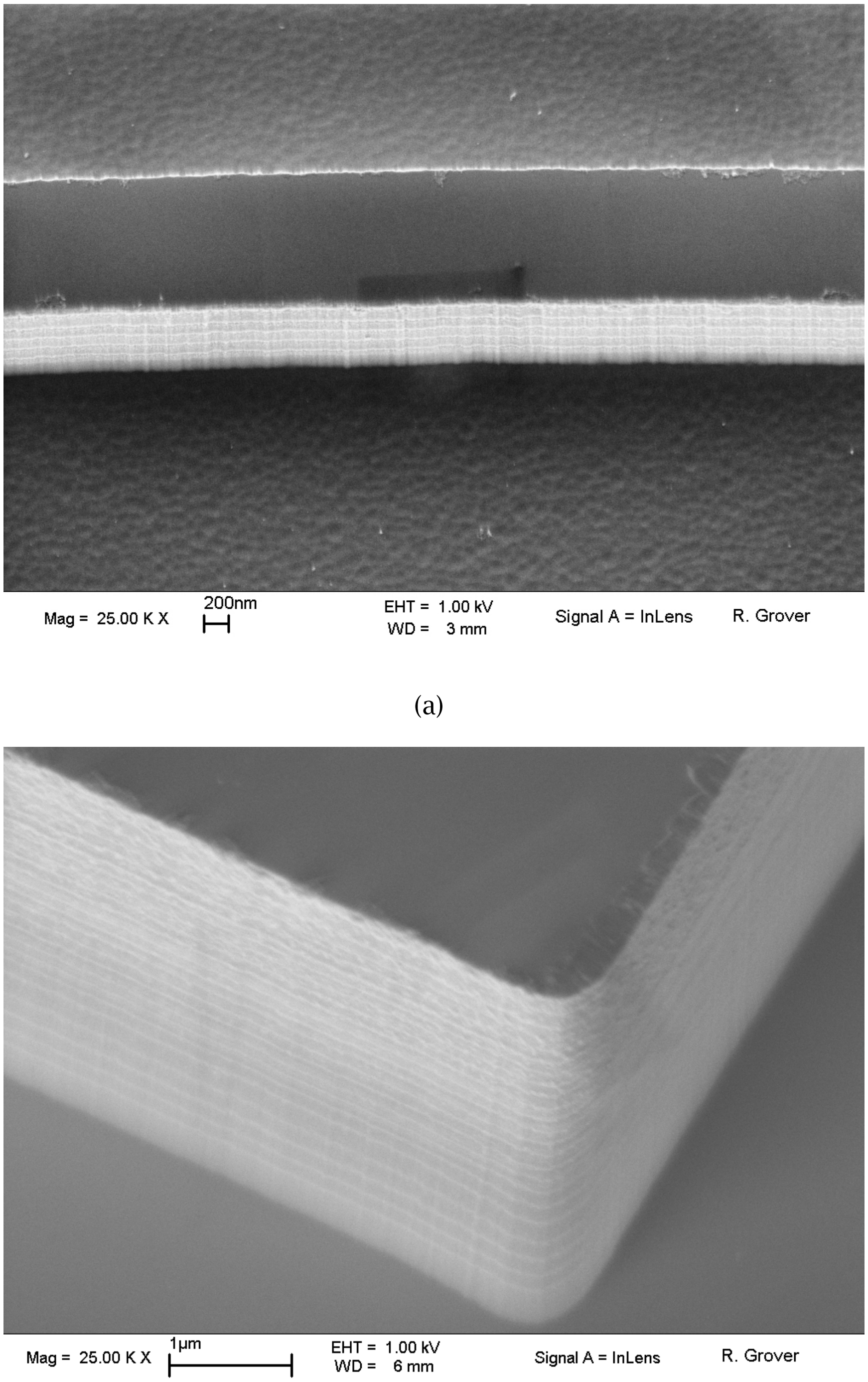

(a)

(b)

Figure 3.12: Etch quality without using argon. (a) 1 μm-deep etch. (b) 5 μm-deep etch (from D. P. Kelly and M. W. Pruessner).

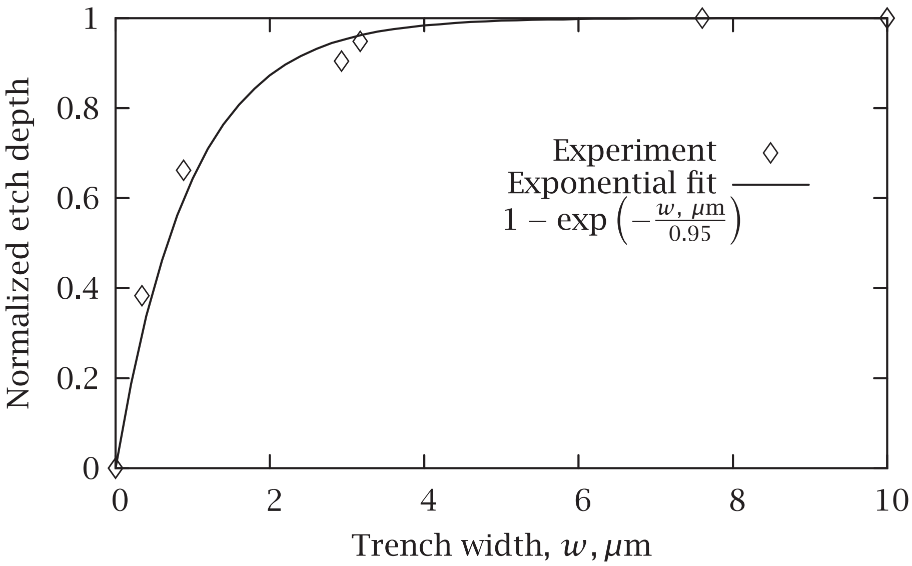

Figure 3.13: Aspect-ratio dependence of etch depth/rate.

deposited and patterned by liftoff, followed by dry-etching with CHF_3-O_2 to transfer the pattern into the underlying SiO_2. The SiO_2 was used to allow the removal of the Cr mask by dipping in BHF, which would dissolve the SiO_2 layer.

Many factors can cause the etch quality to deteriorate for methane-based etches, most notably contamination in the reaction chamber and changes in the chamber chemistry, which are best addressed by using chambers dedicated to the etching of one material. A significant drawback of the methane chemistry even when a dedicated chamber is available can be the slow etch rate. This can be overcome with the use of halogen-chemistries in an ICP-RIE with end-point detection systems (a laser interferometer and/or spectrum analyzer). In that case, fast etch rates can be obtained and the etch depth can be well-controlled. An example of an etch with HBr-N_2 is shown in Fig. 3.14.

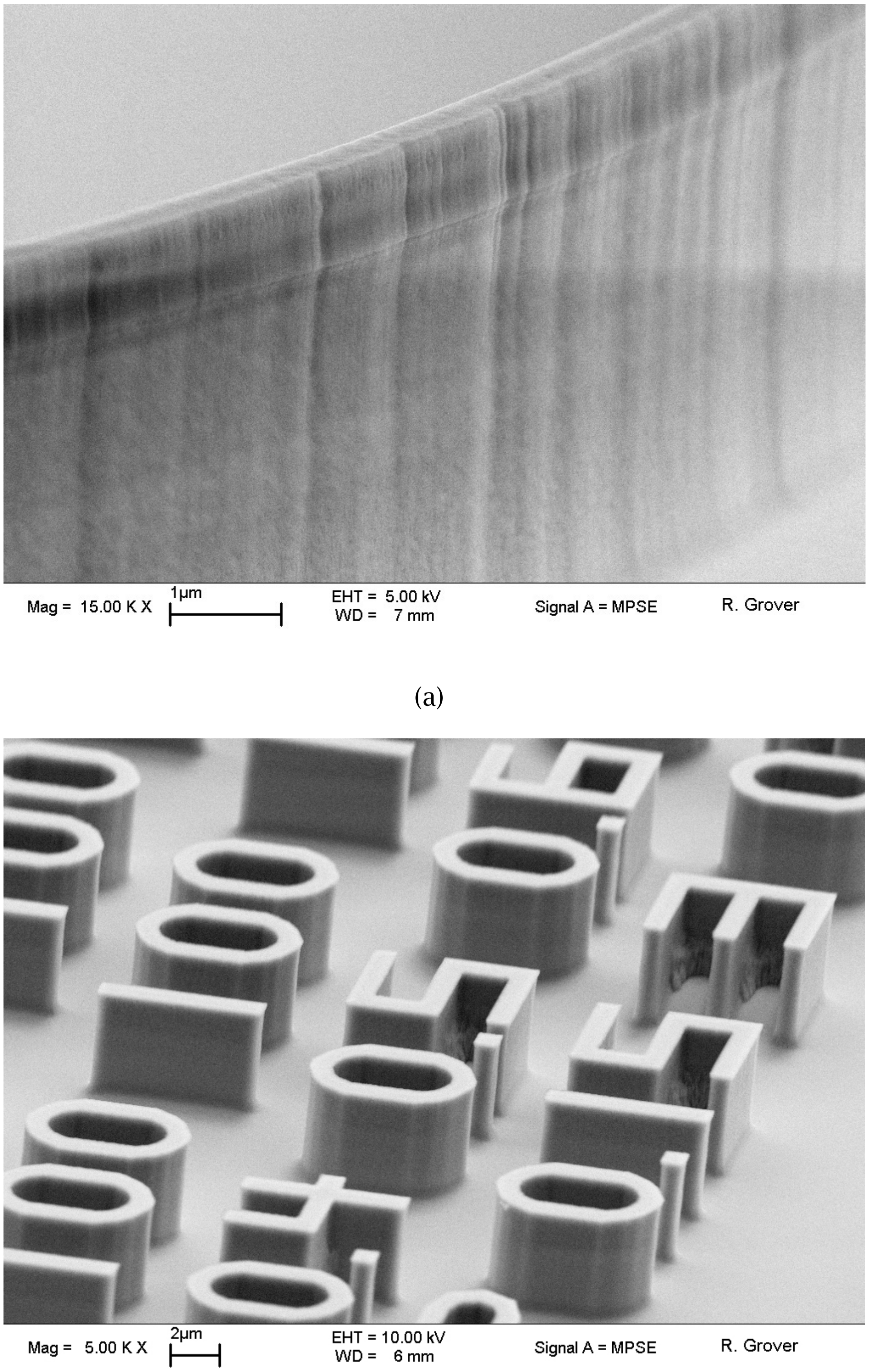

(b)

Figure 3.14: (a) and (b) 4 μm-deep etch with HBr-N_2 from Unaxis, USA, Inc. In (a), the mask of Cr-SiO_2 (50 nm/800 nm) has been left on the sample.

CHAPTER 4

PASSIVE MICRO-RING RESONATORS I: VERTICAL COUPLING

In this chapter I extend a fabrication technique developed originally for the GaAs-AlGaAs system [49] to GaInAsP-InP. This approach does not require regrowth and uses polymer wafer bonding followed by removal of the growth substrate to permit fabrication of waveguides on both sides of the epilayer. Previously, Tishinin et al. [59] proposed a regrowth-free fabrication technique to make vertically coupled structures in GaAs-AlGaAs by use of wafer bonding and IR back-side contact alignment. However, their approach used direct wafer-bonding, which is a difficult processing step. Further, they demonstrated microdisk resonators, which are inherently multi-mode. Efficient and useful channel-dropping filters require single-mode operation, well-controlled waveguide-to-micro-ring alignment, low propagating loss, and multi-ring filters for small channel spacing, which I demonstrate here.

4.1 Design

The design of the devices discussed in this chapter was based on earlier work by Absil et al. [49]. The layer structure was designed to mimic the corresponding GaAs-AlGaAs layer structure to use the same masks. Accordingly, the layer structure was originally designed to have two 500 nm-thick cores

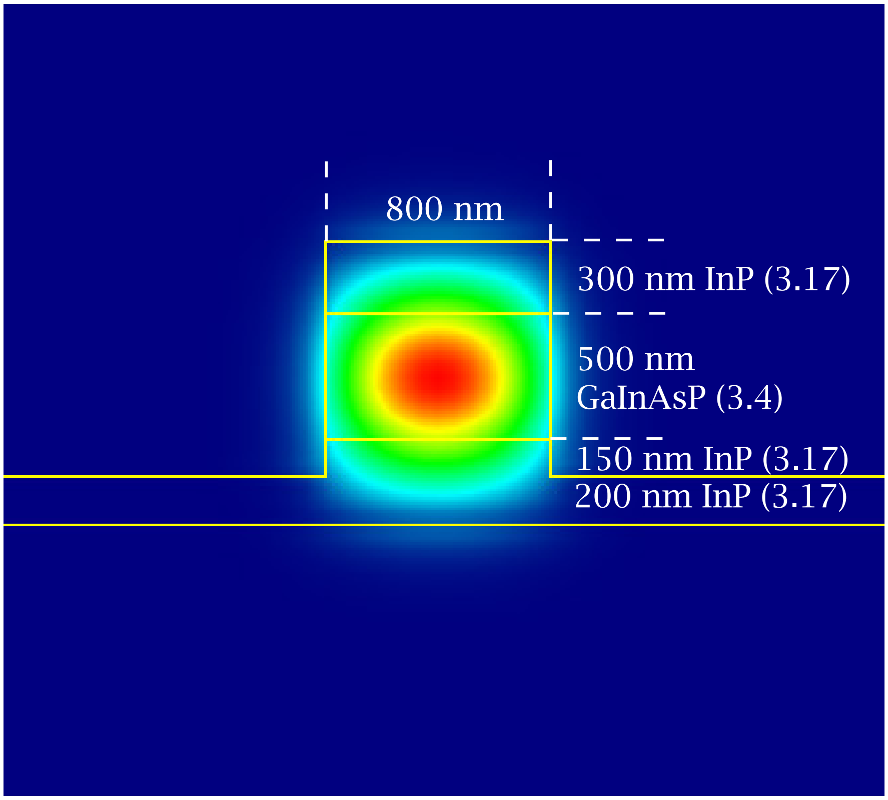

Figure 4.1: Designed waveguide mode and dimensions

with refractive index 3.4, separated by a 500 nm-thick InP mid-layer (refractive index 3.17), with 300 nm-thick InP claddings on the outside. The coupling between the ring and bus waveguides was nominally selected to be 10 %. To account for fabrication tolerances, a range of 'misalignments' were built-in. A simulation of the waveguide mode for the designed dimensions is shown in Fig. 4.1. Based on simulations, the effective index of the waveguide was estimated as 3.16. The FSR based on the designs for the 9.55 μm-radius rings was estimated as 12.6 nm, and for the 4.55 μm-radius rings as 25.6 nm; the bandwidth could not be designed as it depends on the etch process, which does not behave exactly the same across different runs.

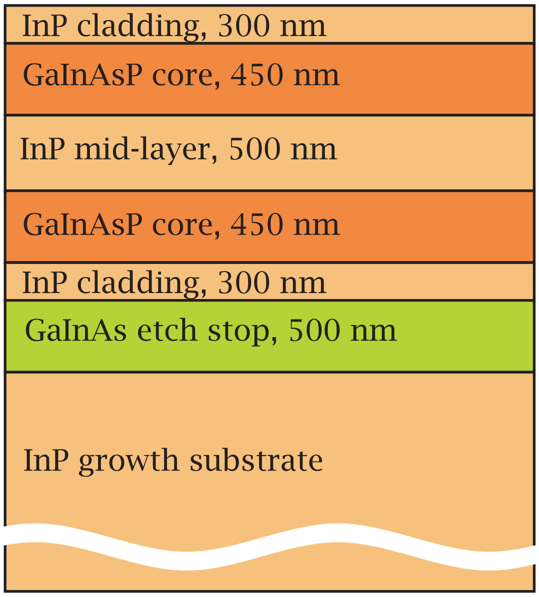

Figure 4.2: Layer structure used for fabrication of vertically coupled microrings. The ternary and quaternary layers are lattice matched to InP.

The wafer used for this work was grown at LPS using solid-source MBE by L. C. Calhoun. The layer structure consists of two 450 nm-wide GaInAsP cores of bandgap 1480 nm, with a cladding of InP (300 nm on the outside and 500 nm between) grown upon a 3 inch (7.62 cm) diameter Crystacomm InP substrate (InP(100) offcut 2° toward the $\langle 111 \rangle$A) by molecular beam epitaxy. The index of the core is approximately 3.4, and that of the cladding is 3.17. Below this is an etch stop of lattice-matched GaInAs to permit substrate removal by a selective chemical etch [93]. Coupling between the ring and the bus waveguides is achieved via the 500 nm InP layer between the two guiding layers. The core thickness is different from that designed because of problems in MBE calibration.

4.2 Process flow

I used a 10× i-line stepper for photolithography. I etched the features into a 400 nm-thick SiO_2 layer with a photoresist mask and a trifluoromethane-oxygen in a reactive ion etching system. I used the patterned SiO_2 as a mask to define the waveguides in GaInAsP-InP with a methane-hydrogen-argon plasma-based reactive ion etching process for smooth and vertical sidewalls [102].

First I etched the alignment keys to a depth of 2 μm to reach the GaInAs layer. I used these keys for processing both sides without requiring infrared back-side alignment. Following this, I etched the waveguide layer to a depth of 0.9 μm (Fig. 4.3(a)-(h)). Next, I bonded the sample to a GaAs transfer substrate using $\sim 1-2$ μm-thick benzocyclobutene (BCB), following the process described by Sakamoto et al. [171] (Fig. 4.3(i),(j)). I removed all but 100 μm of the growth substrate by chemo-mechanical polishing [92]. For the remaining growth substrate, I used H_3PO_4:HCl (1:1), which selectively etched the remaining InP and stopped at the GaInAs layer [93] (Fig. 4.3(k)-(l)). Finally, I removed the etch-stop layer with H_2O_2:H_2SO_4:H_2O (1:1:10), which selectively etches GaInAs over InP (Fig. 4.3(m)). This step cleared the other side of the epilayer for processing. I used the etched-through alignment keys to align the top layer to the lower layer. I etched the top layer to a depth of 0.9 μm (Fig. 4.3(n)-(t)). A 200 nm mid-layer was left between the waveguides in the fabricated device to decrease losses caused by leakage to the substrate. Finally, I encapsulated the sample in BCB to ensure refractive-index profile symmetry (Fig. 4.3(u)), thinned, and cleaved it for high-quality facets.

A ring made on the chip is shown in Fig. 4.4. The rough feature near the top is etch residue, left behind after removal of SiO_2 using a CHF_3-O_2 plasma. I subsequently found that there is no etch residue if the SiO_2 is removed with

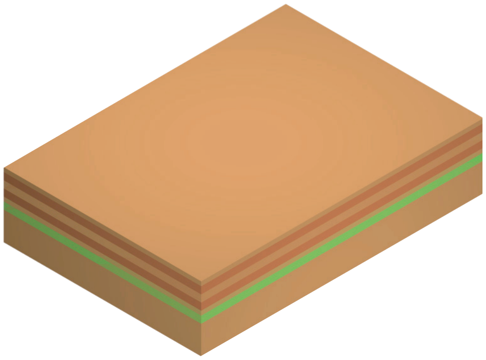

(a) Blank substrate.

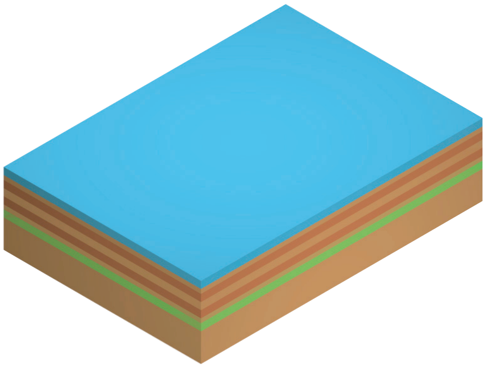

(b) Deposit SiO_2 in PECVD.

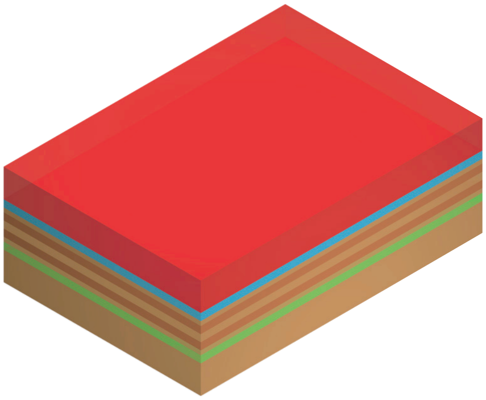

(c) Spin-on photoresist.

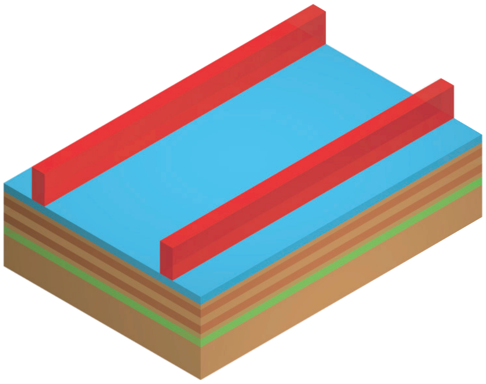

(d) Pattern photoresist.

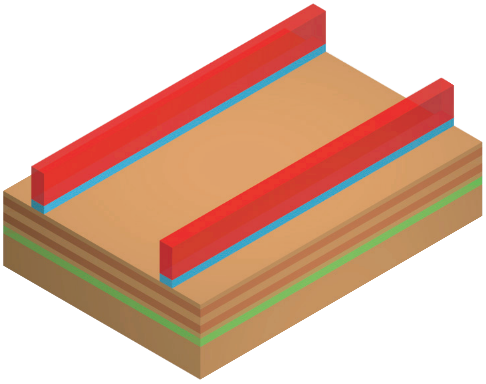

(e) Transfer pattern to SiO_2.

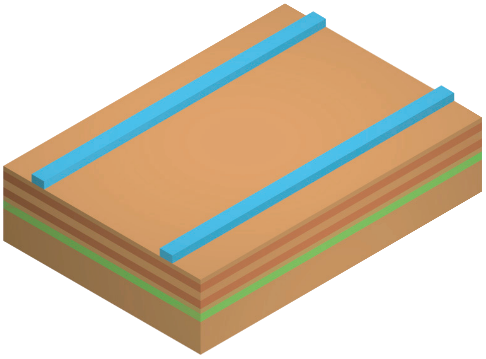

(f) Strip photoresist.

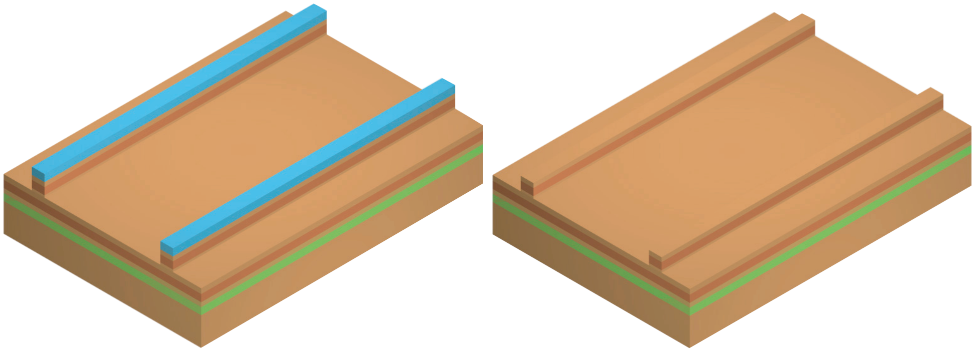

(g) Etch bus waveguides into epilayer. (h) Strip SiO_2.

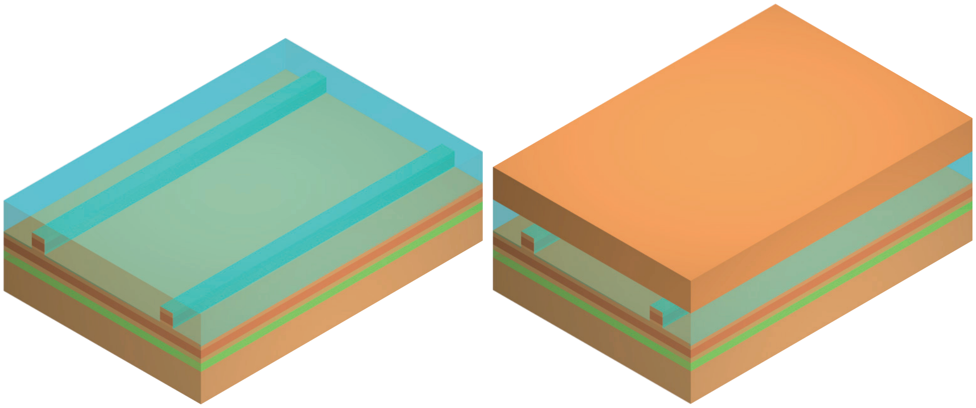

(i) Dispense BCB. (j) Bond to transfer substrate.

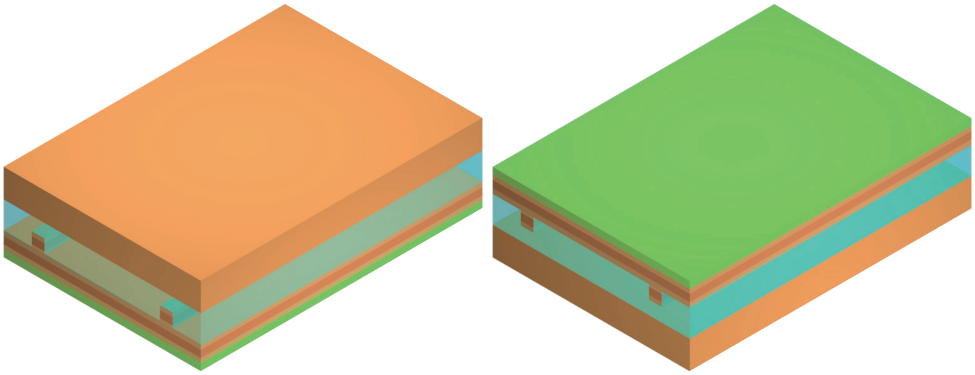

(k) Remove growth substrate. (l) Same as Fig. 4.3(k), but flipped.

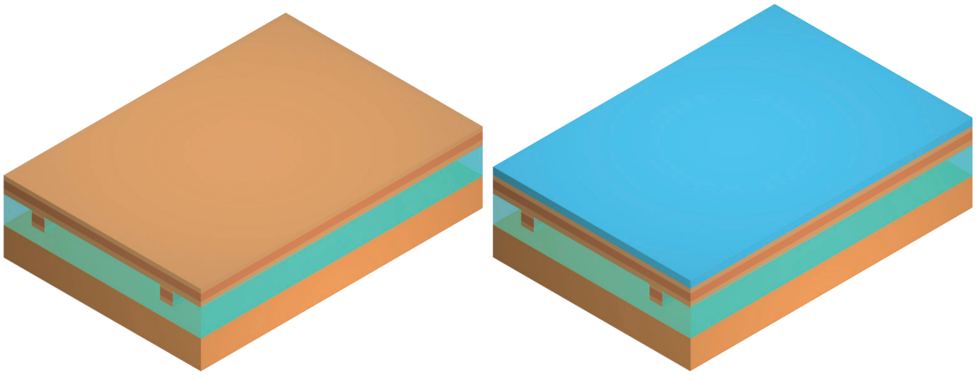

(m) Remove etch-stop.

(n) Deposit SiO_2 in PECVD.

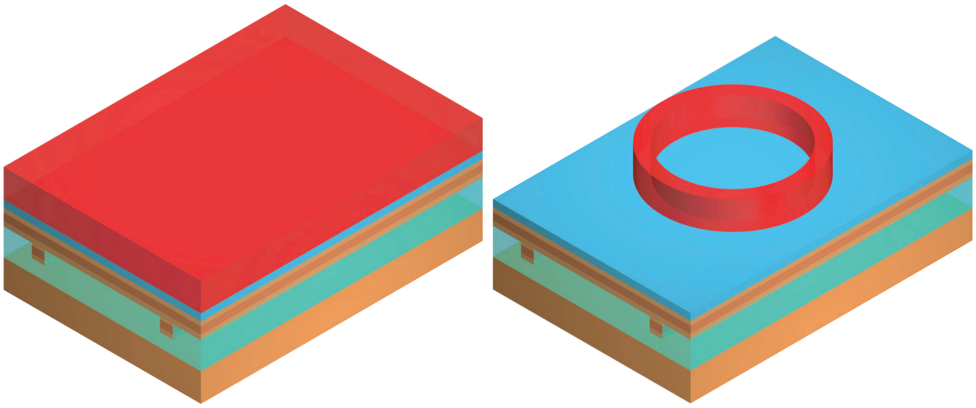

(o) Spin-on photoresist.

(p) Pattern photoresist.

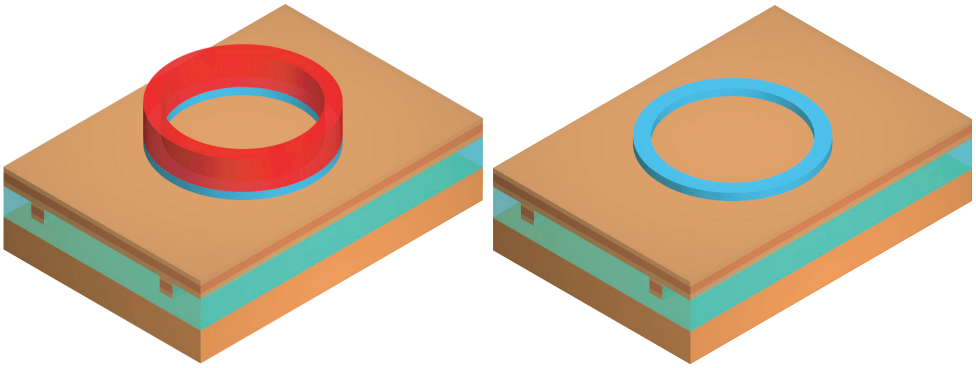

(q) Transfer pattern to SiO_2.

(r) Strip photoresist.

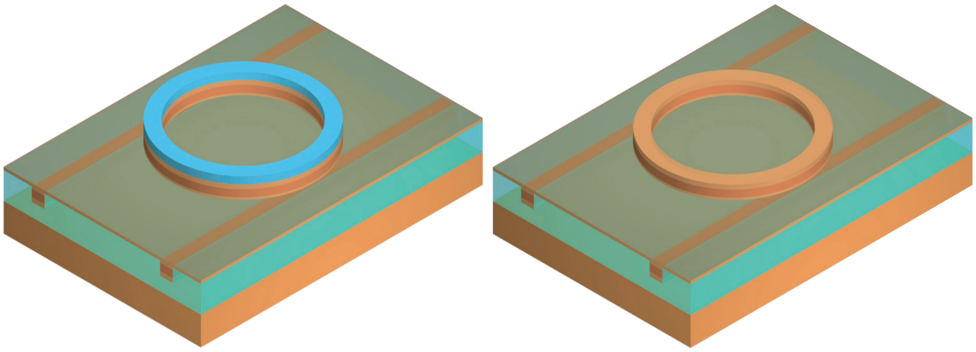

(s) Etch ring into epilayer. (t) Strip SiO_2.

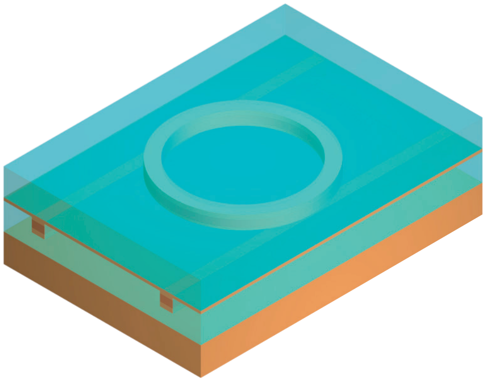

(u) Encapsulate in BCB.

Figure 4.3: Process flow for InP-based vertically-coupled micro-ring resonators. (The definition of alignment keys is not shown here.)

buffered hydrofluoric acid, and adopted it as the method for such removal.

The use of BCB provides a low-refractive-index (1.53 – 1.55) layer between the GaAs transfer substrate and the epilayer, making tightly confined waveguides possible on both device layers. Also, the BCB encapsulation provides the symmetric refractive-index structure that is required for identical micro-rings on both layers, allowing multi-ring resonators with rings on both layers. Leaving a thin layer of InP coupling layer (0.2 μm) reduces the effect of layer-to-layer misalignment [49]. This design also provides added mechanical strength to the structure for the BCB encapsulation. Finally, the alignment scheme, using a stepper and etched-through alignment keys, provides a high-quality layer-to-layer alignment with errors smaller than 0.25 μm (measured from on-chip verniers; Fig. 4.5). The fabricated single-micro-ring optical channel-dropping filter is shown in Fig. 4.6. Residuals from removal of the growth substrate caused the upper level to appear dirty.

4.3 Device characteristics

4.3.1 Single micro-ring devices

I obtained the device response by coupling S-polarized light (Fig. 4.7) from an external-cavity laser diode into the input waveguides and collecting the output, both with lensed optical fibers. The test setup was developed by Philippe Absil [172]; a schematic is shown in Fig. 4.8. The fabricated devices have waveguide widths of 0.8 μm and a mid-layer thickness of $\sim$ 0.2 μm. The waveguides were tapered at both the inputs and the outputs to 2.5 μm width to improve coupling efficiency to the input and output fibers. I tested single micro-ring resonators with radii of 4.55 and 9.55 μm. Dropped power was measured above the 1580 nm wavelength because the material exhibited sig-

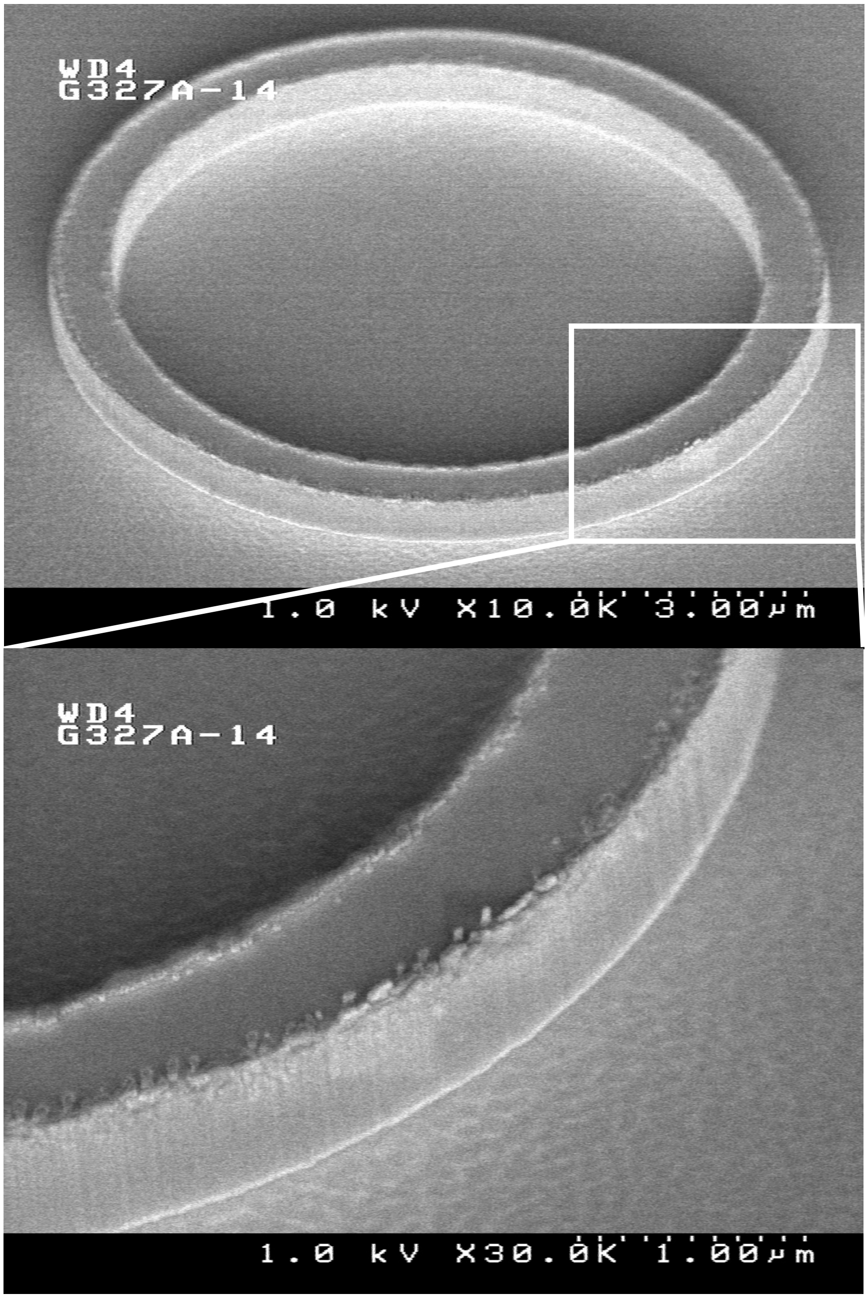

Figure 4.4: Dry etched ring waveguide.

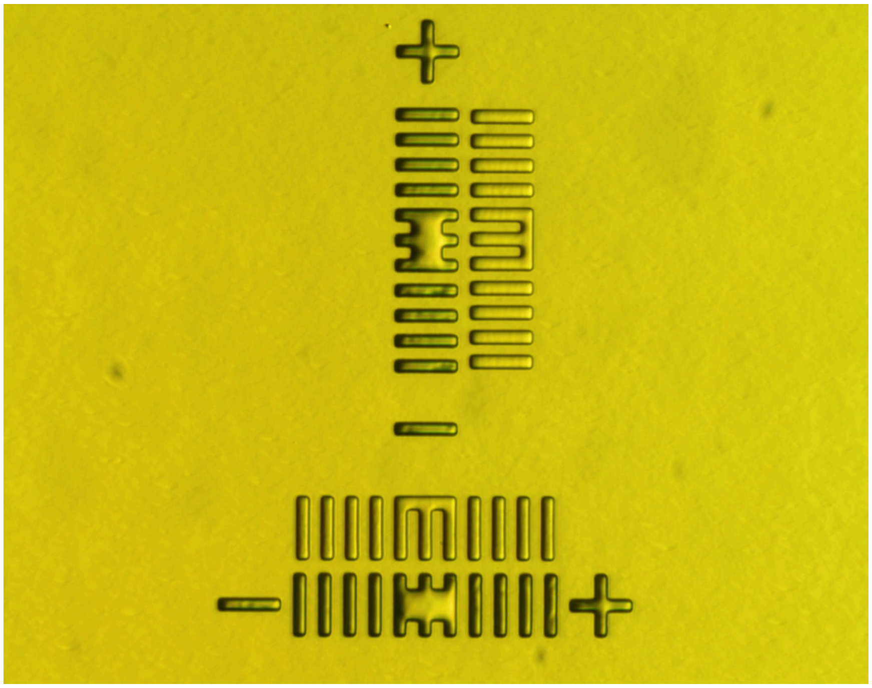

Figure 4.5: Alignment accuracy measured from on-chip verniers.

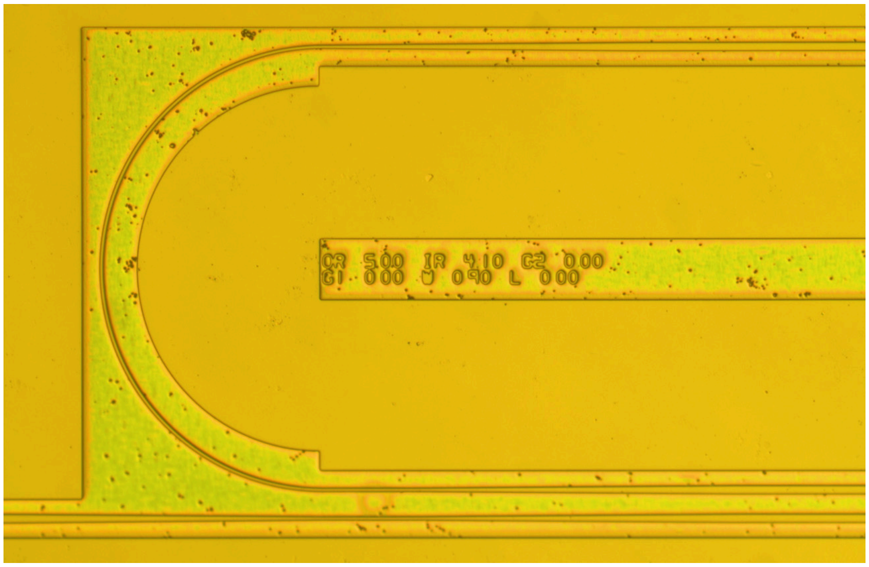

Figure 4.6: Optical micrograph of fabricated single ring add-drop filter with 5 μm radius ring on the lower level.

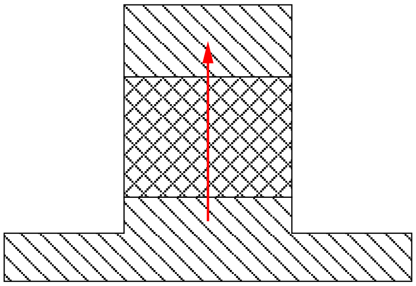

Figure 4.7: Polarization direction (arrow). The double hatched region represents the core of the waveguide. The polarization in use is referred to as 'S' based on the description of the polarizing beam-splitter cube used for the analysis.

nificant absorption below 1580 nm (Figs. 4.9, 4.10). (The bandgap of the core was lower than designed due to calibration problems in the MBE.)

The free spectral range of the 4.55 μm-radius resonators was 24 nm (design prediction was 26.6 nm), with a bandwidth near 0.6 nm (Fig. 4.9). The free spectral range of 10 μm-radius resonators was 13 nm (design prediction was 12.7 nm), with a bandwidth of 0.6 nm (Fig. 4.10). Single-ring resonators in an optical channel-dropping filter configuration exhibited Q values as great as 3000 (for the 9.55 μm-radius resonators). Based on a fit to the data, the coupling to the ring (for the 9.55 μm-radius rings) is estimated as 11 %, which is very close to the designed value of 10 %, and may have been affected by the size of the core. Control waveguides (untapered, straight) made on both levels had losses of $\sim$ 15 cm^{-1} or less. Subsequently fabricated devices (on a different wafer) had Qs of 6500 or more for 9.55 μm radius rings.

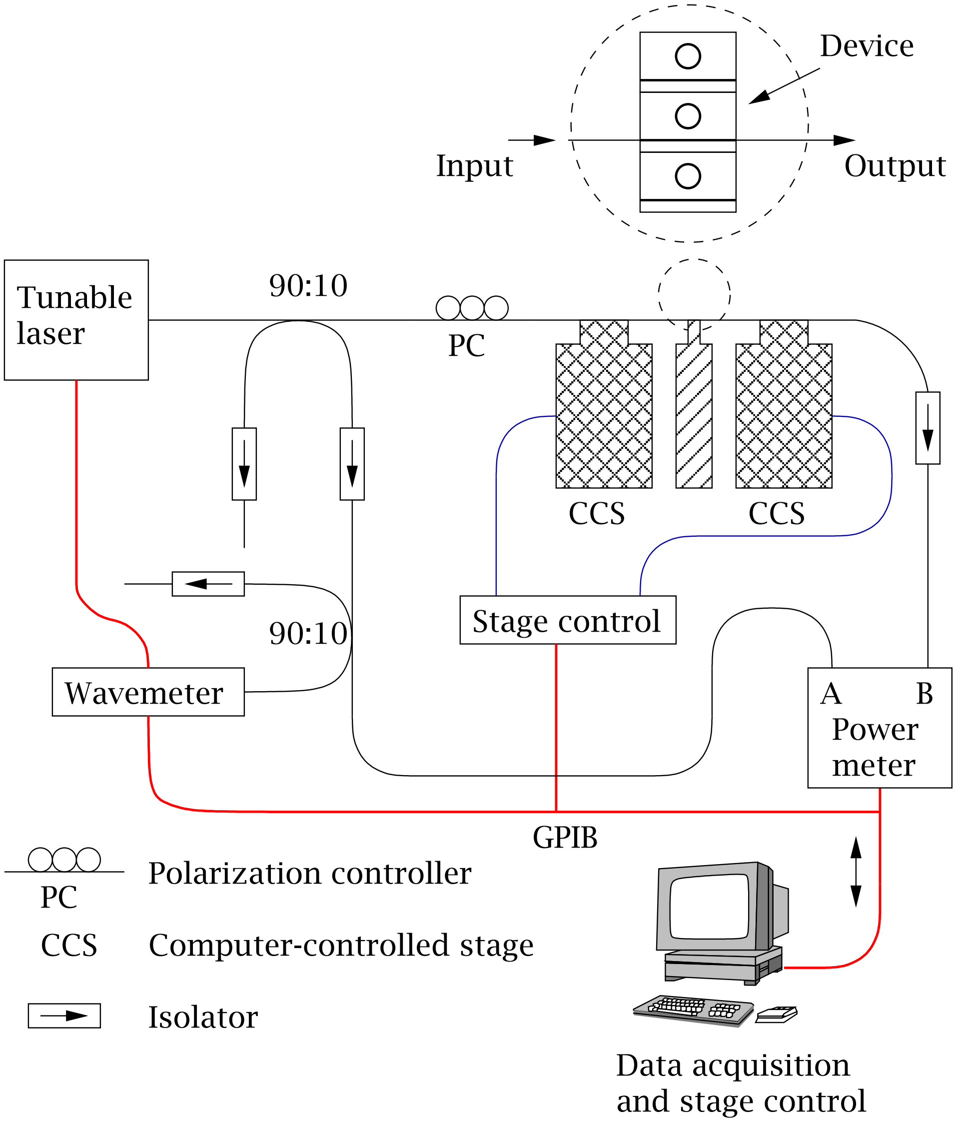

Figure 4.8: Schematic of device test setup (after [172]). The power from the device (channel B of power meter) is normalized to the reference power (channel A) to account for variations in laser output. Power is fed to and collected from the bus with conical fibers to improve the coupling efficiency.

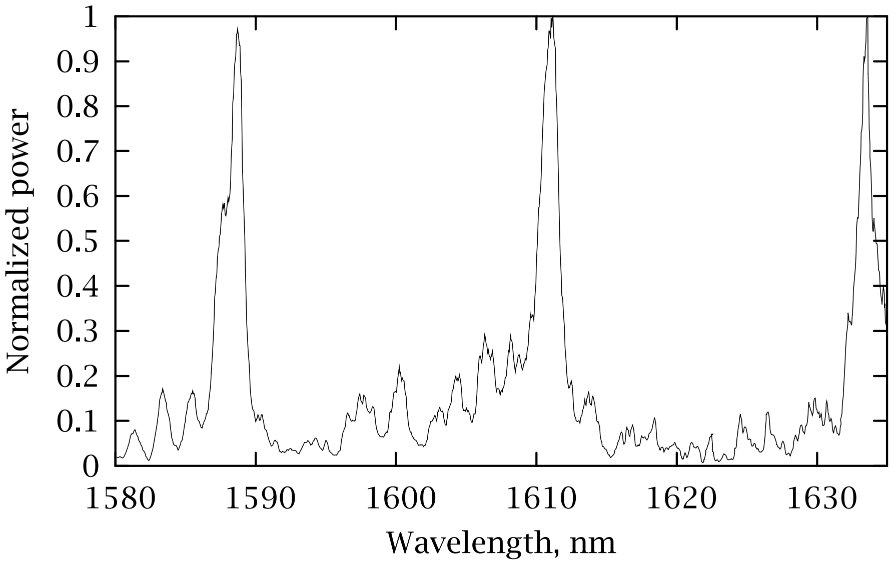

Figure 4.9: Drop port response of a 5 μm radius single ring add-drop filter.

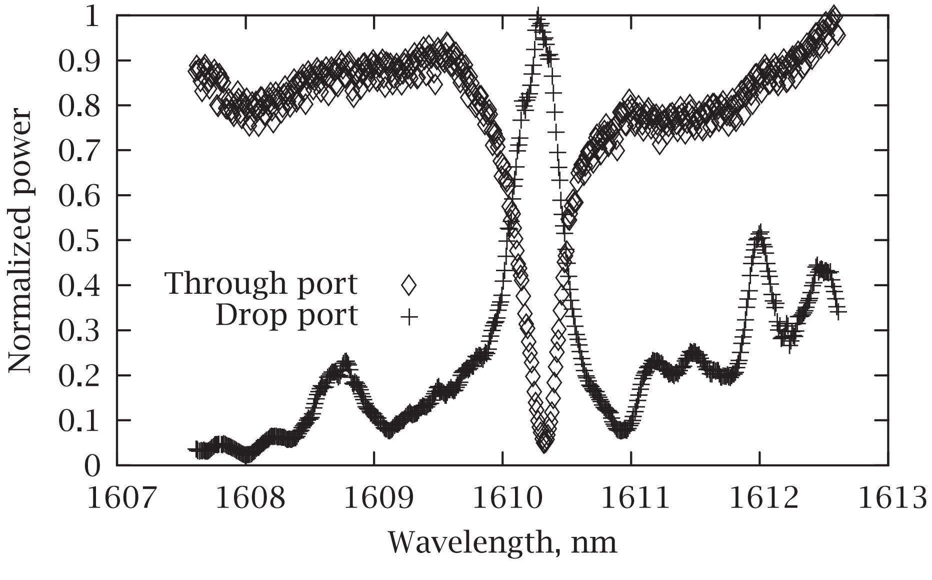

Figure 4.10: Superimposed drop port and through port responses for 10 μm radius ring.

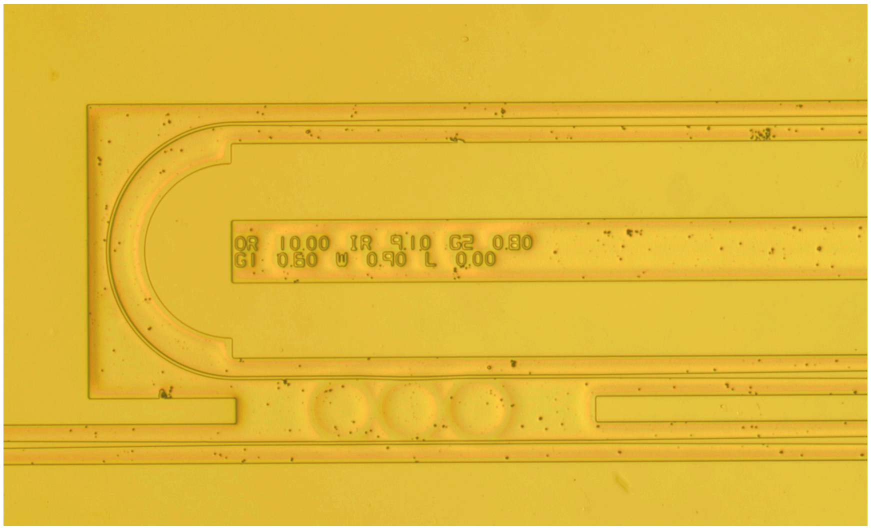

Figure 4.11: Optical micrograph of fabricated GaInAsP-InP triple-micro-ring parallel cascade add/drop filter. The rings are on the lower level.

4.3.2 A parallel cascade of three micro-rings

I fabricated and tested triple micro-ring resonator add/drop filters with the same technique described for a single ring device. These devices were fabricated on a different wafer, which did not have high absorption at 1550 nm, so I was able to test them between 1520 – 1630 nm. Fig. 4.11 shows a triple-ring GaInAsP-InP device. In prior theoretical work Little et al. predicted that periodically coupled multi-ring resonator devices would exhibit sharper roll-off than single ring devices, with a flat-top [112]. Subsequently, our group made these devices in GaAs-AlGaAs, followed by the work described in this section [63]. The theory of parallel cascaded micro-rings is discussed in section 2.10.

The spectral response of the devices is shown in Fig. 4.12. The data is ambiguous as far as the improvement in FSR is concerned, though an argument can be made that it is improved by a factor four to 40 nm compared

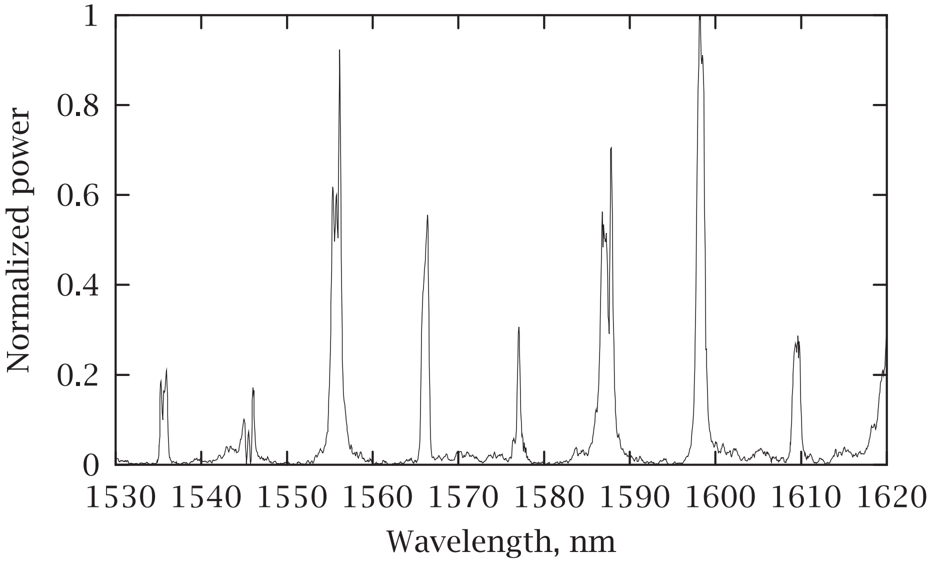

Figure 4.12: Response of periodically coupled triple-micro-ring resonator device with 9.55 μm rings.

to the single-ring case. In Fig. 4.13, we compare the response of a vertically-coupled single- and vertically-coupled parallel-cascaded triple-ring micro-ring resonator channel dropping filter. Note that the response of a three-ring filter has much sharper roll-off and a flat top. Defining roll-off as $\Delta\lambda_{10\ \mathrm{dB}}/\Delta\lambda_{3\ \mathrm{dB}}$, we find the roll-off for a single ring device to be 4.86 and that for a triple ring device to be 1.72, giving an improvement of 2.8 times in the latter case. Thus, these devices show higher-order response. The fast roll-off and flat top may allow this device to be used as an optical bandpass filter.

4.4 Summary

I have demonstrated a new fabrication process for vertically coupled semiconductor micro-ring resonators in the GaInAsP-InP material system. Low-loss

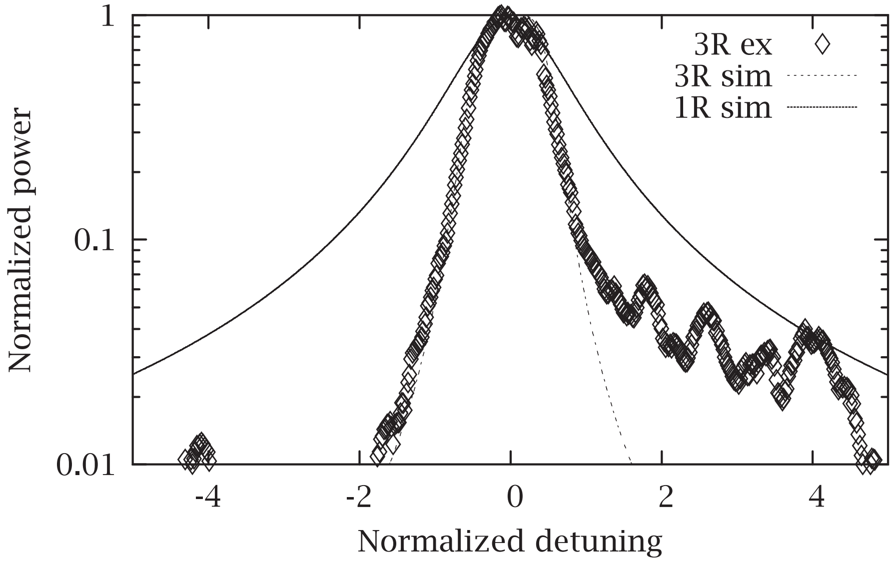

Figure 4.13: Comparison of single (1R sim: simulation) and triple ring (3R ex: experiment, 3R sim: simulation) GaInAsP-InP device response around 1600 nm.

($\sim$ 15 cm^{-1}) tightly confined waveguides are made by a CH_4-H_2-Ar plasma-based reactive ion etching process that provides smooth sidewalls. Substrate transfer permits fabrication of waveguiding structures on both sides of the epilayer and vertical coupling without regrowth. The etched-through alignment keys permit precise layer-to-layer alignment. The middle layer increases alignment tolerance and provides mechanical support for the top BCB cure. The refractive-index profile symmetry of the bonded and encapsulated epilayers permits the use of tight confinement on both guiding layers, making possible the fabrication of identical resonators for high-order filtering on both layers. High-Q ($>$ 3000) micro-ring resonator channel-dropping filters with free spectral ranges of 13 and 24 nm, and resonance bandwidths as low as 0.6 nm, were demonstrated. Subsequently fabricated devices (on a different wafer) had a Q as high as 6500 for 9.55 μm radius rings.

I have also demonstrated high-order roll-off from periodically coupled micro-ring resonators, though the expected wide-FSR response could not be conclusively established. The flat-top response matches theoretical predictions and a possible application could be an optical bandpass filter.

CHAPTER 5

PASSIVE MICRO-RING RESONATORS II: LATERAL COUPLING

In this chapter, I demonstrate laterally-coupled micro-ring resonator devices. At the time of fabrication, these were the smallest optical resonators ever reported in any material system. (Since then, I have demonstrated a smaller resonator, which is described in chapter 7.) The lithography process used is modified from that used in [46] (and related work) for faster write time as the machine used for lithography was off-site (CNF) and the availability of time on the machine was limited.

5.1 Design

The waveguides for this work were designed to be single mode with a layered core due to growth constraints in the MBE (next paragraph). The coupling between the ring and bus waveguides was nominally selected to be 10 %. A simulation of the waveguide mode for the designed dimensions is shown in Fig. 5.1.

The wafer was grown at LPS by S. Kanakaraju and L. C. Calhoun using solid-source molecular beam epitaxy. The layer structure of the device is shown in Fig. 5.2. Since thick layers of GaInAsP are prone to spinodal decomposition, which increases the defect density, the core is composed of alternating layers

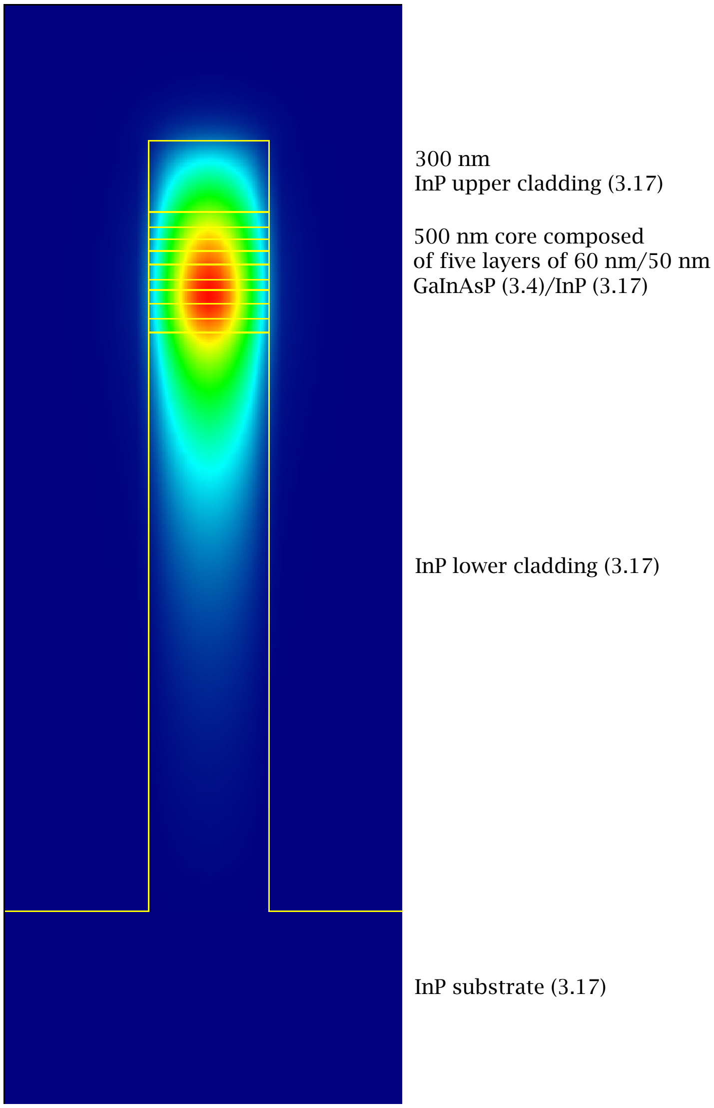

Figure 5.1: Designed waveguide mode and dimensions

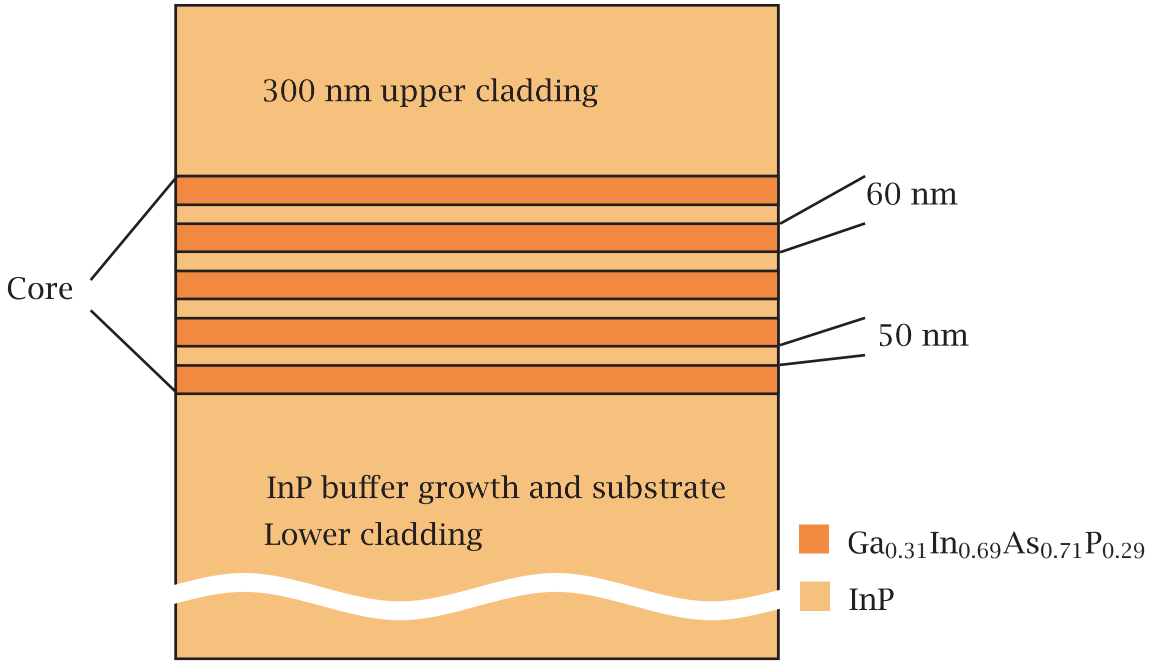

Figure 5.2: Layer structure for laterally-coupled InP microracetrack device. The core is composed of alternating layers of GaInAsP and InP to ease wafer growth requirements.

of GaInAsP and InP. The refractive index of the quaternary layers is 3.39. The substrate was a 3 inch (7.62 cm) diameter Crystacomm InP substrate (InP(100) offcut 2° towards $\langle 111 \rangle$A).

5.2 Process flow

I coated the wafer with 900 nm of silicon dioxide by plasma-enhanced chemical vapor deposition (Fig. 5.3(a), (b)), and used a Leica VB6 e-beam lithography machine to pattern a bilayer film of poly(methyl methacrylate) (PMMA) as follows:

1. Spin on 100K MW 5 % PMMA in Anisole at 4000 RPM for 60 s, which gives a 113 nm-thick film.
2. Bake for 15 min. at 170 °C.
3. Spin on 495K MW PMMA A4 in Anisole at 2000 RPM for 60 s, which gives a 204 nm-thick film.
4. Bake for 15 min. at 170 °C (Fig. 5.3(c)).
5. Write pattern in Leica VB6 HR using a dosage of 736 μC/cm^2 for small features (waveguides and micro-rings), and 610 μC/cm^2 for large features (device labels).
6. Develop with 2-Methyl-2-Pentanone (methyl isobutyl ketone, or MIBK) diluted with 2-Propanol as 1 : 3 for 2 min. 30 s.
7. Rinse with 2-Propanol and blow-dry with nitrogen (Fig. 5.3(d)).

The two layers of PMMA are chosen to have the lower resolution PMMA on the bottom so that when developed, there is an overhang of the higher-resolution PMMA above it where the pattern was written. This helps in liftoff, as the solvent can go into the gap between the metal and the lower portion of the lip, and dissolve both layers of PMMA. Next, I deposited a 50-nm-thick layer of chromium and patterned it by lift-off in warm 1-Methyl-2-Pyrrolidone (Fig. 5.3(e), (f)), and transferred the pattern to the underlying silicon dioxide by dry-etching in a trifluoromethane-oxygen plasma (Fig. 5.3(g)). I etched the InP and quaternary layers by a methane-hydrogen plasma to a depth of 3.2 μm with the Cr-SiO$_2$ mask (Fig. 5.3(h)), and stripped the mask with buffered hydrofluoric acid (Fig. 5.3(i)). Finally, I prepared the device for testing by thinning the chip in bromine-methanol to enable good cleavage, followed by cleaving into bars, and mounting on brass mounts. The process flow is illustrated in Fig. 5.3. Since this work the same process has been successfully used by the group at the Institute of Optics, Rochester, as part of a collaboration to make GaAs-AlGaAs devices with BCl_3-Cl_2-Ar etching [173].

A scanning electron micrograph of a waveguide cross-section is shown in Fig. 5.4, and a fabricated device is shown in Fig. 5.5. The waveguides are fused over a short region (< 1 μm) because of bad liftoff during the mask definition. The radius of the curved sections is 2.25 μm, the straight sections are 10 μm long, the waveguide width is 0.5 μm, and the width of the coupling gap is 0.2 μm. The bus waveguide is tapered to a width of 3 μm away from the coupling region to allow easier coupling of light to and from optical fibers. The waveguides have been etched to a depth of 3.2 μm. The etch depth was chosen to be greater than 2.8 μm to minimize loss from leakage to the substrate. The pedestal design provides a high lateral index contrast, which allows small bends without substantial bending loss [75].

5.3 Device characteristics

5.3.1 Notch filters

I tested the devices without anti-reflection coatings using the test setup shown in Fig. 4.8. I coupled S-polarized light (Fig. 4.7) from the tunable external cavity laser diode to the input port, and collected light at the through port with optical fibers to obtain the spectral behavior. Fig. 5.6 shows the spectra some of the notch filter devices. The baseline of the experimental data has a downward slope due to a drift in the position of the input fiber on the measurement setup, which decreases the power coupled into the device.

Here, I will examine one of the devices in detail. For the device in Fig. 5.6(b),

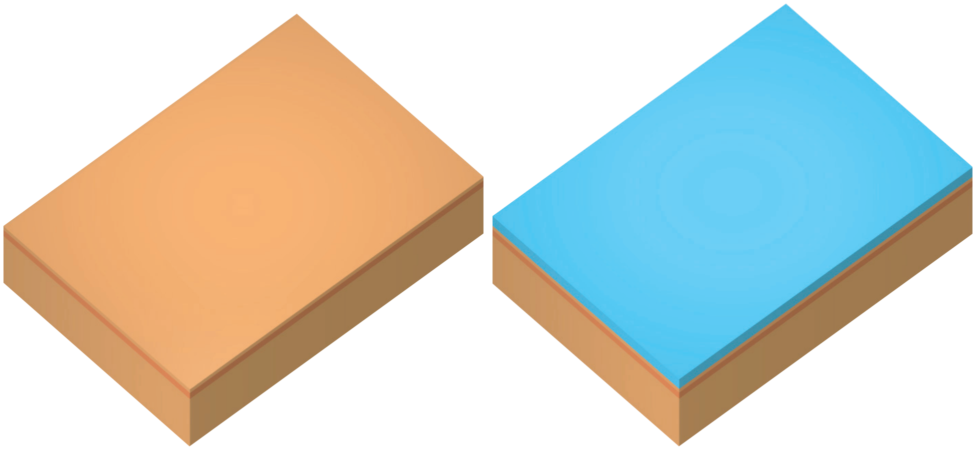

(a) Blank substrate.

(b) Deposit SiO_2 in PECVD.

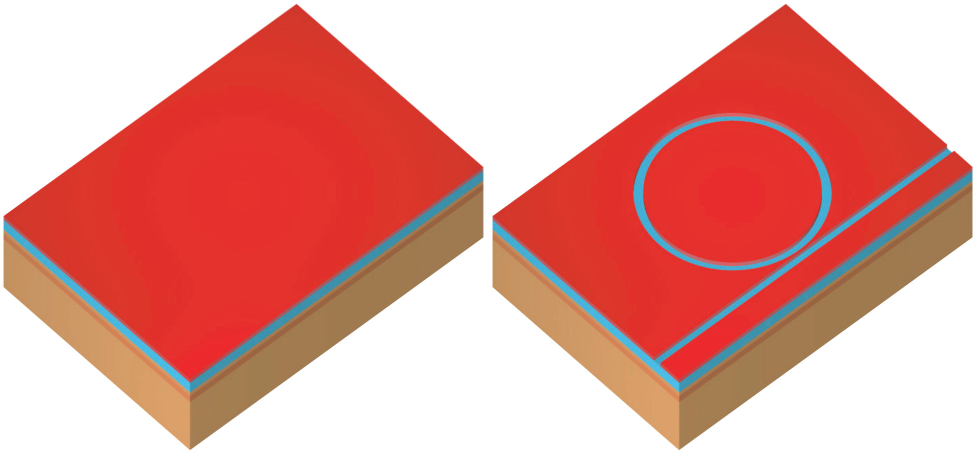

(c) Spin-on a bilayer film of PMMA.

(d) Pattern the bilayer film of PMMA.

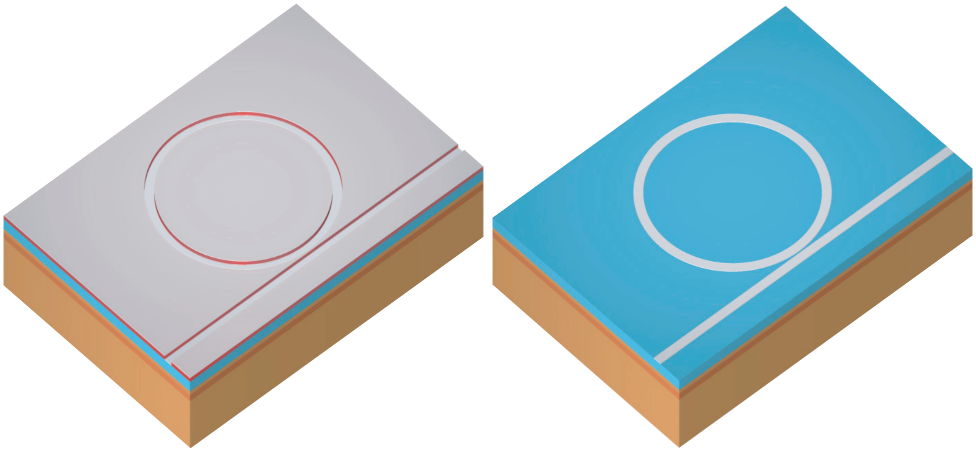

(e) Deposit chromium

(f) Liftoff

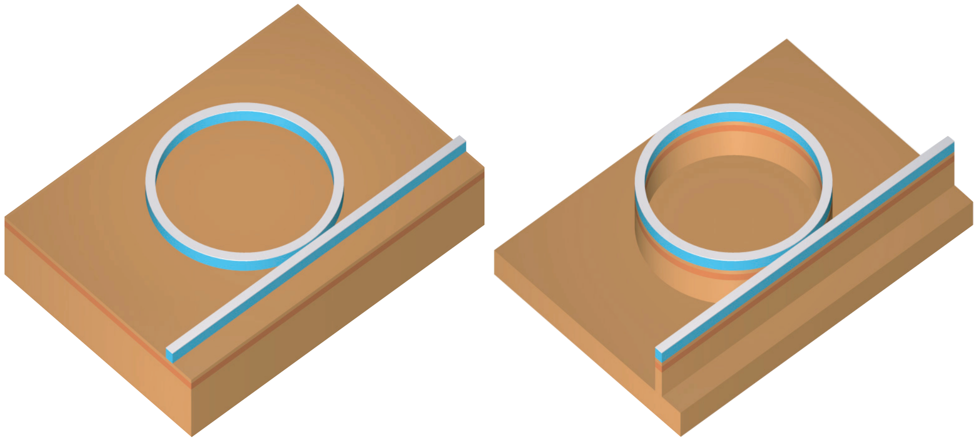

(g) Etch the SiO_2 spacer. (h) Etch the GaInAsP-InP with CH_4-H_2

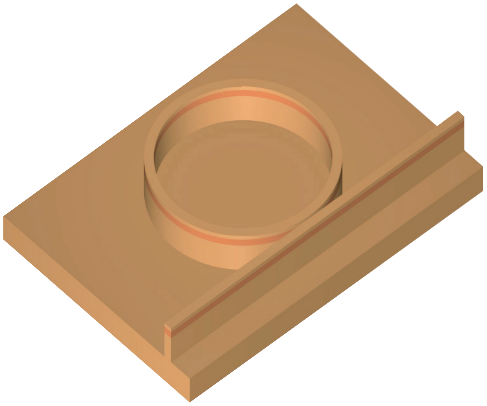

(i) Remove the mask.

Figure 5.3: Laterally-coupled micro-rings process flow.

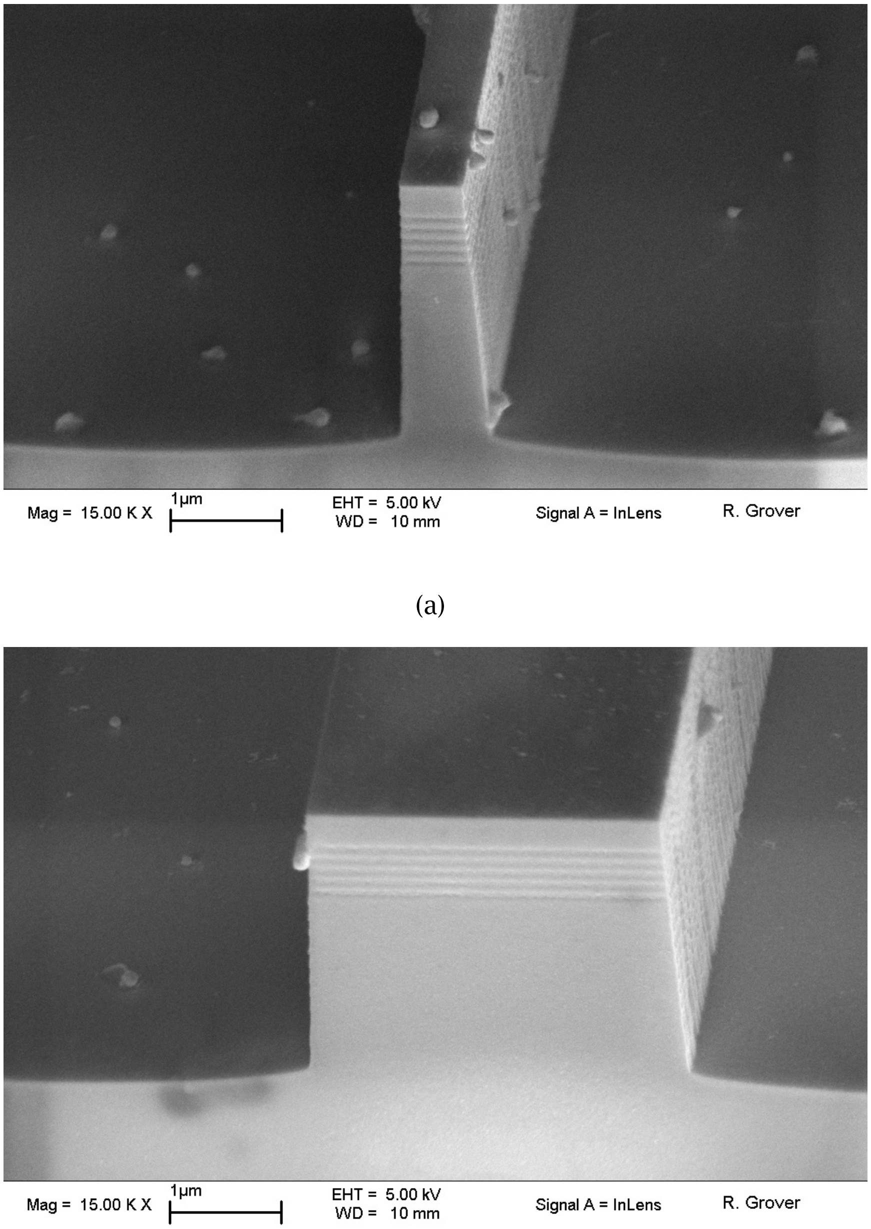

(a)

(b)

Figure 5.4: Scanning electron micrographs of waveguide cross-section. (a) 0.5 μm-wide waveguide in the filter section, (b) 3 μm-side waveguide at the input and output(s). The dark bands are the quaternary layers which comprise the core of the waveguide.

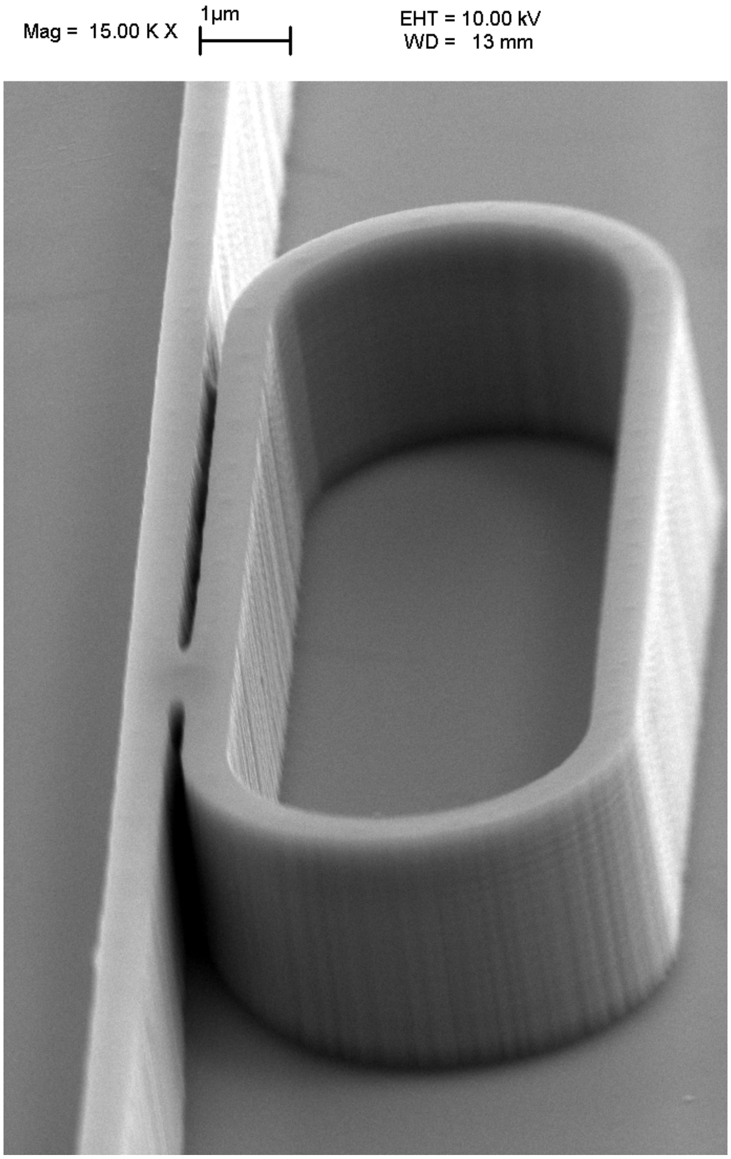

Figure 5.5: Scanning electron micrograph of a laterally coupled micro-ring notch filter.

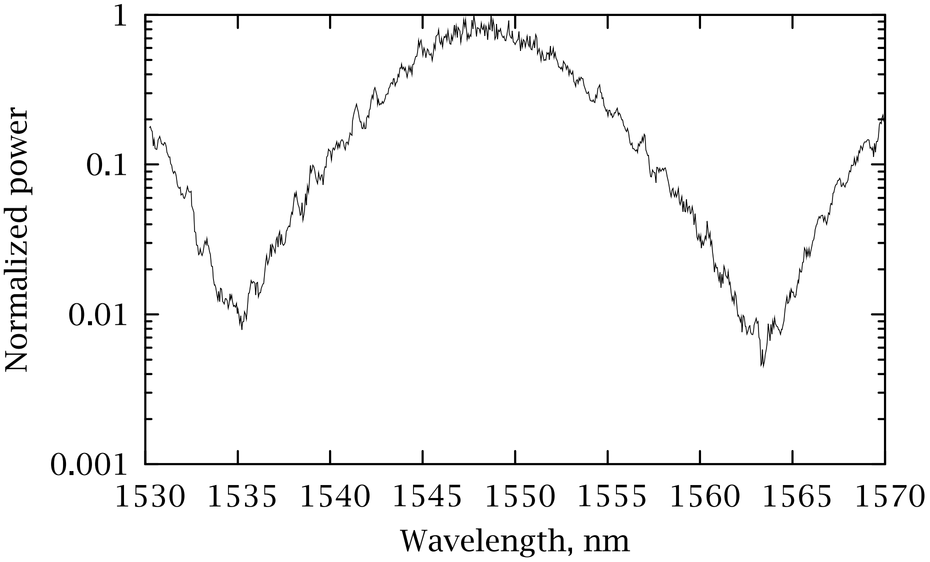

(a) $r = 2.25,\ s = 5, \mathrm{FSR} \approx 28$ nm

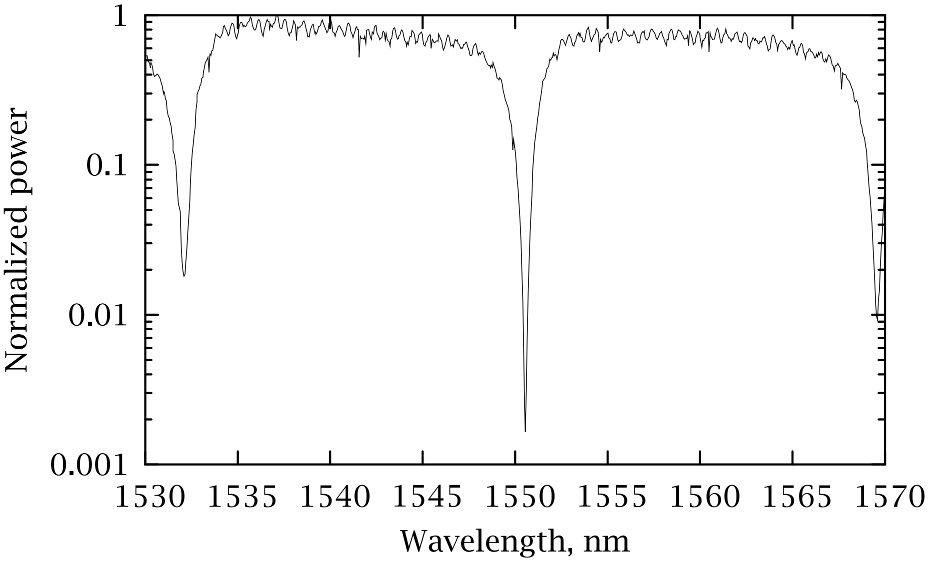

(b) $r = 2.25,\ s = 10, \mathrm{FSR} \approx 19$ nm

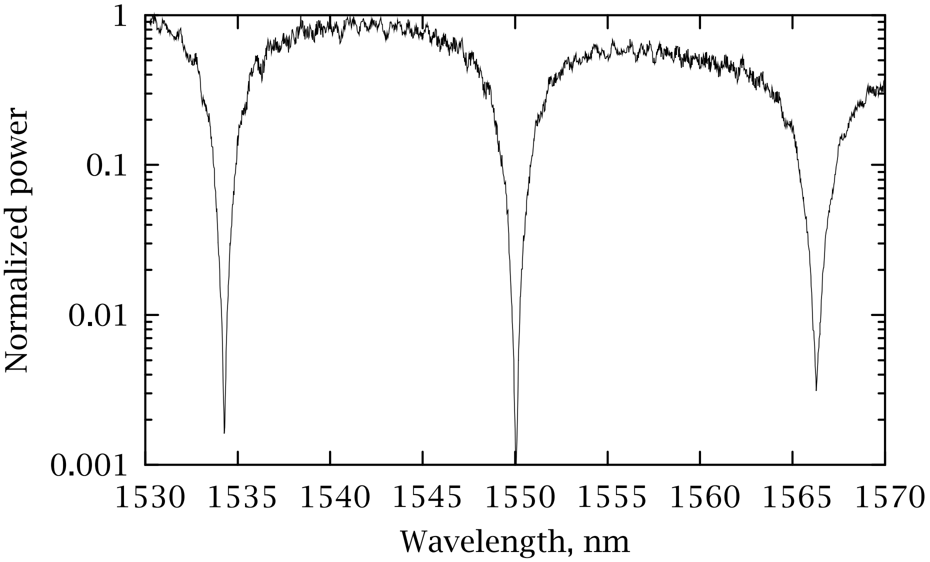

(c) r = 4.75, s = 5, FSR ≈ 16 nm

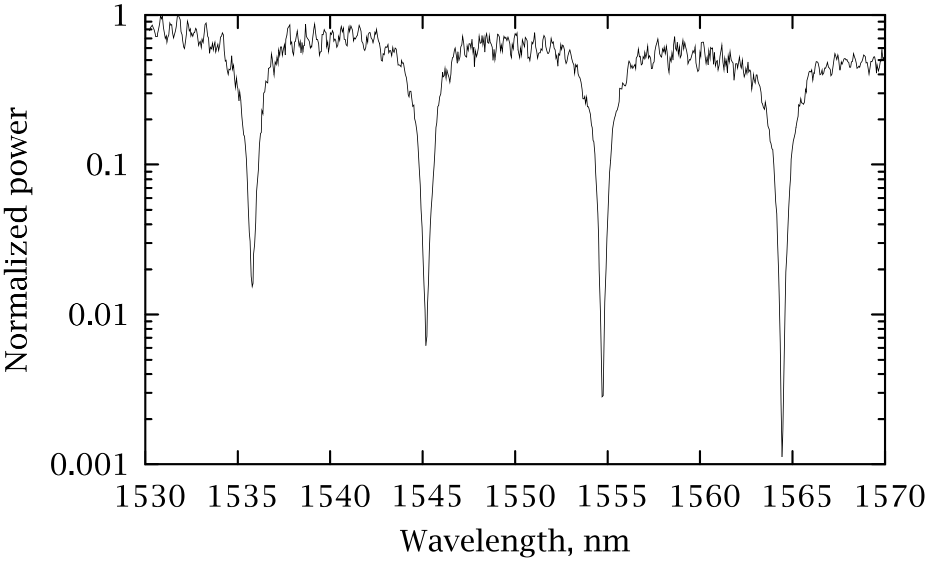

(d) r = 9.75, s = 3, FSR ≈ 9.5 nm

Figure 5.6: Spectral behavior of InP micro-ring notch filters. r is the radius of the curved section, and s is the length of the straight section of the racetrack, both in μm.

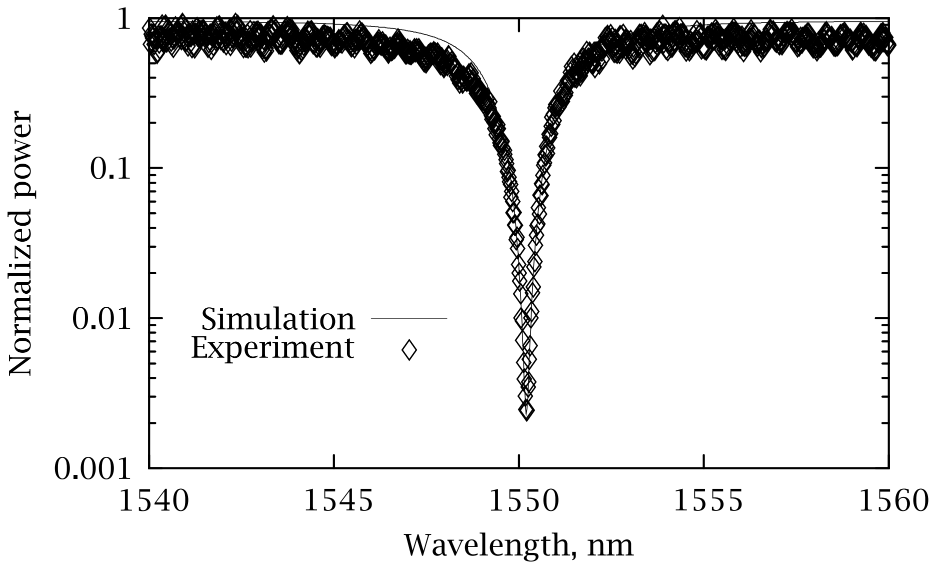

Figure 5.7: Detail of the resonance around 1550 nm.

near 1550 nm, we have critical-coupling: the extinction is > 25 dB, and limited by unpolarized light, which is 26 dB below the S-polarized light near 1550 nm. The free spectral range is 19 nm and increases to 21 nm around 1610 nm. The curve fit in Fig. 5.7 gives the round-trip loss, $1 - \exp(-\alpha L)$, which, at critical coupling, is equal to $(1 - \tau^2)$, as 39.16 ± 1.6 %. Defining the finesse as FSR/$\Delta\lambda$, where $\Delta\lambda$ is the width where the power drops by 3 dB, we find that the finesse of the device is ~ 6 at 1550 nm. The Q is ~ 500. The coupling is consistent with the value of 25 % calculated by coupled-mode theory and numerical simulations of the structure. Near 1550 nm, we have critical coupling. The coupling increases with wavelength, as confirmed by simulations, causing the extinction to decrease on either side of 1550 nm. The FSR changes due to the wavelength dependence of the effective index. Using $n_{\mathrm{eff}} = 2.86$ (from simulations), we get $\mathrm{d}n_{\mathrm{eff}}/\mathrm{d}\lambda = -5.776 \times 10^{-4}/\mathrm{nm}$, and $d^2 n_{\mathrm{eff}}/d\lambda^2 = 3.846 \times 10^{-7}/\mathrm{nm}^2$.

I measured the loss in straight waveguides of comparable width as $\sim$ 17 cm^{-1}, which cannot solely account for the loss in the resonator. However, curved sections typically have slightly higher loss than straight sections because of increased sidewall scattering, and there is loss due to mode-mismatch at the junction between the straight and curved sections. The junction loss usually dominates loss in racetracks with curved sections of small radii [75]. Indeed, comparing the results from Van, et al. [75], we see that their model predicts 1.5 dB loss per round-trip for similar GaAs-AlGaAs devices from sidewall roughness and mode-mismatch at the straight-to-curved junction, while we have 2.2 dB per round-trip, which is a reasonable match. The loss in the resonator can be decreased by incorporating an offset between the straight and curved sections for better mode-matching.

5.3.2 Add/drop filters

In addition to the notch filters demonstrated in the previous section, I fabricated some add/drop filters with Tarek Ibrahim (Fig. 5.8). These devices were designed for use as photonic logic gates, and the through port of some of the devices was on the same side as the input port for use with fiber arrays. Since fiber arrays were not available, we were able to measure only the drop port response for those devices. In other devices, the through port response was buried in the Fabry-Perot resonances of the bus waveguide. The drop port responses of two laterally-coupled add/drop filters are shown in Fig. 5.9. The filter in Fig. 5.9(a) has a curved section radius of 10 μm, and straight sections of length 20 μm (circumference, $L = 101$ μm), resulting in $\Delta\lambda = 0.25$ nm for the resonance near 1563 nm, FSR = 8 nm, $Q \approx 6250$, and $\mathcal{F} \approx 32.4$. The filter in Fig. 5.9(b) has the same dimensions, and $\Delta\lambda = 0.35$ nm for the resonance near 1555 nm, FSR = 7.5 nm, $Q \approx 4440$, and $\mathcal{F} \approx 21.4$.

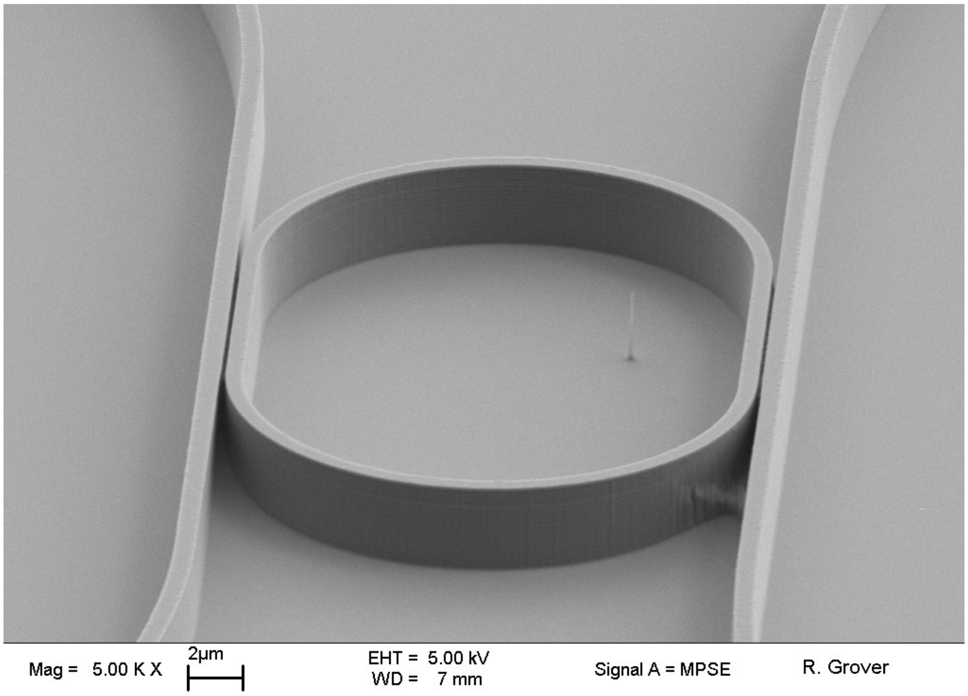

Figure 5.8: Scanning electron micrograph of a laterally-coupled micro-ring add/drop filter.

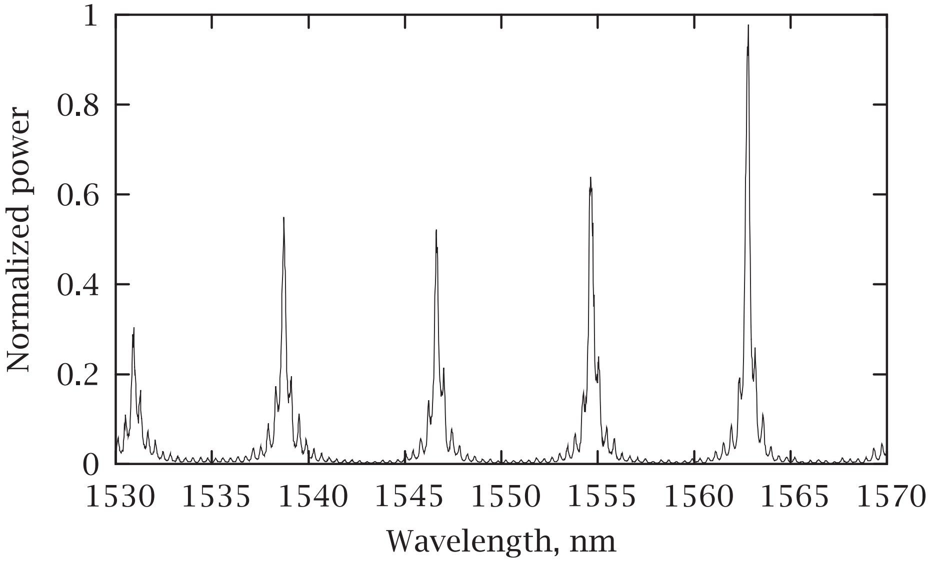

(a)

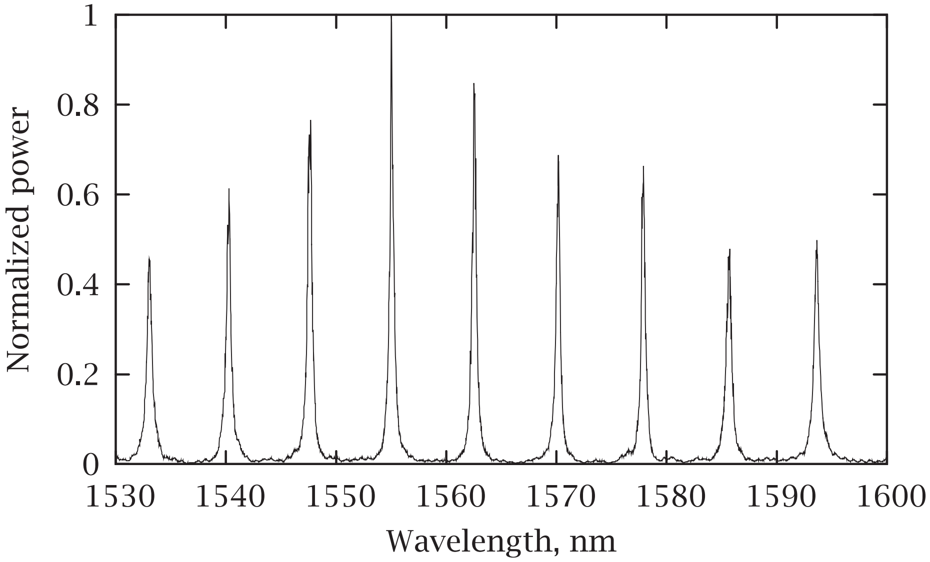

(b)

Figure 5.9: Drop port responses of two laterally-coupled add/drop filters.

5.4 Summary

I have demonstrated single-mode micro-ring resonators with the smallest radius of curvature to date. My devices work as notch filters with extinctions of > 25 dB (limited by the unpolarized light floor), and a free spectral range of as high as 28 nm near 1550 nm. The round-trip loss is high because of the mode-mismatch between the straight and curved sections, but can be decreased by incorporating an offset at the straight-to-curved junction. The high round-trip loss makes the resonances broad, and decrease the Q and finesse. I have also demonstrated add/drop filters with $\Delta\lambda$ as low as 0.25 nm, FSR = 8 nm, Q as high as 6250, and $\mathcal{F}$ as high as 32.4.

The devices are ultra-compact; the entire filter section for my smallest device fits in $5 \times 10\ \mu\text{m}^2$ (an order-of-magnitude reduction compared to the best previous demonstration for this material system), and with better fabrication, the straight section can be eliminated, so that the device would fit in $5\times5\ \mu\text{m}^2$. Therefore, such devices may be useful elements in future optical VLSI circuits.

Note: The electron-beam lithography for this work was performed at the Cornell Nanofabrication Facility (now called the Cornell NanoScale Science and Technology Facility), a member of the National Nanofabrication Users Network, which is supported by the National Science Foundation under Grant ECS-9731293, by its users, by Cornell University, and by Industrial Affiliates.

CHAPTER 6

AN ALL-OPTICAL AND GATE

The work described in this chapter was done in collaboration with Tarek A. Ibrahim. We used the devices described in chapter 5 for this work. Detailed experiments and analyses of nonlinear optics with ring resonators are in [174].

In section 2.5, I showed that the intensity in a micro-ring resonator can be boosted substantially, and in section 2.11, I showed that the refractive index change in a ring resonator due to two-photon absorption scales as $\mathcal{I}^3$. In this chapter, we use the refractive index change from two-photon absorption to demonstrate all-optical logic, specifically, an AND gate with a micro-ring resonator in an all-pass configuration.

6.1 Experiment

The device used (Fig. 6.1) had a round-trip power loss of 40 %, and a coupling coefficient (κ^2) of 46 %, with $\Delta\lambda = 1.8$ nm, FSR = 10 nm, $\mathcal{F} = 6$, and $\mathcal{I} \approx 1.23$. The test setup is shown in Fig. 6.2. We used two counter-propagating data streams to test the device. The RZ data (0.5 GHz, 500 ps pulse duration) was generated by externally modulating the output of a continuous-wave (CW) external-cavity tunable diode laser tuned to 1550 nm using a pattern generator. The data was split with a 50/50 coupler and amplified with two cascaded erbium-doped fiber amplifiers (EDFA), with band-pass filters to reduce noise from amplified spontaneous emission. An optical delay line was used to ad-

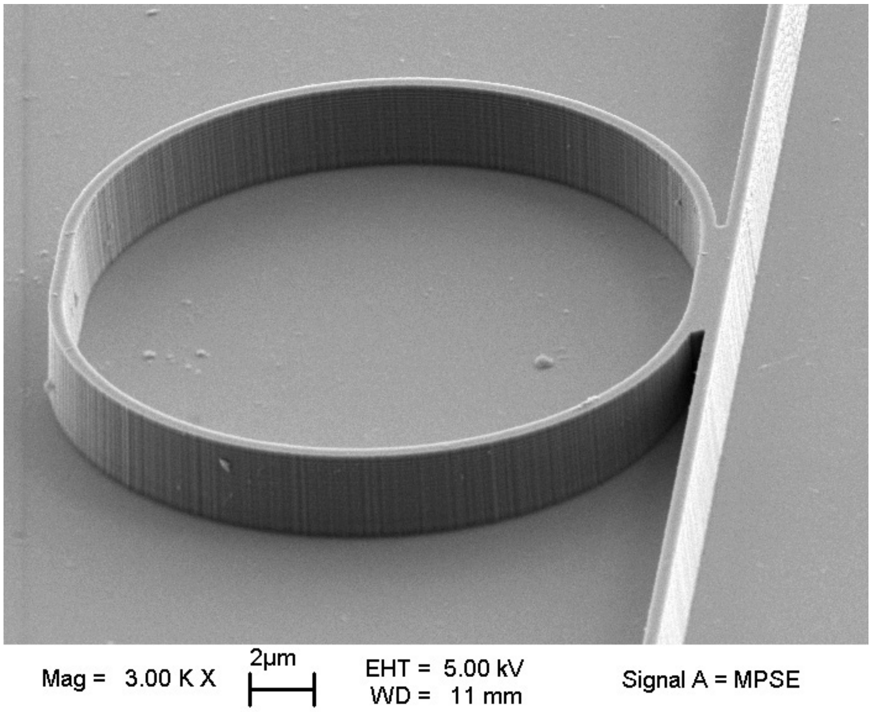

Figure 6.1: Scanning electron micrograph of the micro-ring used as an AND gate. The ring and the bus waveguide are fused due to bad liftoff during mask definition. This has the undesired effect of increasing the coupling to the micro-ring and increasing the loss in the ring, resulting in broad resonances.

just the arrival of one data channel with respect to the other. The probe beam was a CW signal tuned to the resonator resonance at 1560 nm, amplified separately, and coupled with one of the data channels using a 50/50 coupler. The output probe was collected using a fiber circulator, band-pass filtered at the probe beam wavelength, optically-amplified and fed to a 40 GHz detector and 50 GHz oscilloscope.

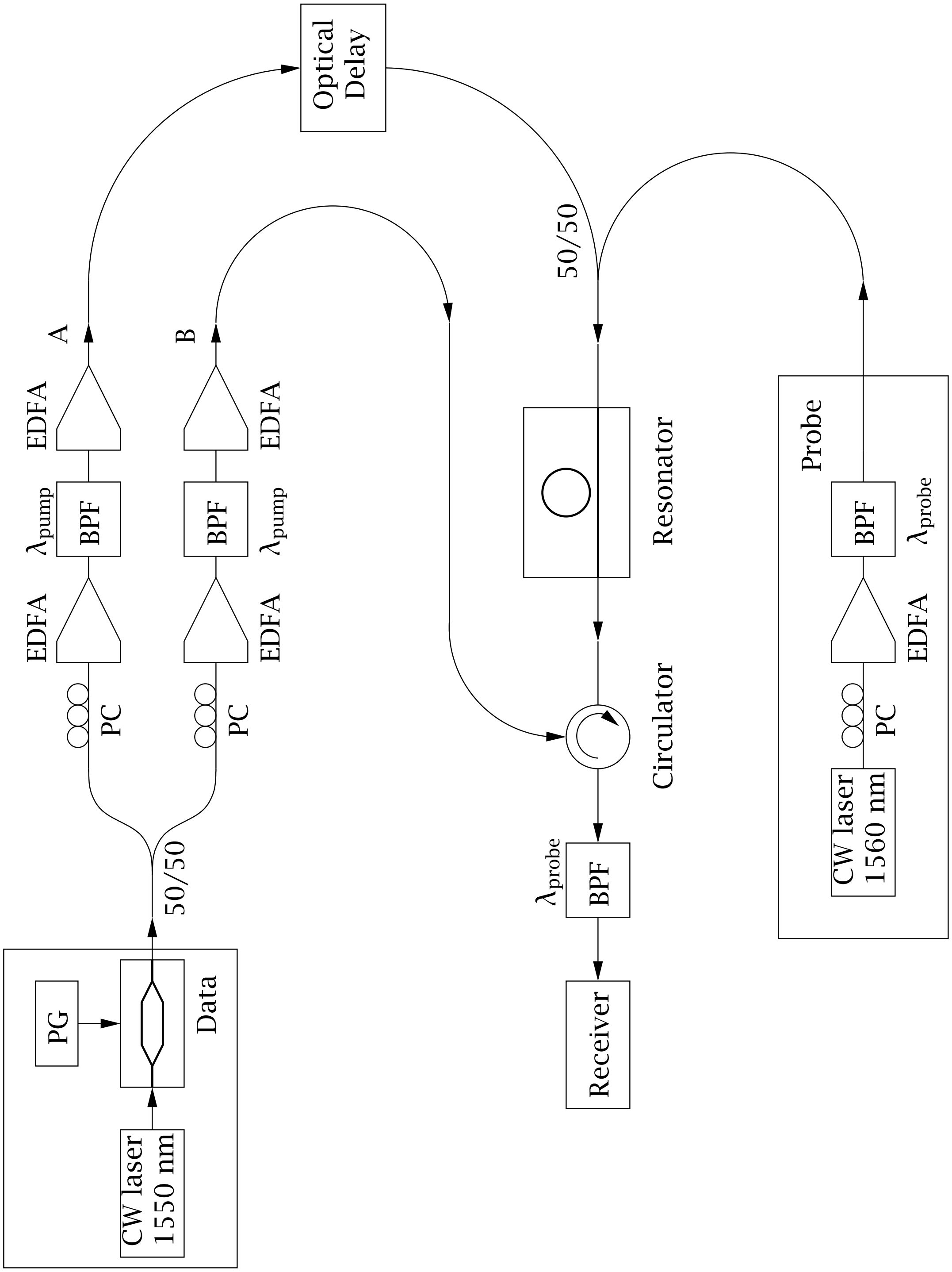

Figure 6.2: Schematic of test setup used for AND gate demonstration.

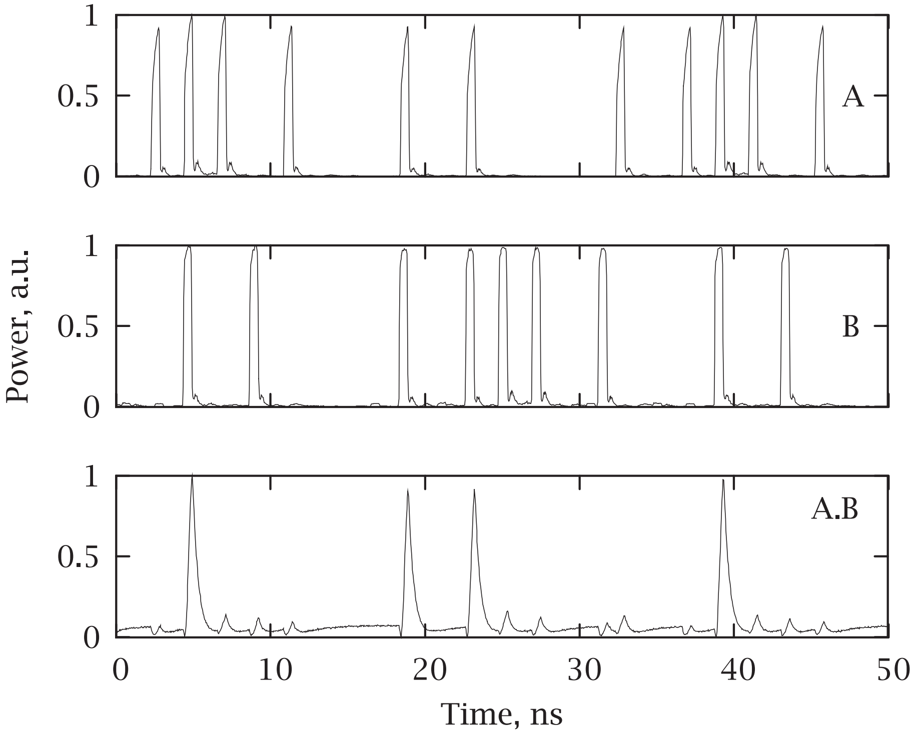

Figure 6.3: AND gate characteristics.

6.2 Device characteristics

The guiding layer was designed to have a bandgap at 1380 nm. The pump pulses are partially absorbed by two photon absorption, and free carriers are generated. The change in refractive index causes switching (Fig. 6.3). Initially, the probe is resonant in the ring, and experiences low transmission, i.e., logic state 0. When either 'A' or 'B' are 1, the change in index is not sufficient to cause switching. However, when both 'A' and 'B' are 1, the amount of carriers generated is much higher due to the quadratic dependence of two photon absorption (section 2.11); if the power of pulses in each stream is equal, four times as many carriers are generated. The resonator then goes off resonance, giving high transmission, or 1.

We investigated the speed of the device by using a single input pump, with pulses of width 35 ps, and duty cycle 5.6 GHz, modulated externally at 140 MHz. The pump pulses had energy of 20 pJ. Considerable power is lost due to the splitters, input coupling, and at the tapered sections of the bus waveguide, so the power coupled into the resonator is much lower. We lose 3 dB at each splitter, and $>$ 6 dB at the input facet; the power lost in the taper has not been measured. As an upper bound, we estimate the pulse energy coupled into the filter section of the bus waveguide to be a few pJ. We measured the switching window as 100 ps, limited by the carrier lifetime, and a 13 dB switching contrast, limited by the noise floor of the receiver. From the measured data and simulation model, we estimate a 0.9 nm temporal tuning of the micro-ring resonator for the pulse energy coupled into the ring (few pJ). The two photon absorption coefficient, α_2 for InP was separately measured and found to be 43 cm/GW.

In general, for carrier-generation-related effects, the the switching speed is limited by the photon lifetime and the carrier lifetime. The photon lifetime, τ_{photon}, is related to the number of round-trips made by light in the ring before the power is depleted to (say) $1/e$ of its initial value. For a resonator with $\mathcal{F} = 100, L = 60\ \mu\text{m}, n_{\text{eff}} = 3$, this value is $\tau_{\text{photon}} = \mathcal{F} L n_{\text{eff}}/(2\pi c) = 4.8$ ps. If the waveguide material is designed to have short carrier lifetimes, this represents the limiting case for switching speed. However, for the device described in this chapter, the waveguide core is intrinsic and bulk, so the switching speed is determined by ambipolar diffusion to the waveguide walls, which is dominated by slow carrier (hole) diffusion [115], which is 150 cm^2/Vs. This accounts for the relatively slow switching speed of 100 ps.

We measured the carrier mobility by pumping a straight waveguide section and probing the change in induced absorption at a different wavelength. The absorption tail gives us the carrier lifetime as 120 ps. Since the carrier lifetime is dominated by surface recombination, the carrier lifetime is the time taken to reach the sidewalls, which allows us to calculate the mobility. We estimate the (ambipolar) mobility of our sample as 210 cm^2/Vs. The ambipolar mobility from literature is 290 cm^2/Vs [115], which is comparable to our measured value. The switching speed can be improved by applying a reverse bias to sweep out the generated carriers, by doping the waveguide with p-dopants, or by appropriately straining the core lattice to lift the LH band and increase the hole mobility. If the waveguide were engineered so that the carrier lifetime is determined by the electron mobility (4600 cm^2/Vs), the device speed would be limited by the photon lifetime, allowing operation at many tens of GHz or more.

6.3 Summary

We have demonstrated an all-optical AND gate with an InP-based micro-ring resonator. Pump pulses alter the refractive index of the resonator by generating free carriers via two photon absorption. The switching speed is limited by ambipolar diffusion, and can be improved by applying a bias and doping the core, among other means.

Note: The electron-beam lithography for this work was performed at the Cornell Nanofabrication Facility (now called the Cornell NanoScale Science and Technology Facility), a member of the National Nanofabrication Users Network, which is supported by the National Science Foundation under Grant ECS-9731293, by its users, by Cornell University, and by Industrial Affiliates.

CHAPTER 7

A TUNABLE MICRO-RING NOTCH FILTER

In this chapter, I demonstrate the tuning of a laterally-coupled micro-ring resonator notch filter. In addition to being tunable, this device is the smallest optical micro-ring resonator ever reported in any material system.

7.1 Design

Tuning can be achieved with the electro-optic, electro-refractive (carrier-induced), or thermo-optic effect. Thermal effects are typically slow – modulation speeds are typically tens of kHz at best and they depend on the heat conductivity of the material and the temperature of the surrounding medium or the heat sink. The electro-refractive effect can afford high modulation speeds in a properly designed material/device. It uses carrier-based refractive index change, and is limited by the carrier lifetime, which we saw in the previous chapter. In general, the electro-optic effect has the best potential for low-loss high-speed refractive-index-modulation as it does not involve carriers. However, it requires careful design of the material to prevent excessive loss when modulating the refractive index.

I chose to demonstrate tuning using the electro-optic effect. InP-based electro-optic phase and amplitude modulators using QCSE have been demonstrated earlier; the layer structure used here is based on that in Fetterman et al., 1996 [128]. The core of the waveguide is composed of a superlattice of quantum-wells to take advantage of the QCSE. For low-loss operation, I designed the material so that the signal wavelength was $>$ 60 meV from the band edge. The wafer was grown at LPS by S. Kanakaraju and L. C. Calhoun using solid-source molecular beam epitaxy. The wafer was a 3 inch (7.62 cm) diameter Crystacomm InP substrate (InP(100) offcut 2° towards $\langle 111 \rangle$A). The layer structure of the device is shown in Fig. 7.1. The core is designed to have a bandgap of 1.44 μm, so that there is little or no absorption in the C-band. For good material growth, where the leakage currents would be low, the use of a reverse-biased p-i-n structure would mean that most of the bias voltage appears across the core, which is 0.5 μm-thick in our case.

7.2 Process flow

I fabricated the device as in chapter 5, except that I etched to a depth of 4.5 μm (Fig. 7.2(a)-(i)). Since the device needed planarization for deposition of contacts, I coated it with a thin layer of SiO_2 ($\sim$ 70 nm) to help with the adhesion of the benzocyclobutene planarization layer. Prior to spin-coating the benzocyclobutene, I spun-on an adhesion promoter, AP3000 from Dow Chemical, at 2000 RPM for 30 s. The benzocyclobutene used was Cyclotene 3022-46 from Dow Chemical, spun-on at 4000 RPM for 60 s (Fig. 7.2(j)). This was followed by etchback of benzocyclobutene and SiO_2 to expose the tops of the waveguides (Fig. 7.2(k)). For the top (p-side) contact, I deposited Ti-Pt-Au. The chip was thinned by M. Lisa Lucas with an abrasive (alumina) to enable good cleavage, then I deposited the bottom (n-side) contact of Pd-Sn-Au-Pd-Au. Although the n-contact usually requires annealing [175], I was unable to anneal it because the BCB cannot tolerate the high temperature ($\sim$ 400°C) required. Finally, I cleaved the chip into bars, and mounted them on oxygen-free

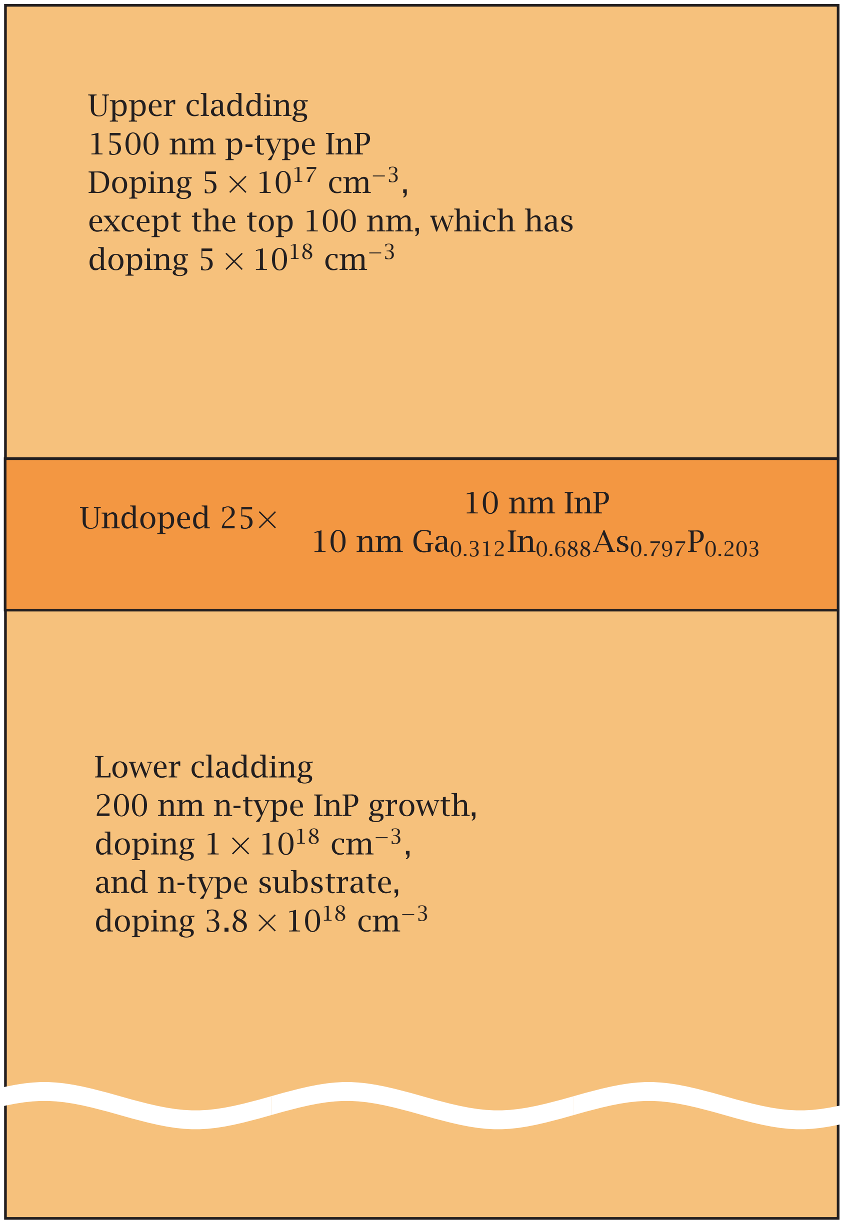

Figure 7.1: Layer structure for laterally-coupled electro-optically-tuned GaInAsP-InP micro-ring device. The upper cladding is very thick to minimize optical loss from the top contact.

copper mounts with a silver epoxy. In the device described here, I deposited the top-side electrode globally (on both the bus and the resonator). This led to unwanted electro-absorption in the bus waveguide due to the QCSE when a reverse bias was applied, so for improved performance, the bus and ring should be electrically isolated. The complete process flow for a device in which the bus and ring are electrically isolated is illustrated in Fig. 7.2.

A scanning electron micrograph of a fabricated device prior to planarization is shown in Fig. 7.3. The ring is in the shape of a racetrack. The waveguides are fused over the short coupling region (1 μm) because of bad liftoff during the mask definition. The radius of the curved sections is 2.25 μm, the straight sections are 1 μm long, the waveguide width is 0.5 μm. The designed width of the coupling gap was 0.1 μm; here, since the bus and ring are fused, the coupling region has a width of 1.1 μm. The bus waveguide is tapered to a width of 3 μm away from the coupling region to allow easier coupling of light to and from optical fibers. The waveguides have been etched to a depth of $\sim$ 4.5 μm. The tall, grass-like structures on either side of the waveguide are probably due to contaminants in the reaction chamber. The grass is not very close to the sidewalls, possibly because both the Cr-SiO_2-mask and the particles which caused micro-masking may have had the same sign of charge.

Fig. 7.4 shows the cross-section of the input/output waveguide of a fabricated device with the BCB planarization and Ti-Pt-Au top contact. As can be seen in the picture, the planarization layer began to detach from the waveguide sidewall in this particular device. This is a serious problem and can severely limit the yield, as it can create a short circuit around the diode. However, it can be addressed by using planarization materials which have better adhesion (say, polyimides), or by increasing the thickness of the SiO_2 deposited to improve the adhesion of the benzocyclobutene. If the SiO_2 layer

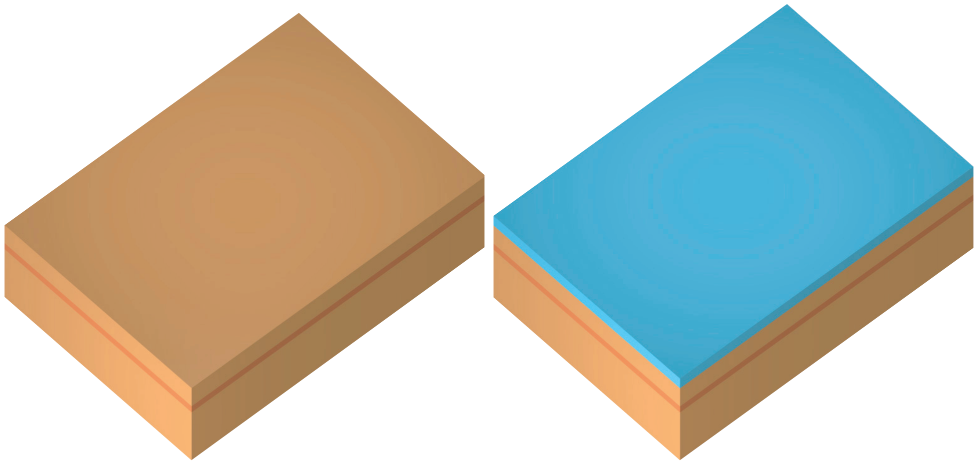

(a) Blank substrate

(b) Deposit SiO_2 in PECVD.

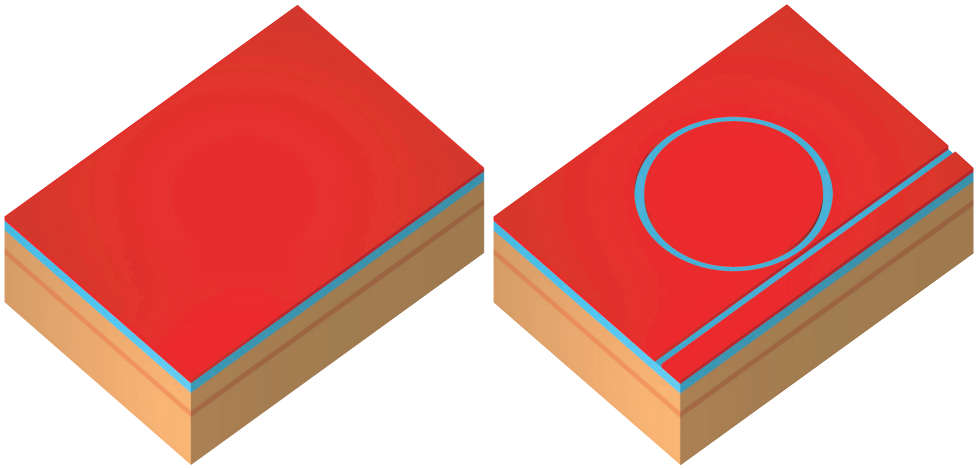

(c) Spin-on a bilayer film of PMMA.

(d) Pattern the bilayer film of PMMA.

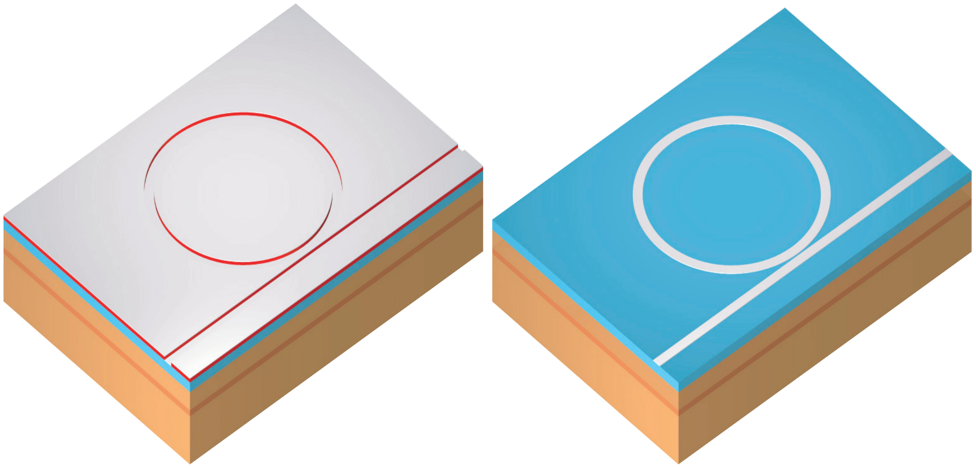

(e) Deposit chromium.

(f) Liftoff.

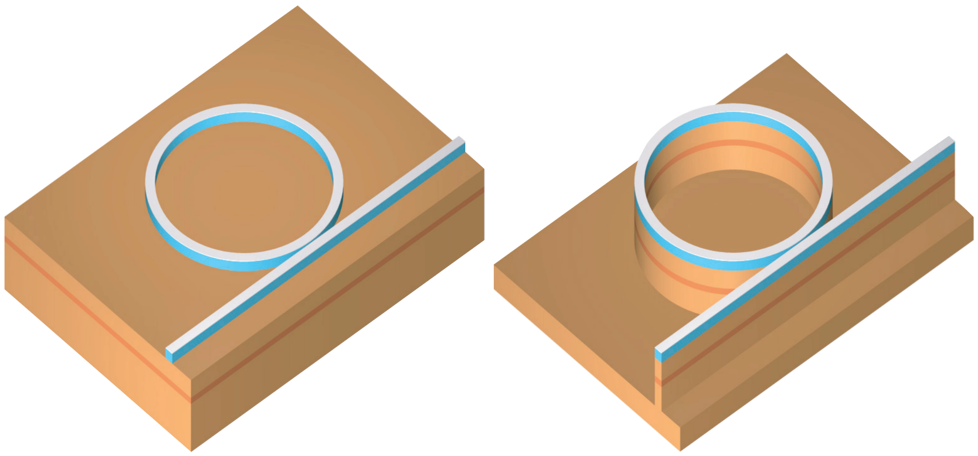

(g) Etch the silicon dioxide spacer. (h) Etch the GaInAsP-InP with CH_4-H_2.

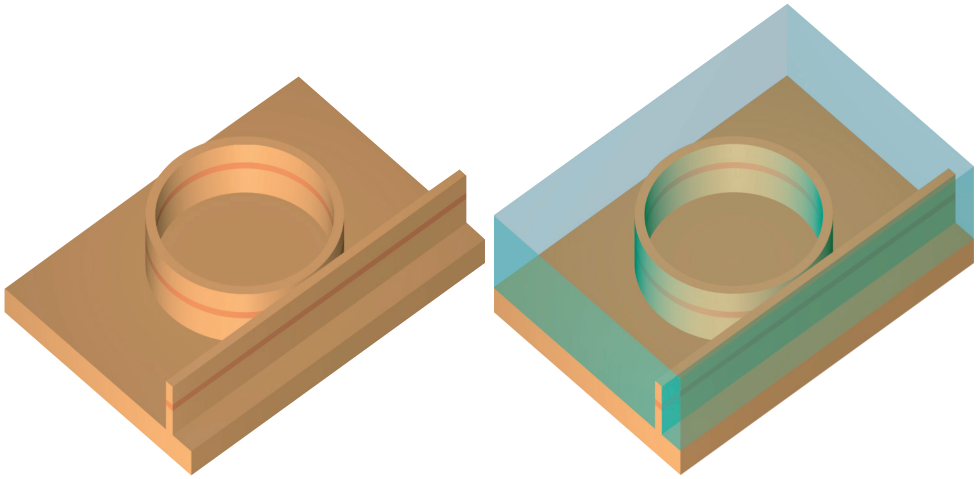

(i) Remove the mask. (j) Planarize.

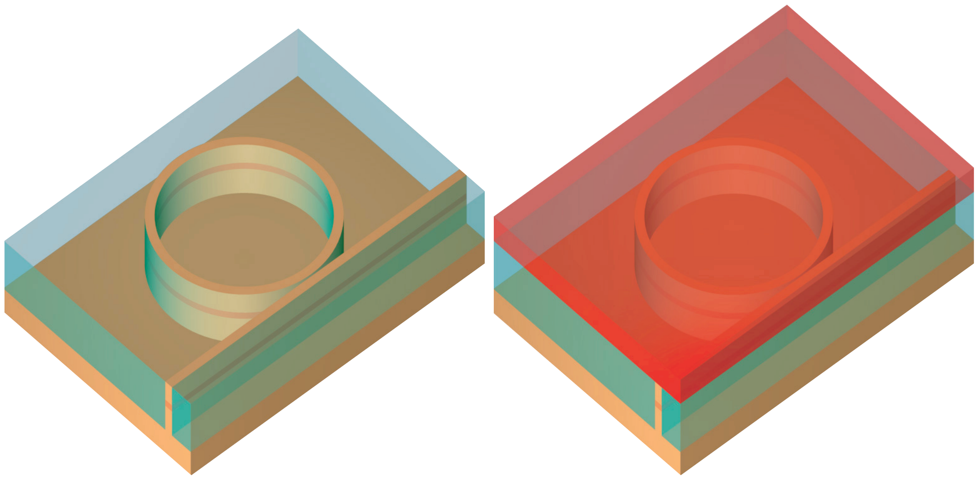

(k) Etchback. (l) Spin-on photoresist.

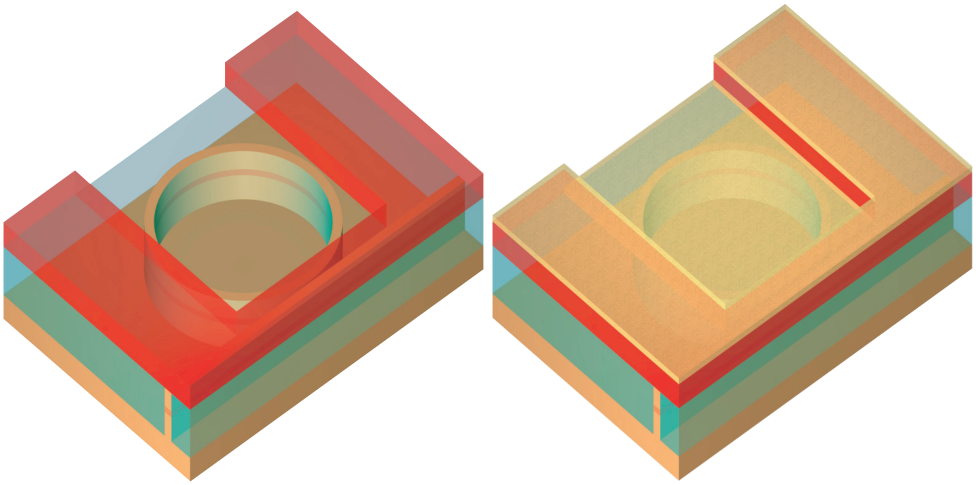

(m) Pattern photoresist.

(n) Deposit p-side contact.

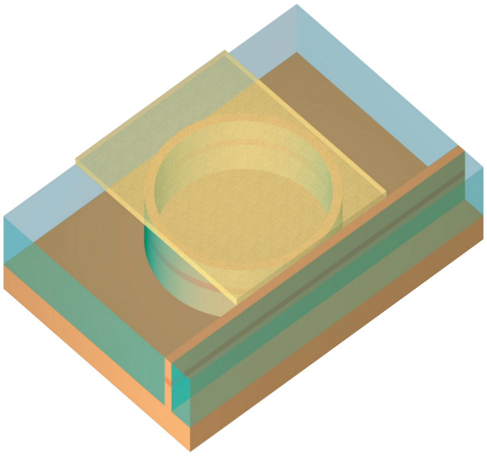

(o) Liftoff.

Figure 7.2: Active micro-rings process flow. The last step shown is followed by thinning, deposition of n-side contact, scribing, cleaving, and mounting. For the devices described in this chapter, I did not pattern the top-contact, i.e., I deposited the p-contact globally, so the bus and ring were not electrically isolated. This led to unwanted absorption in the bus when a bias was applied.

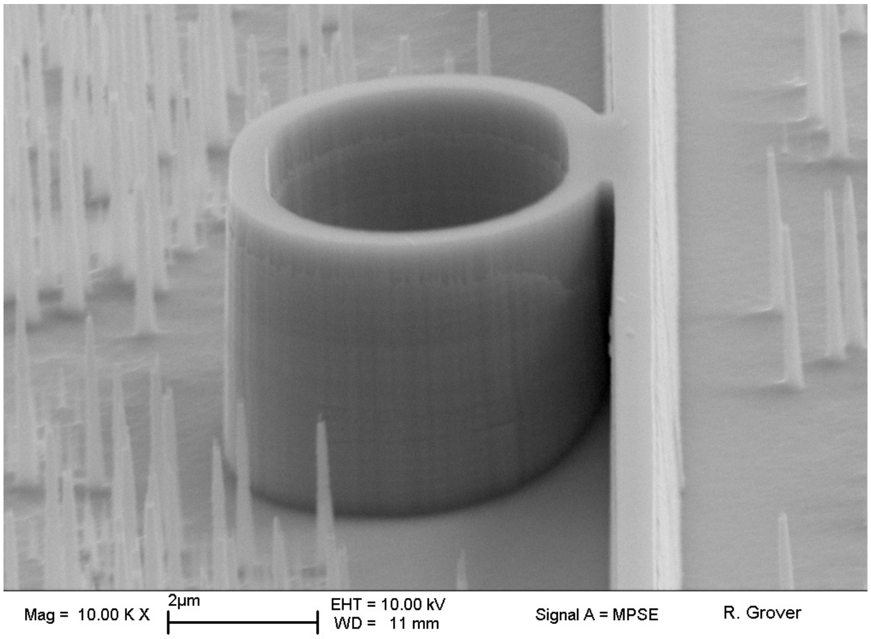

Figure 7.3: Scanning electron micrograph of fabricated device prior to planarization and metallization.

were thick enough, it would prevent the diode from being short-circuited.

7.3 Device characteristics

7.3.1 Material characteristics

To confirm that the wafer behaved as a diode, I tested the electrical characteristics of the wafer by putting contacts on either side of the wafer, and using a semiconductor parameter analyzer (Agilent 4155B). The characteristics are shown in Fig. 7.5 and validate the electrical design, but introduce a wrinkle in the form of a high reverse leakage current, which may mean that thermal effects play a role in devices employing reverse bias.

To find the electro-optic coefficient of the material, I constructed a free-

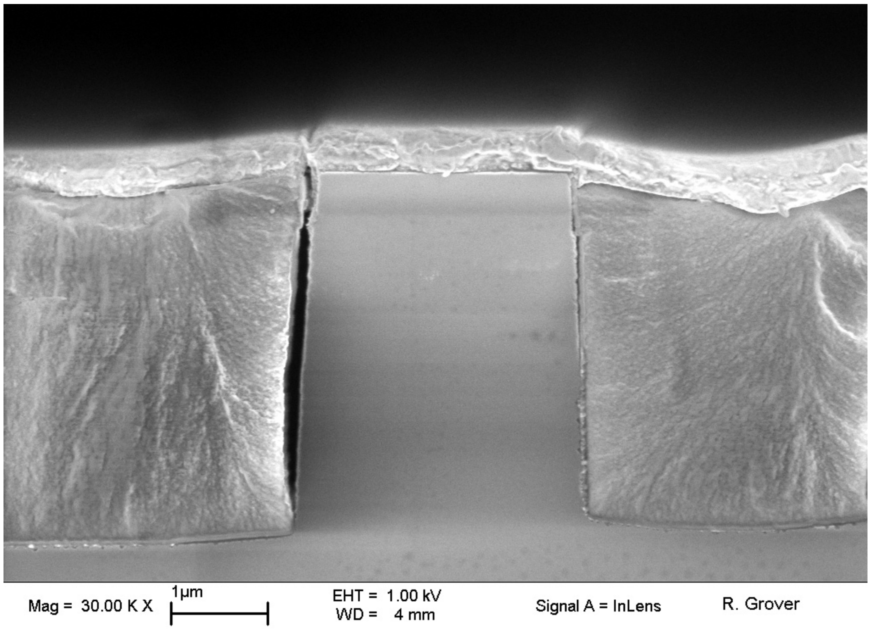

Figure 7.4: Cross-section of input-output waveguide in fabricated device. The ridge in the center is the waveguide, the material on either side is the BCB planarization layer, and the contact is on the top.

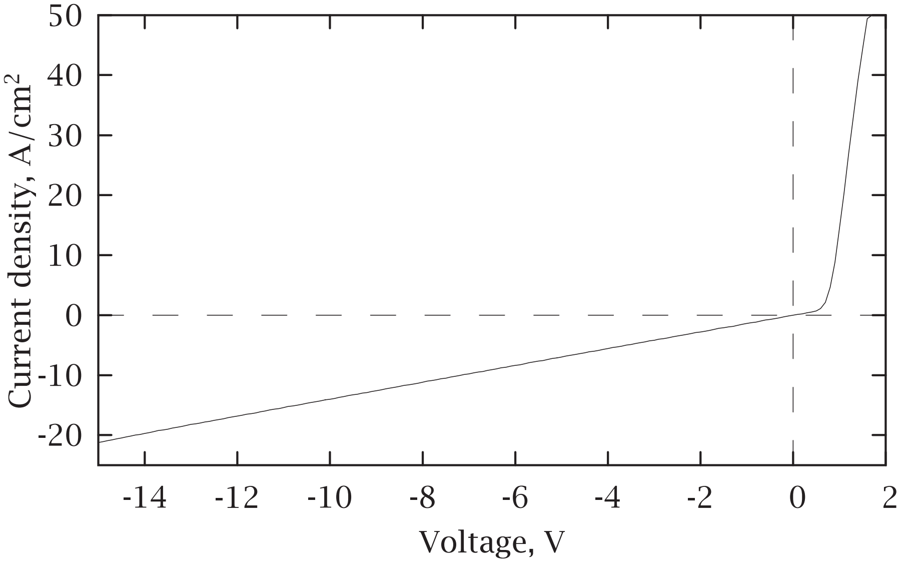

Figure 7.5: Electrical characteristics of diode made with wafer used for electro-optically tuned ring resonators. The diode area is 100 × 2000 μm^2.

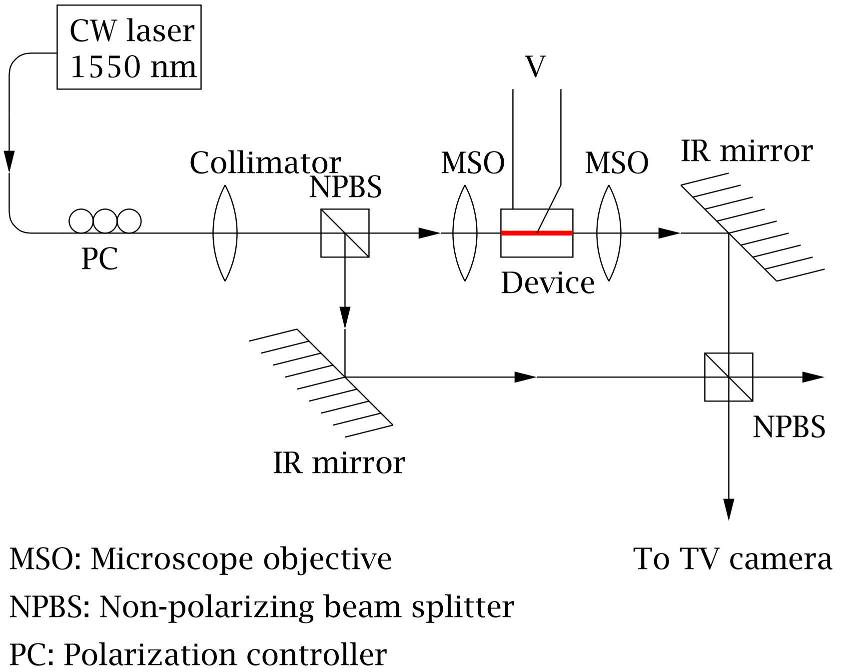

Figure 7.6: Mach-Zehnder interferometer for EO coefficient measurement.

space Mach-Zehnder interferometer (Fig. 7.6) and looked at the interference pattern versus voltage (Fig. 7.7) for a slab waveguide made from the material. Composite images of the interference pattern v/s voltage for the S (out-of-wafer-plane) and P (in-wafer-plane) polarizations are shown.

As can be seen, the interference pattern shifts with voltage for both polarizations. For the S-polarization, at 5 V, the phase change is 2π because the maxima and minima coincide with those at 0 V. If we assume that the effect is purely quadratic in nature (which is the case for the quadratic EO effect in InP for the S-polarization), we have

$$\begin{aligned} \Delta n &= \frac{1}{2} n^3 s E^2, \text{ and} && (7.1) \\ 2\pi &= \Delta n \frac{2\pi L}{\lambda} && (7.2) \end{aligned}$$

Using $\lambda = 1.55\ \mu$m, $L = 0.2$ cm, $E = 10$ V/μm (5 V), and $n = 3.22$ (effective

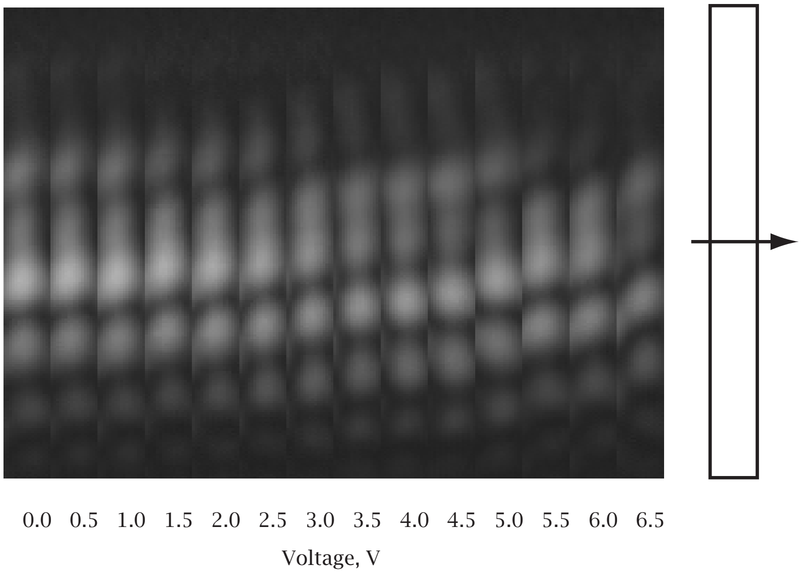

(a) S-polarization (out-of-wafer-plane).

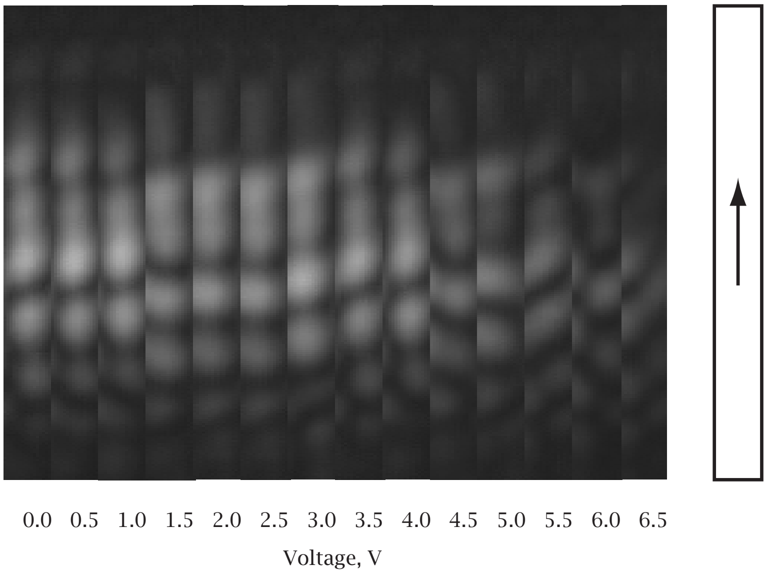

(b) P-polarization (in-wafer-plane).

Figure 7.7: Interference pattern versus voltage. The empty rectangular box represents the orientation of the slab, and the arrow indicates the *E*-field polarization.

index of slab) gives

$$s = 2.3 \times 10^{-15}\ \mathrm{cm}^2/\mathrm{V}^2. \tag{7.3}$$

At this stage, it is tempting to identify s with the quadratic electro-optic coefficient, but the high reverse leakage current means that the effect may well be thermal – the $I - V$ curve for the material is approximately linear below 0 V to around 6 V, so both the thermal and EO effect are quadratic with voltage for the S-polarization. To distinguish between the thermal and electro-optic effects, we require high-speed (pulsed) testing. If the absorption changes at high-speeds, it implies that the QCSE is changing absorption, hence is at least partly responsible for the index change. Since the EO coefficient was measured under DC conditions, the modulation depth should match low frequency measurements.

First, I measured the impedance of the device upto 2 MHz by placing it in series with a 10 Ω resistor as shown in Fig. 7.8(a). The resistor had an inductance of 4 μH (as measured by an inductance meter), so is depicted as two elements, L_2, and R_2. The device is represented as a resistor, R_1, in parallel with a capacitance, C. The capacitance is calculated from the dimensions of the slab (100 μm×2 mm plate, separated by 0.5 μm, $n^2 = 3.3$). R_1 is calculated from the voltage drop across the resistor at low frequencies. The measured data and the theoretical prediction is shown in Fig. 7.8(b). Since the predicted curve provides a reasonable fit, we can conclude that the device impedance does not change appreciably to around 2 MHz.

Next, I modulated the waveguide with sinusoidal signals from 1 Hz to 2 MHz. I measured the response below 2 MHz with a 2 V peak-to-peak signal offset below 0 by 1 V, a large-area photodetector (ThorLabs PDA400) and a lock-in amplifier (Perkin-Elmer 7081 DSP Lock-in amplifier); the frequency re-

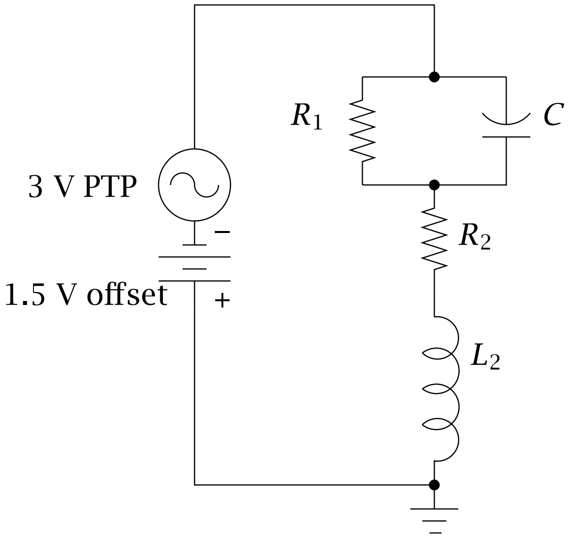

(a)

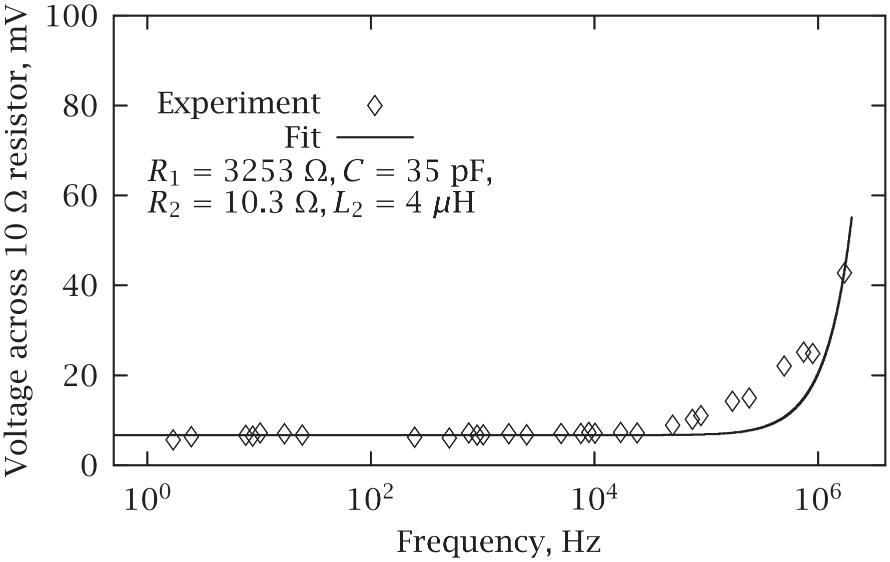

(b)

Figure 7.8: (a) Setup for impedance measurement of slab waveguide, and (b) voltage across R_2 and L_2 versus frequency.

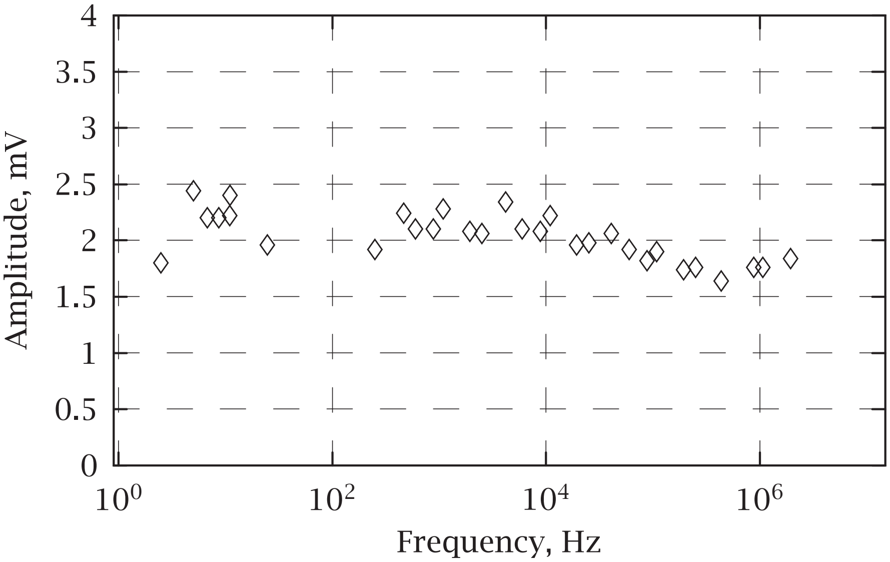

Figure 7.9: Frequency response of slab waveguide.

sponse is shown in Fig. 7.9. We can estimate the thermal roll-off frequency for the slab structure to be 14 kHz or less by solving the heat diffusion equation.

Since the frequency response is flat to 2 MHz, which is considerably higher than the maximum predicted thermal roll-off frequency of 14 kHz, it is a reasonable demonstration that the absorption modulation not thermal in nature. So we can conclude that the absorption modulation is from the quantum-confined Stark effect, and the index change seen in the waveguide is due to the electro-optic effect. Further, since there is a large leakage current, the electro-optic coefficient measured (s) represents a lower-bound for the quadratic electro-optic coefficient of the waveguide.

7.3.2 Tuning measurements

For the tuning measurements, the device was tested without anti-reflection coatings. I used amplified spontaneous emission (ASE) from two cascaded erbium-doped fiber amplifiers (EDFA) to obtain the spectrum of the device at various voltages. A schematic of the test setup is shown in Fig. 7.10.

7.3.3 Raw data and normalization

I have normalized the spectrum to account for the input EDFA spectrum, and increased absorption with bias in the bus waveguide due to QCSE or increased temperature. The latter effect can be mitigated by patterning the contact so that it is only on the ring, and by using a waveguide core with larger bandgap. The data prior to normalization for two voltages is shown in Fig. 7.11. To normalize the data to the EDFA spectrum, I measured the EDFA power over the wavelength range, calculated the power at each wavelength with a polynomial fit, and divided the measured output power from the device by the EDFA power at each measurement wavelength (Fig. 7.12). Finally, to account for the changing loss in the bus, I normalized the power to the maximum power over the wavelength range at each voltage.

7.3.4 Normalized data

The device spectrum at two voltages is shown in Fig. 7.13. Although the input has a mixed polarization, the device has very high loss for the in-plane polarization, effectively filtering the in-plane polarization. So the response shown in Fig. 7.13 is for the out-of-plane polarization. The free spectral range of the device is $>$ 30 nm, so other peaks lie outside the EDFA band. Therefore, I have shown only one dip. Due to the fused bus and ring, the resonator has a high loss, which increases the bandwidth to a few nm; as a result, the Q of the resonator is quite low, about a few hundred. The resonance wavelength of the resonator is red-shifted with reverse bias. For clarity, I have overlaid

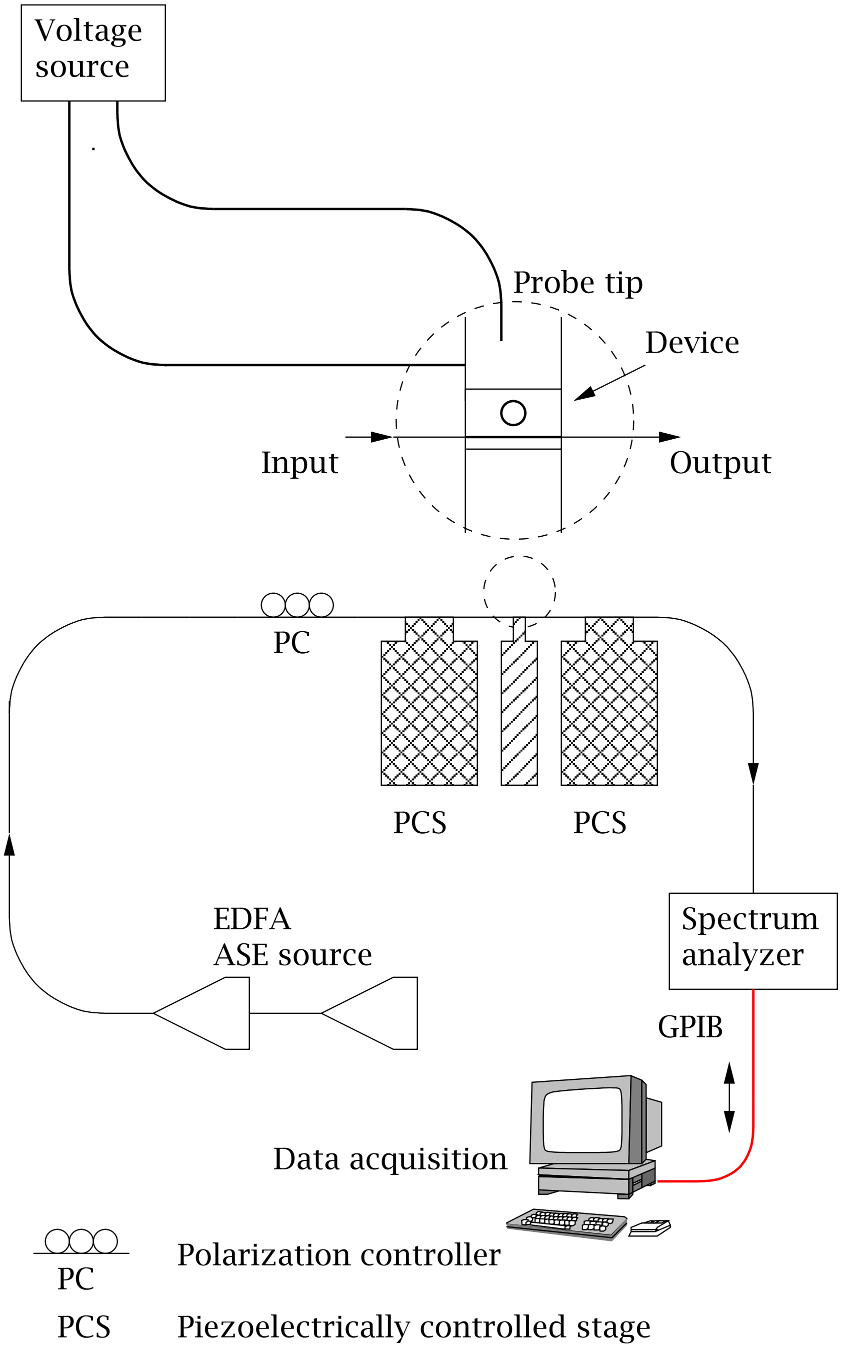

Figure 7.10: Schematic of active device test setup.

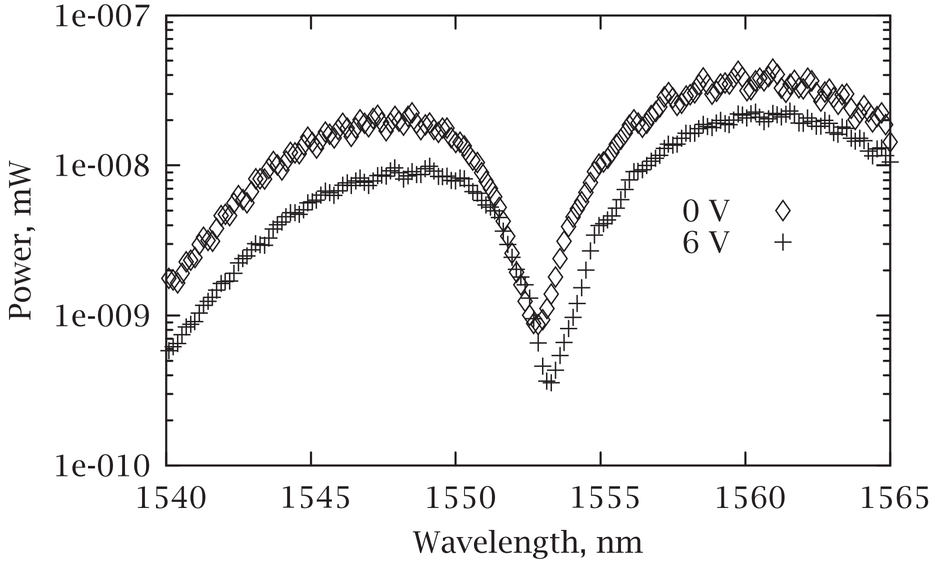

Figure 7.11: Raw data for active resonator at two voltages.

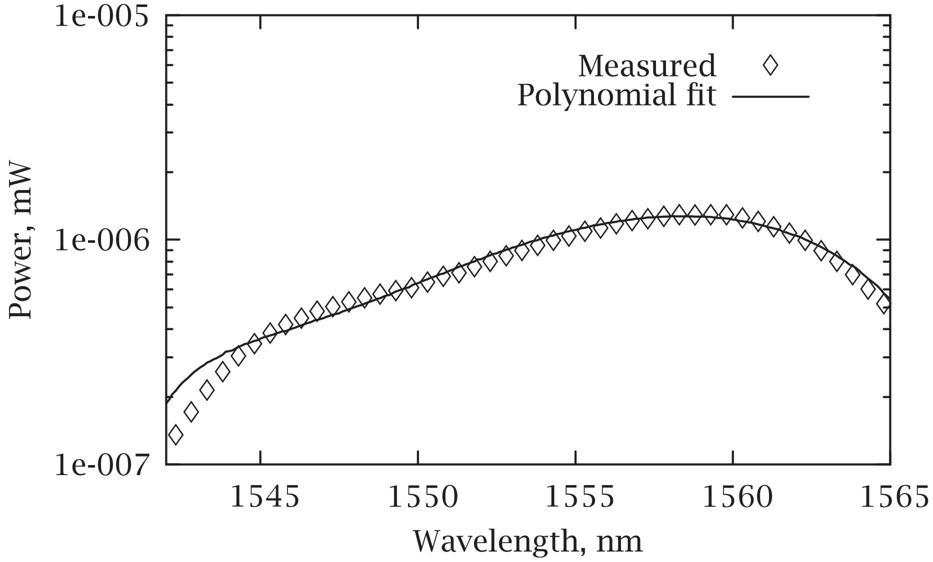

Figure 7.12: EDFA spectrum and polynomial fit used to normalize the raw spectral data for the active resonator.

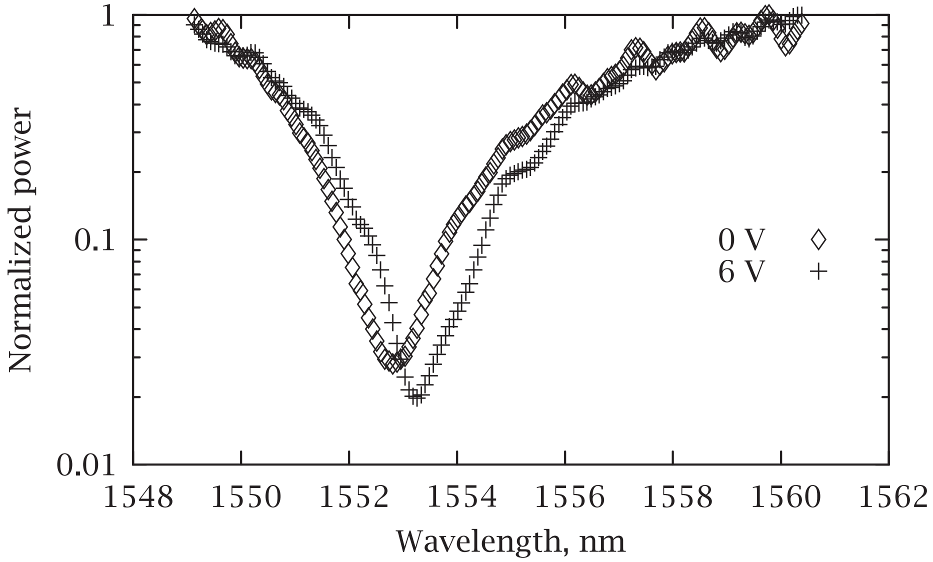

Figure 7.13: Change in resonance wavelength with voltage.

the spectrum for only two voltages. The normalization process is discussed in the previous sub-section.

Fig. 7.14 shows the change in effective refractive index with voltage. The resonance locations were determined by a minimum search routine written in MATLAB which fitted a polynomial to each resonance shape to overcome noise, and then searched for the local minimum of the polynomial. The resonance locations are stepped because of the resolution of the optical spectrum analyzer (0.08 nm) used to collect the spectra. The corresponding value of the resonance wavelength is shown on the right side. The refractive index in the absence of a reverse bias is obtained from simulations using a commercial waveguide mode solver (Optical Waveguide Mode Solver from Apollo Photonics).

Using eq. 2.103 and a quadratic fit to the data in Fig. 7.14, we can get the quadratic electro-optic coefficient for the waveguide. The value of the

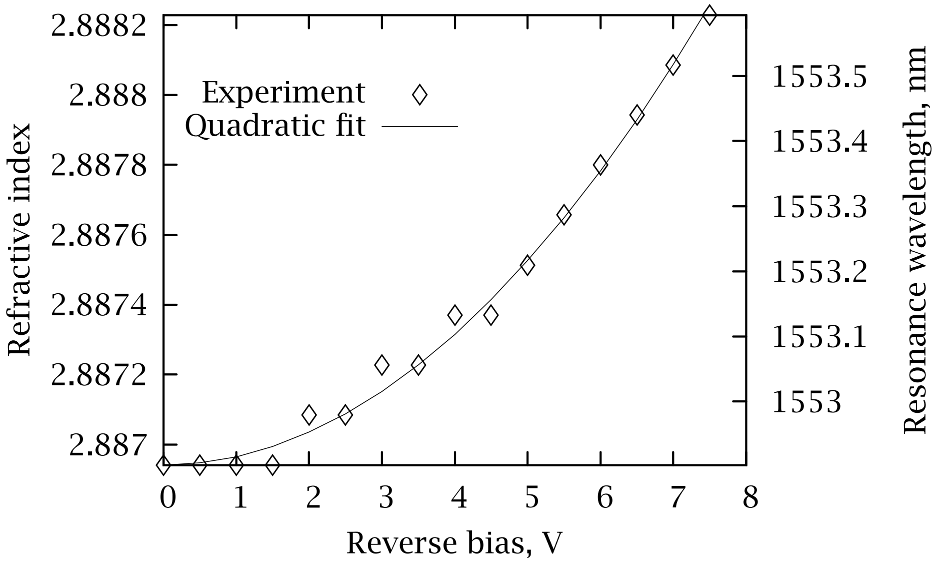

Figure 7.14: Effective refractive index and resonance wavelength versus voltage. The step-like behavior is from the resolution of the optical spectrum analyzer used to acquire the device spectrum.

coefficient for the waveguide is a lower bound for the quadratic electro-optic coefficient of the core because of the high leakage current in the material when under reverse bias. The tuning range of 0.8 nm, or 100 GHz, means that the device is suitable for dense wavelength division multiplexing applications. The curve-fit in Fig. 7.14 allows us to calculate the quadratic electro-optic coefficient for the waveguide as 4.9×10^{-15} cm^2/V^2 at $\sim$ 65 meV from the band edge for our waveguide. Since the quantum-wells occupy roughly half the core of the waveguide, the quadratic electro-optic coefficient for the wells is double that value, i.e., $s_{\mathrm{qw}} = 9.8 \times 10^{-15}$ cm^2/V^2. The obtained quadratic electro-optic coefficient value is compares favorably to the value of 5×10^{-15} cm^2/V^2 reported by Fetterman et al. for a similar MQW structure, at 113 meV from the band edge [128]. Higher values of the quadratic coefficient may be obtained

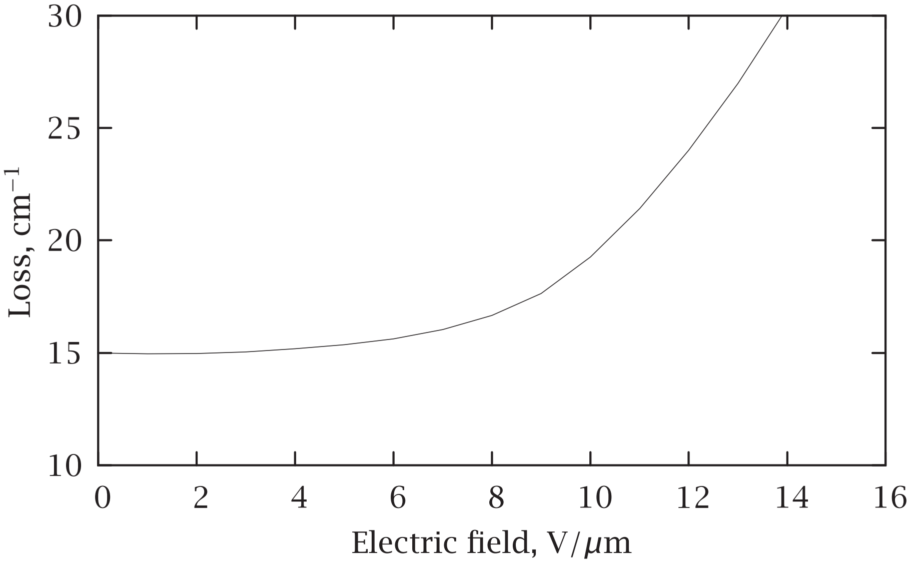

Figure 7.15: Measured loss versus electric field in straight waveguides. The loss in the absence of electric field is estimated as 15 cm^{-1} based on results from similar passive waveguides. The change in loss will be the same in the ring as in the bus, as the electric field affects only the internal loss.

by operating closer to the band edge; however, that has the deleterious effect of decreasing the signal transmission substantially. Zucker et al. report a much higher value for their structure by operating 32 meV from the band edge [176].

The change in throughput with voltage at off-resonance wavelengths allows us to estimate the increase in loss with electric field (Fig. 7.15). The increased loss is due to bandgap shrinkage in the quantum wells [177]. The loss in the absence of any field is due to scattering by rough sidewalls, and mode-mismatch between the modes of the straight and curved sections of the resonator [75].

7.4 Extrapolations of device behavior

In chapter 4, I have demonstrated resonance bandwidths as narrow as 0.25 nm in the same material system, so it is possible to make substantial improvements in the filter characteristics. Bad mask definition in the coupling region during fabrication of the current series of devices resulted in fused bus and resonators. The effect of this was a high coupling between the bus and resonator, giving us the broad (few nm) resonance of the device in this report.

As an example, let us consider the behavior of a high finesse micro-ring resonator add-drop filter made from the same layer structure described in this chapter. We can use the index change from Fig. 7.14 and the loss from Fig. 7.15, $\tau_1 = \tau_2 = 0.989$, and $A = 0.99$ to predict the behavior of a ring resonator with achievable behavior - the corresponding bandwidth is a little over 0.5 nm, which is higher than the best demonstrated bandwidth for similar sized devices in chapters 4 and 5. The simulated drop-port response for an add/drop filter at two voltages is shown in Fig. 7.16. The increased loss affects the bandwidth and decreases the drop-port amplitude, and also changes the extinction on the through port (not shown in the graph). The simulated bandwidth versus electric field is shown in Fig. 7.17. Since the bandwidth increases drastically over the tuning range, the material bandgap must be modified to decrease the change in loss.

7.5 Other configurations

I chose to use the lateral coupling approach for the device described in this chapter because of the simplicity of fabrication. Real-world applications will typically require the use of vertical coupling so that the bus and the ring can be of different bandgaps. Then, we can make not just electro-optic modula-

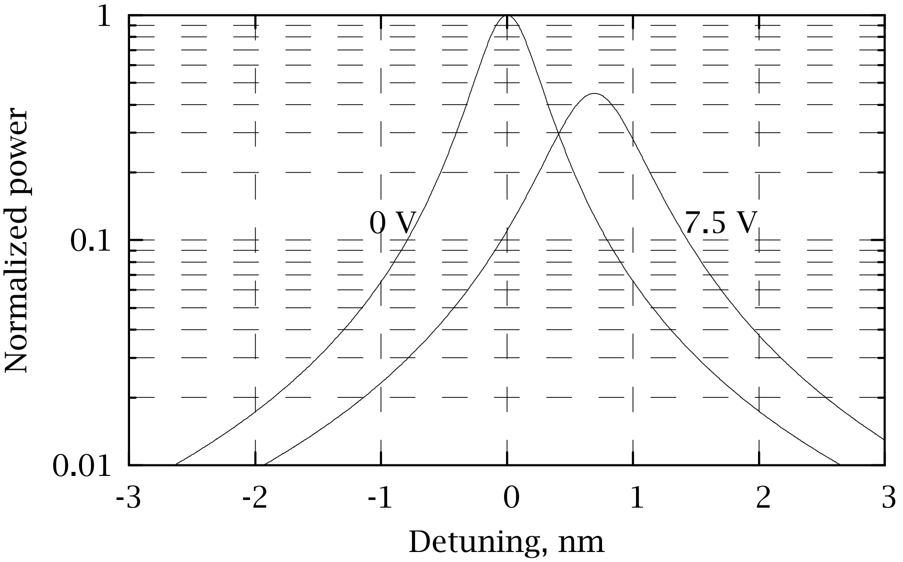

Figure 7.16: Simulated change in spectral response with reverse bias for the layer structure used in this chapter.

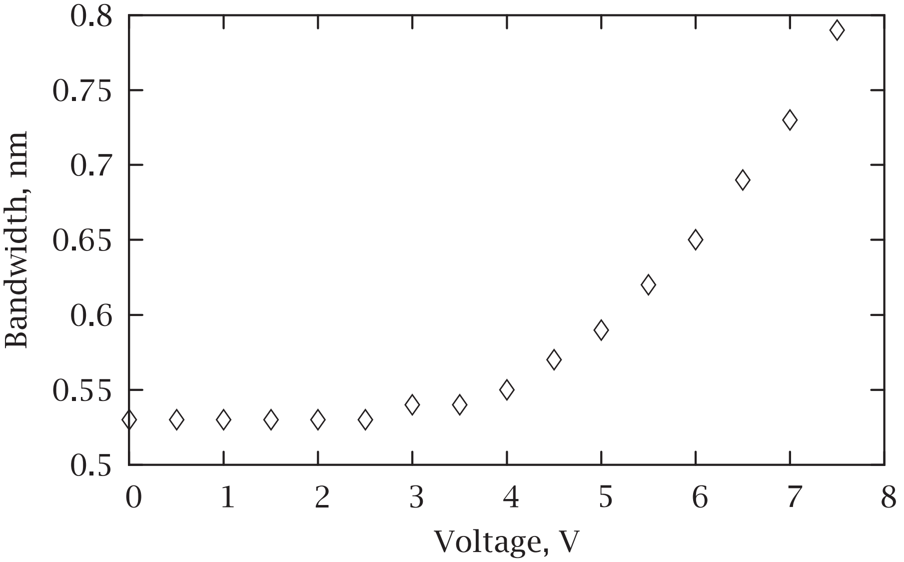

Figure 7.17: Simulated change in bandwidth with electric field across the core for the layer structure used in this chapter.

tors, but also ring lasers, amplifiers, and intensity modulators. Integration of these components could be achieved by making electro-optic modulators on the same side as the bus and changing the bandgap of ring with quantum-well intermixing. Alternately, with the direct-wafer-bonding approach, two wafer bonding steps could be used to make the electro-optically tuned components on the third layer. Two possible configurations for active vertically-coupled rings are shown in Fig. 7.18. In each case, the p- and n- regions can be interchanged. The p-contacts in each case require a planarization step. I have not shown the planarization and passivation layers for clarity. In Fig. 7.18(a), the wafer bonding is achieved with a suitable glue, such as BCB (not shown). In Fig. 7.18(b), I have shown the case for direct-wafer-bonding. An alternate method of achieving a conducting interface would be to planarize the bus level, etchback, and bond with a conducting material, such as Pb-Sn [80] Pd [81], Au-Sn [82], or Pd-In [83, 84].

7.6 Summary

I have demonstrated an ultra-compact tunable micro-ring notch filter. The device is a p-i-n diode, with the intrinsic region forming the waveguide core. The intrinsic region is composed of a superlattice of quantum wells. By applying a reverse bias, I am able to tune the resonance wavelength by 0.8 nm (100 GHz) over 8 V. Direct material property measurements indicate that the effect is electro-optic, and that the quadratic electro-optic coefficient is at least 2.3×10^{-15} cm^2/V^2 which is consistent with values reported in literature. The quadratic electro-optic coefficient for the waveguide is estimated as 4.9×10^{-15} cm^2/V^2; the corresponding value for the wells which comprise the waveguide compares favorably with previous reports. The tuning range is

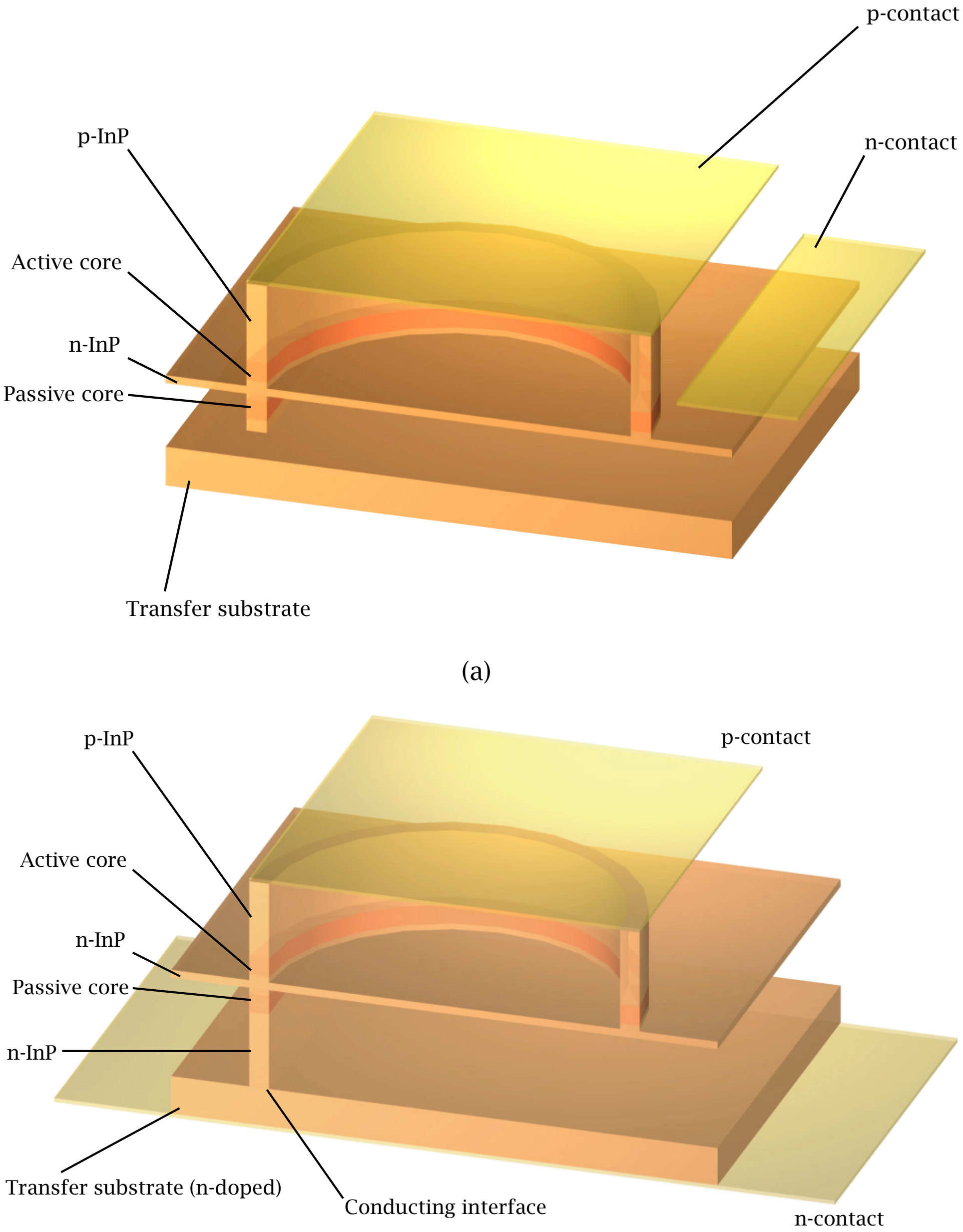

(a)

(b)

Figure 7.18: Two possible configurations for active vertically coupled microring resonator filters. The active core could enable devices like lasers, amplifiers, and electroabsorption and electro-optic modulators.

suitable for WDM applications. However, the increase in loss with reverse bias and consequent change in bandwidth is quite high, and must be addressed by modifying the structure and bandgap suitably.

Note: The electron-beam lithography for this work was performed at the Cornell Nanofabrication Facility (now called the Cornell NanoScale Science and Technology Facility), a member of the National Nanofabrication Users Network, which is supported by the National Science Foundation under Grant ECS-9731293, by its users, by Cornell University, and by Industrial Affiliates.

CHAPTER 8

CONCLUSIONS

8.1 Achievements

I have developed an etch recipe for the InP material system using methane-based reactive ion etching. Using this etch recipe, I have demonstrated InP-based micro-ring resonators in both the vertically and laterally coupled geometries, all-optical logic operation in laterally coupled InP-based micro-ring resonators (in collaboration with Tarek A. Ibrahim), and electro-optic tuning of a laterally-coupled GaInAsP-InP micro-ring resonator.

These devices represent the first demonstration of vertically-coupled micro-rings in the InP material system, the first micron-scale laterally-coupled micro-rings in the InP material system, the smallest laterally-coupled micro-rings in any material system, and the first electro-optically tuned micro-rings in III-V materials.

8.2 Future directions

Much needs to be done in this area to achieve consistent and reproducible filter behavior. Aside from the lithography, the most important component is the etch process, which ideally needs a dedicated reaction chamber to prevent cross-contamination. Also, etching with halogen chemistries may provide improved surface morphology and lower waveguide losses. For electro-optically tuned devices, improved material growth would provide better diode behavior, and enable operation at lower voltages.

Improved device design, i.e., electrically isolating the bus and the ring instead of a single contact for the bus and the ring, would allow high-speed modulation with results similar to other III-V electro-optic and electro-absorption modulators. The problems in planarization for active devices can be addressed by using other materials such as polyimides and spin-on glasses. Using polyimides or spin-on glasses for the planarizing materials would allow the n-side contact to be alloyed, improving the contact resistance.

Finally, a significant issue not tackled in this work is the problem of coupling to the bus waveguides. Currently, we lose at least 6 dB of power in coupling to and from the bus waveguides with lensed fibers. For an integrated system where one needs to go on and off chip just once, and in which the chip incorporates amplifiers, this will not be a crippling problem, but clearly, this figure needs to be improved greatly. There are many promising technologies that are being developed for this, notably adiabatic spot-size and index transformers, so I anticipate that this issue will be solved eventually.

APPENDIX A

COUPLING OF WAVEGUIDES

Here I describe the properties of the coupling matrix following Haus [108]. The output fields are $\mathbf{b} = [b_1\ b_2]^{\mathrm{t}}$, and the input fields are $\mathbf{a} = [a_1\ a_2]^{\mathrm{t}}$. The scattering matrix $\mathbf{S} = s_{ij}$ is

$$\mathbf{b} = \mathbf{S}\mathbf{a}. \tag{A.1}$$

To find the relations between the elements of the scattering matrix, we use time reversal and power conservation. We assume that the two-port system described by the scattering matrix is reciprocal, i.e., the inputs and outputs can be exchanged.

Time reversal arises from the properties of the complex conjugates of the electric and magnetic fields. If $\mathbf{E}$ and $\mathbf{H}$ are solutions of Maxwell's equations, then we can show that $\mathbf{E}^*$ and $-\mathbf{H}^*$ are solutions and the direction of power flow is opposite that of the solution $\mathbf{E}$ and $\mathbf{H}$.

Then, $\mathbf{a}^*$ is a wave travelling in the opposite direction of $\mathbf{a}$. This means that if $\mathbf{a}$ is the input and $\mathbf{b}$ is the output (as defined above), $\mathbf{a}^*$ represents an output for the input $\mathbf{b}^*$. In other words,

$$\begin{aligned} \mathbf{b} &= \mathbf{S}\mathbf{a} && \text{(A.2)} \\ \Rightarrow \mathbf{a}^* &= \mathbf{S}\mathbf{b}^* && \text{(A.3)} \\ \Rightarrow \mathbf{b}^* &= \mathbf{S}^{-1}\mathbf{a}^*. && \text{(A.4)} \end{aligned}$$

Comparing eq. A.4 with eq. A.2, we get

$$\mathbf{S}^* = \mathbf{S}^{-1}. \tag{A.5}$$

Next, we consider power conservation, i.e., $|a_1|^2 + |a_2|^2 = |b_1|^2 + |b_2|^2$.

$$\begin{aligned}
\mathbf{b}^\dagger\mathbf{b} &= \mathbf{a}^\dagger\mathbf{S}^\dagger\mathbf{S}\mathbf{a} && \text{(A.6)}\\
&= \mathbf{a}^\dagger\mathbf{a} && \text{(A.7)}\\
\Rightarrow \mathbf{S}^\dagger\mathbf{S} &= \mathbf{1} && \text{(A.8)}\\
\Rightarrow \mathbf{S}^\dagger &= \mathbf{S}^{-1}. && \text{(A.9)}
\end{aligned}$$

Comparing with eq. A.5, we get

$$\mathbf{S}^* = \mathbf{S}^\dagger. \tag{A.10}$$

The off-diagonal elements give

$$\begin{aligned}
s_{12}^* &= s_{21}^* && \text{(A.11)}\\
\Rightarrow s_{12} &= s_{21}, && \text{(A.12)}
\end{aligned}$$

i.e., **S** is symmetric.

Expanding on the power conservation theme gives

$$\begin{aligned}
s_{11}^*s_{11} + s_{21}^*s_{21} &= 1 && \text{(A.13)}\\
s_{22}^*s_{22} + s_{12}^*s_{12} &= 1 && \text{(A.14)}\\
s_{11}^*s_{12} + s_{21}^*s_{22} &= 0. && \text{(A.15)}
\end{aligned}$$

Using $s_{21} = s_{12}$ in eqs. A.13 and A.14 gives

$$s_{11}^*s_{11} = s_{22}^*s_{22}. \tag{A.16}$$

We are left with three complex unknowns: s_{11}, s_{22}, and s_{12} (or s_{21}). This is as far as we can go without further assumptions.

APPENDIX B

PROCESSES USED

Electron-beam lithography process adapted from recommendations by Teresa Emery (Cornell Nanofabrication Facility). Cr-SiO_2 mask process adapted from recommendations by John Hryniewicz (Little Optics). Original InP etch, modified InP etch, chamber conditioning for InP etch, and Ti etch were developed for this project. Modified etch was developed with D. P. Kelly and M. W. Pruessner based on recommendations from David Lishan (Unaxis). Bromine-methanol thinning adapted from [92]. Other processes adapted from those developed by LPS staff or supplied by manufacturer.

B.1 Lithography

B.1.1 Photo

GCA/Mann DSW 4800 10× i-line stepper. OiR 908 20HC spun at 3500 RPM; pre-bake 60 s at 90 °C; pattern exposed in 10× i-line stepper; post-exposure bake 60 s at 120 °C; developed in OPD 4262 for 60 s; rinsed in deionized water.

B.1.2 Electron-beam

Leica VB6 HR. 100K MW 5 % PMMA in Anisole spun-on at 4000 RPM for 60 s (113 nm-thick film). Bake for 15 min. at 170 °C. 495K MW PMMA A4 in Anisole spun-on at 2000 RPM for 60 s (204 nm-thick film). Bake for 15 min. at 170 °C. Pattern written with 736 $\mu\text{C}/\text{cm}^2$ for small features (waveguides and micro-rings), and 610 $\mu\text{C}/\text{cm}^2$ for large features (device labels). Developed with 2-Methyl-2-Pentanone diluted with 2-Propanol as 1 : 3 for 2 min. 30 s. Sample rinsed with 2-Propanol, dried with N_2.

B.2 Mask definition

B.2.1 Dry-etch patterned masks

(Ti, SiO_2 and Ti-SiO_2) Plasmatherm 790 Series RIE, photoresist mask. Chips cleaned with 2-Propanone, Methanol, 2-Propanol, deionized H_2O. Immersed in OPD 4262 for > 15 min.. SiO_2 deposited for thicknesses of 120, 300, and 500 nm for various samples; 100 nm Ti deposited on 500 nm SiO_2-covered samples; 100 nm Ti deposited on other InP test samples. Samples patterned by photolithography. Pattern transferred to SiO_2-only samples by RIE with CHF_3-O-2, to Ti-SiO_2 samples by RIE successively with SF_6 (for Ti) and CHF_3-O_2 (for SiO_2), Ti-only samples by RIE with SF_6.

B.2.2 InP etch mask

Ni or NiCr patterned by liftoff; Ti, SiO_2 or Ti-SiO_2 patterned by dry-etching with SF_6 plasma (Ti) or CHF_3-O_2 plasma (SiO_2), or both (Ti-SiO_2); Cr-SiO_2 patterned by liftoff (Cr) followed by CHF_3-O_2 plasma (for SiO_2).

B.3 SiO_2 deposition

Oxford Plasmalab PECVD. 12 sccm N_2O, 64 sccm 2% SiH_4/N_2, 300 mT, 10 W, 13.56 MHz RF, 300 °C. Deposition rate = 15 nm/min., refractive index $\sim$ 1.5.

B.4 Metal deposition

Manufacturer specified process on CHA Mark 40 electron-beam evaporator, except NiCr. NiCr deposited using home-made resistive evaporator in LPS packaging lab.

B.5 Plasmatherm 790 Series RIE

B.5.1 SiO_2 etch

18 sccm CHF_3, 2 sccm O_2, 40 mT, 175 W, 8 inch graphite platen, 13.56 MHz RF, room temperature. Etch rate 35 – 40 nm/min., sidewall angle not distinguishable from 90 deg.

B.5.2 Ti etch

20 sccm SF_6, 25 mT, 50 W, 8 inch graphite platen, 13.56 MHz RF, room temperature. Etch rate 10 nm/min., sidewall angle not measured.

B.5.3 InP etch/clean cycle

5 min. etch (original/modified), followed by 3 min. sample clean.

B.5.4 Original InP etch step

8 sccm CH_4, 32 sccm H_2, 10 sccm Ar, 30 mT, −440 V, 8 inch anodized aluminum platen, 13.56 MHz RF, room temperature. Etch rate ∼ 50 nm/min., sidewall angle not distinguishable from 90 deg.

B.5.5 Modified InP etch step

8 sccm CH_4, 32 sccm H_2, 30 mT, −440 V, 8 inch anodized aluminum platen, 13.56 MHz RF, room temperature. Etch rate ∼ 40 nm/min., sidewall angle ca. 88 deg.

B.5.6 Sample clean

16 sccm O_2, 200 mT, −200 V, 8 inch anodized aluminum platen, 13.56 MHz RF, room temperature.

B.5.7 Chamber clean

Manufacturer-supplied process for Plasmatherm 790 Series RIE.

B.5.8 Chamber conditioning

> 3 hr. chamber clean followed by > 33 cycles of original etch/clean.

B.6 Wet-bench processes

B.6.1 Liftoff

Sample with patterned resist treated with H_2SO_4:H_2O 1 : 20 for 60 s; Appropriate thickness of metal evaporated onto chips and chips immersed overnight in 2-Propanone, and rinsed successively in Methanol, 2-Propanol, deionized water, and 2-Propanol, and dried with N_2. Alternately, samples immersed in warm 1-Methyl-2-Pyrrolidinone for > 15 min., and rinsed successively in 1,1,1-Trichloroethane, 2-Propanone, Methanol, 2-Propanol, deionized water, and 2-Propanol, and dried with N_2.

B.6.2 Photoresist mask removal

3 min. O_2 plasma clean with RIE or Matrix asher, immersion in warm 1-Methyl-2-Pyrrolidinone for > 15 min., and rinsing successively with 1,1,1-Trichloroethane, 2-Propanone, Methanol, 2-Propanol, deionized water, 2-Propanol, blow-drying with N_2.

B.6.3 InP etch mask removal

(Ti, SiO_2, Ti-SiO_2) Rinsing with BHF (preferred) or dry-etching in RIE with SF_6 plasma (for Ti) and CHF_3-O_2 plasma (for SiO_2).

B.7 Substrate thinning

B.7.1 Bromine-Methanol

Minimet polisher. Sample mounted with appropriate wax onto quartz disk. Disk held by teflon holder with backside of sample outward. Sample polished with teflon pad in 2.5 % Br_2-Methanol solution. Thinning rate $\sim 5 - 10\ \mu$m/min..

B.7.2 Alumina-based

Logitech polishing machine. Sample mounted on Southbay polishing jig with appropriate wax. Polished with $\sim 10\ \mu$m-grit alumina slurry to 180 μm, followed by ~ 1 μm-grit alumina slurry to 120 μm.

B.8 Scribing, cleaving, mounting

Thinned samples scribed using Karl Suss scriber with a diamond-tipped scribe. Cleaved on cleaving station. Mounted with pick-and-place machine using silver epoxy onto brass or oxide-free copper mounts.

BIBLIOGRAPHY

[1] Lord Rayleigh, “The problem of the whispering gallery,” *Philosophical Magazine*, vol. xx, pp. 1001–1004, 1910.

[2] E. A. J. Marcatili, “Bends in optical dielectric guides,” *The Bell System Technical Journal*, vol. 48, pp. 2103–2132, 1969.

[3] H. P. Weber and R. Ulrich, “A thin-film ring laser,” *Applied Physics Letters*, vol. 19, pp. 38–40, 1971.

[4] R. Ulrich and H. P. Weber, “Unidirectional thin-film ring laser,” *Applied Physics Letters*, vol. 20, pp. 38–40, 1972.

[5] R. Ulrich and H. P. Weber, “Solution-deposited thin films as passive and active light-guides,” *Applied Optics*, vol. 11, pp. 428–434, 1972.

[6] J. Haavisto and G. A. Pajer, “Resonance effects in low-loss ring waveguides,” *Optics Letters*, vol. 5, pp. 510–512, 1980.

[7] L. F. Stokes, M. Chodorow, and H. J. Shaw, “All-single-mode fiber resonator,” *Optics Letters*, vol. 7, pp. 288–290, 1982.

[8] R. G. Walker and C. D. W. Wilkinson, “Integrated optical ring resonators made by silver ion-exchange in glass,” *Applied Optics*, vol. 22, pp. 1029–1035, 1983.

[9] A. Mahapatra and J. M. Connors, "High finesse ring resonators fabrication and analysis," in *Integrated Optical Circuit Engineering*, Innsbruck, Austria, 1986.

[10] J. M. Connors and A. Mahapatra, "High finesse ring resonators made by silver ion exchange in glass," *Journal of Lightwave Technology*, vol. LT-5, pp. 1686–1689, 1987.

[11] K. Honda, E. M. Garmire, and K. E. Wilson, "Characteristics of an integrated optics ring resonator fabricated in glass," *Journal of Lightwave Technology*, vol. LT-2, pp. 714–719, 1984.

[12] A. Naumaan and J. T. Boyd, "Ring resonator fabricated in phosphosilicate glass films deposited by chemical vapor deposition," *Journal of Lightwave Technology*, vol. LT-4, pp. 1294–1303, 1986.

[13] K.-H. Tietgen, "Tunable integrated optical ring resonator," in *Topical Meeting on Integrated and Guided Wave Optics*, Kissimee, FL, 1984.

[14] A. Mahapatra and W. C. Robinson, "Integrated-optic ring resonators made by proton exchange in lithium niobate," *Applied Optics*, vol. 24, pp. 2285–2286, 1985.

[15] K. Oda, N. Takato, and H. Toba, "A wide-FSR waveguide double-ring resonator for optical FDM transmission systems," *Journal of Lightwave Technology*, vol. 9, pp. 728–736, 1991.

[16] T. Kominato, Y. Ohmori, N. Takato, H. Okazaki, and M. Yasu, "Ring resonators composed of GeO_2-doped silica waveguides," *Journal of Lightwave Technology*, vol. 10, pp. 1781–1788, 1992.

[17] W. J. Wang, S. Honkanen, S. I. Najafi, and A. Tervonen, "New integrated optical ring resonator in glass," *Electronics Letters*, vol. 28, pp. 1967–1968, 1992.

[18] S. T. Chu, B. E. Little, P. Wugen, T. Kaneko, and Y. Kokubun, "Cascaded microring resonators for crosstalk reduction and spectrum cleanup in add-drop filters," *IEEE Photonics Technology Letters*, vol. 11, pp. 1423–1425, 1999.

[19] S. T. Chu, B. E. Little, W. Pan, and Y. Kokubun, "A cross-grid array of microresonators for very large scale integrated photonic circuits," in *Conference on Lasers and Electro-Optics*, San Francisco, CA, 1999.

[20] S. T. Chu, P. Wugan, S. Suzuki, B. E. Little, S. Sato, and Y. Kokubun, "Temperature insensitive vertically coupled microring resonator add/drop filters by means of a polymer overlay," *IEEE Photonics Technology Letters*, vol. 11, pp. 1138–1140, 1999.

[21] B. E. Little, S. T. Chu, W. Pan, D. Ripin, T. Kaneko, Y. Kokubun, and E. P. Ippen, "Vertically coupled glass microring resonator channel dropping filters," *IEEE Photonics Technology Letters*, vol. 11, pp. 215–217, 1999.

[22] S. T. Chu, B. E. Little, W. Pan, T. Kaneko, and Y. Kokubun, "Second order filter response from parallel coupled glass microring resonators," *IEEE Photonics Technology Letters*, vol. 11, pp. 1426–1428, 1999.

[23] S. T. Chu, W. Pan, S. Sato, T. Kaneko, B. E. Little, and Y. Kokubun, "Wavelength trimming of a microring resonator filter by means of a UV sensitive polymer overlay," *IEEE Photonics Technology Letters*, vol. 11, pp. 688–690, 1999.

[24] Y. Kokubun, S. Kubota, and S. T. Chu, "Polarisation-independent vertically coupled microring resonator filter," *Electronics Letters*, vol. 37, pp. 90–92, 2001.

[25] Y. Yanagase, S. Suzuki, Y. Kokubun, and S. T. Chu, "Box-like filter response by vertically series coupled microring resonator filter," in *European Conference on Optical Communications*, Amsterdam, The Netherlands, 2001.

[26] J. Bismuth, P. Gidon, F. Revol, and S. Valette, "Low-loss ring resonators fabricated from silicon based integrated optics technologies," *Electronics Letters*, vol. 27, pp. 722–724, 1991.

[27] S. Suzuki, K. Shuto, and Y. Hibino, "Integrated-optic ring resonators with two stacked layers of silica waveguide on Si," *IEEE Photonics Technology Letters*, vol. 4, pp. 1256–1258, 1992.

[28] T. Kominato, Y. Hibino, and K. Onose, "Silica-based finesse-variable ring resonator," *IEEE Photonics Technology Letters*, vol. 5, pp. 560–562, 1993.

[29] S. Suzuki, K. Oda, and Y. Hibino, "Integrated-optic double-ring resonators with a wide free spectral range of 100 GHz," *Journal of Lightwave Technology*, vol. 13, pp. 1766–1771, 1995.

[30] P. Katila, P. Heimala, and J. Aarnio, "Thermo-optically controlled ring resonator on silicon," *Electronics Letters*, vol. 32, pp. 1005–1006, 1996.

[31] J. S. Foresi, B. E. Little, G. Steinmeyer, E. Thoen, S. T. Chu, H. A. Haus, E. P. Ippen, L. C. Kimerling, and W. Greene, "Si/SiO$_2$ micro-ring resonator optical add/drop filters," in *Conference on Lasers and Electro-Optics*, Baltimore, MD, 1997.

[32] B. E. Little, J. S. Foresi, G. Steinmeyer, E. R. Thoen, S. T. Chu, H. A. Haus, E. P. Ippen, L. C. Kimerling, and W. Greene, "Ultra-compact Si-SiO_2 microring resonator optical channel dropping filters," *IEEE Photonics Technology Letters*, vol. 10, pp. 549–551, 1998.

[33] D. R. Lim, B. E. Little, K. K. Lee, M. Morse, H. H. Fujimoto, H. A. Haus, and L. C. Kimerling, "Micron-sized channel dropping filters using silicon waveguide devices," in *Optical Devices for Fiber Communication*, Boston, MA, 1999.

[34] D. J. W. Klunder, F. S. Tan, T. van der Veen, H. F. Bulthuis, H. J. W. M. Hoekstra, and A. Driessen, "Design and characterization of waveguide-coupled cylindrical microring resonators in Si_3N_4," in *IEEE Lasers and Electro-Optics Society, 13th Annual Meeting*, Rio Grande, Puerto Rico, 2000.

[35] D. J. W. Klunder, E. Krioukov, F. S. Tan, T. van der Veen, H. F. Bulthuis, G. Sengo, C. Otto, H. J. W. M. Hoekstra, and A. Driessen, "Vertically and laterally waveguide-coupled cylindrical microresonators in Si_3N_4 on SiO_2 technology," *Applied Physics B (Lasers and Optics)*, vol. B73, pp. 603–608, 2001.

[36] S. Suzuki, Y. Hatakeyama, Y. Kokubun, and S. T. Chu, "Precise control of wavelength channel spacing of microring resonator add-drop filter array," *Journal of Lightwave Technology*, vol. 20, pp. 745–750, 2002.

[37] B. E. Little, "A VLSI photonics platform," in *Optical Fiber Communication*, Atlanta, GA, 2003.

[38] P. Rabiei and W. H. Steier, "Micro-ring resonators using polymer materials," in *Conference on Lasers and Electro Optics*, Baltimore, MD, 2001.

[39] P. Rabiei, W. H. Steier, C. Zhang, C.-G. Wang, and H. J. Lee, "Polymer micro-ring modulator with 1 THz FSR," in *Conference on Lasers and Electro-Optics*, Long Beach, CA, 2002.

[40] P. Rabiei, W. H. Steier, C. Zhang, and L. R. Dalton, "Polymer micro-ring filters and modulators," *Journal of Lightwave Technology*, vol. 20, pp. 1968–1975, 2002.

[41] W. Y. Chen, R. Grover, T. A. Ibrahim, V. Van, and P.-T. Ho, "Compact single-mode benzocyclobutene microracetrack resonators," in *Integrated Photonics Research*, Washington, DC, 2003.

[42] D. Rafizadeh, J. P. Zhang, S. C. Hagness, A. Taflove, K. A. Stair, S. T. Ho, and R. C. Tiberio, "Waveguide-coupled AlGaAs/GaAs microcavity ring and disk resonators with high finesse and 21.6 nm free spectral range," *Optics Letters*, vol. 22, pp. 1244–1246, 1997.

[43] D. Rafizadeh, J. P. Zhang, S. C. Hagness, A. Taflove, K. A. Stair, S. T. Ho, and R. C. Tiberio, "Temperature tuning of microcavity ring and disk resonators at 1.5 μm," in *IEEE Lasers and Electro-Optics Society, 10th Annual Meeting*, San Francisco, CA, 1997.

[44] J. V. Hryniewicz, P. P. Absil, B. E. Little, and P.-T. Ho, "Semiconductor microring resonators for integrated photonics," in *Integrated Photonics Research*, Québec City, Canada, 2000.

[45] J. V. Hryniewicz, P. P. Absil, B. E. Little, R. A. Wilson, L. G. Joneckis, and P.-T. Ho, "Microring resonator notch filters," in *Conference on Lasers and Electro-Optics*, San Francisco, CA, 2000.

[46] J. V. Hryniewicz, P. P. Absil, B. E. Little, and P.-T. Ho, "Higher order filter response in coupled microring resonators," *IEEE Photonics Technology Letters*, vol. 12, pp. 320–322, 2000.

[47] P. P. Absil, J. V. Hryniewicz, B. E. Little, P. S. Cho, R. A. Wilson, L. G. Joneckis, and P.-T. Ho, "Wavelength conversion in GaAs micro-ring resonators," *Optics Letters*, vol. 25, pp. 554–556, 2000.

[48] P. P. Absil, J. V. Hryniewicz, B. E. Little, R. A. Wilson, L. G. Joneckis, and P.-T. Ho, "Compact microring notch filters," *IEEE Photonics Technology Letters*, vol. 12, pp. 398–400, 2000.

[49] P. P. Absil, J. V. Hryniewicz, B. E. Little, F. G. Johnson, and P.-T. Ho, "Vertically coupled microring resonators using polymer wafer bonding," *IEEE Photonics Technology Letters*, vol. 13, pp. 49–51, 2001.

[50] R. Grover, P. P. Absil, V. Van, J. V. Hryniewicz, B. E. Little, O. S. King, F. G. Johnson, L. C. Calhoun, and P.-T. Ho, "Vertically coupled GaAs-AlGaAs and GaInAsP-InP microring resonators," in *Optical Fiber Communication*, Anaheim, CA, 2001.

[51] P. P. Absil, J. V. Hryniewicz, B. E. Little, F. G. Johnson, and P.-T. Ho, "Wavelength selective mirror using notched microring resonators," in *IEEE Lasers and Electro-Optics Society, 14th Annual Meeting*, San Diego, CA, 2001.

[52] V. Van, T. A. Ibrahim, P. P. Absil, R. Grover, J. V. Hryniewicz, B. E. Little, F. G. Johnson, and P.-T. Ho, "Periodically-coupled GaAs/AlGaAs microring array filter with wide free spectral range," in *Integrated Photonics Research*, Monteray, CA, 2001.

[53] S. L. McCall, A. F. J. Levi, R. E. Slusher, S. J. Pearton, and R. A. Logan, “Whispering-gallery mode microdisk lasers,” *Applied Physics Letters*, vol. 60, pp. 289–291, 1992.

[54] D. Y. Chu, M. K. Chin, N. J. Sauer, Z. Xu, T. Y. Chang, and S. T. Ho, “1.5 μm InGaAs/InAlGaAs quantum-well microdisk lasers,” *IEEE Photonics Technology Letters*, vol. 5, pp. 1353–1355, 1993.

[55] C. R. Abernathy, S. J. Pearton, J. D. MacKenzie, J. R. Mileham, S. R. Bharatan, V. Krishnamoorthy, K. S. Jones, M. Hagerott-Crawford, R. J. Shul, S. P. Kilcoyne, J. M. Zavada, D. Zhang, and R. M. Kolbas, “Growth and fabrication of GaN-InGaN microdisk laser structures,” *Solid-State Electronics*, vol. 39, pp. 311–313, 1996.

[56] T. Baba, P. Fujita, A. Sakai, M. Kihara, and R. Watanabe, “Lasing characteristics of GaInAsP-InP strained quantum-well microdisk injection lasers with diameter of $2-10$ μm,” *IEEE Photonics Technology Letters*, vol. 9, pp. 878–880, 1997.

[57] L. Dai, B. Zhang, R. A. Mair, K. Zeng, J. Lin, H. Jigang, A. Botchkarev, W. Kim, H. Morkoc, and M. A. Khan, “Optical properties and resonant modes in GaN/AlGaN and InGaN/GaN multiple quantum well microdisk cavities,” in *Semiconductor Lasers III*, Beijing, China, 1998.

[58] R. A. Mair, K. C. Zeng, J. Y. Lin, H. X. Jiang, B. Zhang, L. Dai, A. Botchkarev, W. Kim, H. Morkoc, and M. A. Khan, “Optical modes within III-nitride multiple quantum well microdisk cavities,” *Applied Physics Letters*, vol. 72, pp. 1530–1532, 1998.

[59] D. V. Tishinin, P. D. Dapkus, A. E. Bond, I. Kim, C. K. Lin, and J. O’Brien, “Vertical resonant couplers with precise coupling efficiency control fab-

ricated by wafer bonding," *IEEE Photonics Technology Letters*, vol. 11, pp. 1003–1005, 1999.

[60] L. Djaloshinski and M. Orenstein, "Disk and ring microcavity lasers and their concentric coupling," *IEEE Journal of Quantum Electronics*, vol. 35, pp. 737–744, 1999.

[61] N. B. Rex, R. K. Chang, and L. J. Guido, "Threshold minimization and directional laser emission from GaN microdisks," in *Laser Resonators*, San Jose, CA, 2000.

[62] R. Grover, P. P. Absil, V. Van, J. V. Hryniewicz, B. E. Little, O. S. King, L. C. Calhoun, F. G. Johnson, and P.-T. Ho, "Vertically coupled GaInAsP-InP microring resonators," *Optics Letters*, vol. 26, pp. 506–508, 2001.

[63] R. Grover, V. Van, T. A. Ibrahim, P. P. Absil, L. C. Calhoun, F. G. Johnson, J. V. Hryniewicz, and P.-T. Ho, "Parallel-cascaded semiconductor microring resonators for high-order and wide-FSR filters," *Journal of Lightwave Technology*, vol. 20, pp. 900–905, 2002.

[64] K. Djordjev, S.-J. Choi, S.-J. Choi, and P. D. Dapkus, "High-*Q* vertically coupled InP microdisk resonators," *IEEE Photonics Technology Letters*, vol. 14, pp. 331–332, 2002.

[65] K. Djordjev, S.-J. Choi, S.-J. Choi, and P. D. Dapkus, "Microdisk tunable resonant filters and switches," *IEEE Photonics Technology Letters*, vol. 14, pp. 828–830, 2002.

[66] G. Griffel, J. H. Abeles, R. J. Menna, A. M. Braun, J. C. Connolly, and M. King, "Low-threshold InGaAsP ring lasers fabricated using bi-level

dry etching," *IEEE Photonics Technology Letters*, vol. 12, pp. 146–148, 2000.

[67] D. G. Rabus and M. Hamacher, "MMI-coupled ring resonators in GaInAsP-InP," *IEEE Photonics Technology Letters*, vol. 13, pp. 812–814, 2001.

[68] D. G. Rabus, M. Hamacher, and H. Heidrich, "Active and passive microring resonator filter applications in GaInAsP/InP," in *Indium Phosphide and Related Materials*, Nara, Japan, 2001.

[69] D. G. Rabus, M. Hamacher, U. Troppenz, and H. Heidrich, "High-Q channel dropping filters using ring resonators with integrated SOAs," *IEEE Photonics Technology Letters*, vol. 14, pp. 1442–1444, 2002.

[70] S. L. Rommel, J.-H. Jang, W. Lu, G. Cueva, L. Zhou, I. Adesida, G. A. Pajer, R. W. Whaley, A. Lepore, Z. Schellanbarger, and J. H. Abeles, "Effect of H_2 on the etch profile of InP/InGaAsP alloys in $Cl_2/Ar/H_2$ inductively coupled plasma reactive ion etching chemistries for photonic device fabrication," *Journal of Vacuum Science & Technology B*, vol. 20, pp. 1327–1330, 2002.

[71] R. Grover, T. A. Ibrahim, T. N. Ding, L.-C. Kuo, S. Kanakaraju, L. C. Calhoun, and P.-T. Ho, "Ultracompact single-mode GaInAsP-InP microracetrack resonators," in *Integrated Photonics Research*, Washington, DC, 2003.

[72] R. Grover, T. A. Ibrahim, T. N. Ding, Y. Leng, L.-C. Kuo, S. Kanakaraju, K. Amarnath, L. C. Calhoun, and P.-T. Ho, "Laterally coupled InP-based single-mode microracetrack notch filter," *IEEE Photonics Technology Letters*, 2003.

[73] R. Grover, T. A. Ibrahim, S. Kanakaraju, M. L. Lucas, L. C. Calhoun, and P.-T. Ho, "Tunable GaInAsP-InP optical microresonator notch filter," *submitted to IEEE Photonics Technology Letters*, 2003.

[74] B. E. Little, J. P. Laine, and S. T. Chu, "Surface-roughness-induced contradirectional coupling in ring and disk resonators," *Optics Letters*, vol. 22, pp. 4–6, 1997.

[75] V. Van, P. P. Absil, J. V. Hryniewicz, and P.-T. Ho, "Propagation loss in single-mode GaAs-AlGaAs microring resonators: measurement and model," *Journal of Lightwave Technology*, vol. 19, pp. 1734–1739, 2001.

[76] M. Heiblum and J. H. Harris, "Analysis of curved optical waveguides by conformal transformation," *IEEE Journal of Quantum Electronics*, vol. QE-11, pp. 75–83, 1975.

[77] M. Heiblum and J. H. Harris, "Correction to "Analysis of curved optical waveguides by conformal transformation"," *IEEE Journal of Quantum Electronics*, vol. 12, pp. 313–313, 1976.

[78] D. Marcuse, "Bend loss of slab and fiber modes computed with diffraction theory," *IEEE Journal of Quantum Electronics*, vol. 29, pp. 2957–2961, 1993.

[79] F. Niklaus, P. Enoksson, E. Kälvesten, and G. Stemme, "Low-temperature full wafer adhesive bonding," *Journal of Micromechanics and Microengineering*, vol. 11, pp. 100–107, 2001.

[80] P. A. Moskowitz, H. L. Yeh, and S. K. Ray, "Thermal dry process soldering," *Journal of Vacuum Science & Technology A*, vol. 4, pp. 838–840, 1985.

[81] I. H. Tan, C. Reaves, A. L. Holmes Jr., E. L. Hu, J. E. Bowers, and S. DenBaars, “Low-temperature Pd bonding of III-V semiconductors,” *Electronics Letters*, vol. 31, pp. 588–589, 1995.

[82] G. R. Dohle, T. J. Drabik, J. J. Callahan, and K. P. Martin, “Low temperature bonding of epitaxial lift off devices with AuSn,” *IEEE Transactions on Components, Packaging, and Manufacturing Technology, Part B*, vol. 19, pp. 575–580, 1996.

[83] W. S. Wong, A. B. Wengrow, Y. Cho, A. Salleo, N. J. Quitoriano, N. W. Cheung, and T. Sands, “Integration of GaN thin films with dissimilar substrate materials by Pd-In metal bonding and laser lift-off,” *Journal of Electronic Materials*, vol. 28, pp. 1409–1413, 1999.

[84] W. S. Wong, T. Sands, N. W. Cheung, M. Kneissl, D. P. Bour, P. Mei, L. T. Romano, and N. M. Johnson, “$In_xGa_{1-x}N$ light emitting diodes on Si substrates fabricated by Pd-In metal bonding and laser lift-off,” *Applied Physics Letters*, vol. 77, pp. 2822–2824, 2000.

[85] M. A. Raburn, B. Liu, K. Rauscher, Y. Okuno, N. Dagli, and J. E. Bowers, “3-D photonic circuit technology,” *IEEE Journal of Selected Topics in Quantum Electronics*, vol. 8, pp. 935–942, 2002.

[86] S. Adachi, “Material parameters of $In_{1-x}Ga_xAs_yP_{1-y}$ and related binaries,” *Journal of Applied Physics*, vol. 53, pp. 8775–8792, 1982.

[87] S. Adachi, “Refractive indices of III-V compounds: Key properties of InGaAsP relevant to device design,” *Journal of Applied Physics*, vol. 53, pp. 5863–5869, 1982.

[88] S. Adachi, “Optical properties of InGaAsP: discussion,” in *Properties of Indium Phosphide*, S. Adachi, Ed., EMIS Datareviews Series. IEE, Inspec, London, UK, 1989.

[89] S. Adachi, *Physical Properties of III-V Semiconductor Compounds*, John Wiley & Sons, New York, NY, 1992.

[90] S. Adachi, Ed., *Properties of Aluminum Gallium Arsenide*, EMIS Datareviews Series. IEE, Inspec, London, UK, 1993.

[91] R. J. Deri and M. A. Emanuel, “Consistent formula for the refractive index of $\mathrm{Al}_x\mathrm{Ga}_{1-x}\mathrm{As}$ below the band edge,” *Journal of Applied Physics*, vol. 77, pp. 4667–4672, 1995.

[92] M. V. Sullivan and G. A. Kolb, “The chemical polishing of gallium arsenide in bromine-methanol,” *Journal of the Electrochemical Society*, vol. 110, pp. 585–587, 1963.

[93] S. B. Phatak and G. Kelner, “Material selective etching in the system InGaAsP/InP,” *Journal of the Electrochemical Society*, vol. 126, pp. 287–292, 1979.

[94] G. C. DeSalvo, W. F. Tseng, and J. Comas, “Etch rates and selectivities of citric acid/hydrogen peroxide on GaAs, $\mathrm{Al}_{0.3}\mathrm{Ga}_{0.7}\mathrm{As}$, $\mathrm{In}_{0.3}\mathrm{Ga}_{0.8}\mathrm{As}$, $\mathrm{In}_{0.53}\mathrm{Ga}_{0.47}\mathrm{As}$, $\mathrm{In}_{0.52}\mathrm{As}_{0.48}\mathrm{As}$ and InP,” *Journal of the Electrochemical Society*, vol. 139, pp. 831–835, 1992.

[95] H. Fourre, F. Diette, and A. Cappy, “Selective wet etching of lattice-matched InGaAs/InAlAs on InP and metamorphic InGaAs/InAlAs on GaAs using succinic acid/hydrogen peroxide solution,” *Journal of Vacuum Science & Technology B*, vol. 14, pp. 3400–3402, 1996.

[96] F. G. Johnson, O. S. King, F. Seiferth, D. R. Stone, R. D. Whaley, M. Dagenais, and Y. J. Chen, "Solid source molecular beam epitaxy of low threshold 1.55 μm wavelength GaInAs/GaInAsP/InP semiconductor lasers," *Journal of Vacuum Science & Technology B*, vol. 14, pp. 2753–2756, 1996.

[97] F. G. Johnson, O. S. King, F. Seiferth, S. Horst, D. R. Stone, R. D. Whaley, M. Dagenais, and Y. J. Chen, "Solid source MBE growth and regrowth of 1.55 μm wavelength GaInAsP/InP ridge lasers," *Journal of Crystal Growth*, vol. 175, pp. 46–51, 1997.

[98] J. V. Hryniewicz, Y. J. Chen, S. H. Hsu, C. H. D. Lee, and G. A. Porkolab, "Ultrahigh vacuum chemically assisted ion beam etching system with a three grid ion source," *Journal of Vacuum Science & Technology A*, vol. 15, pp. 616–621, 1997.

[99] S. Agarwala, S. C. Horst, O. S. King, R. A. Wilson, D. R. Stone, M. Dagenais, and Y. J. Chen, "High-density inductively coupled plasma etching of GaAs/AlGaAs in $BCl_3/Cl_2/Ar$: A study using a mixture design experiment," *Journal of Vacuum Science & Technology B*, vol. 16, pp. 511–514, 1998.

[100] S. Agarwala, O. S. King, S. C. Horst, R. A. Wilson, D. R. Stone, M. Dagenais, and Y. J. Chen, "Response surface study of inductively coupled plasma etching of GaAs/AlGaAs in BCl_3/Cl_2," *Journal of Vacuum Science & Technology A*, vol. 17, pp. 52–55, 1999.

[101] R. D. Whaley, B. Gopalan, M. Dagenais, R. D. Gomez, F. G. Johnson, S. Agarwala, O. King, and D. R. Stone, "Use of atomic force microscopy for analysis of high performance InGaAsP/InP semiconductor lasers

with dry-etched facets," *Journal of Vacuum Science and Technology B*, vol. 16, pp. 1007–1011, 1998.

[102] R. Grover, J. V. Hryniewicz, O. S. King, and V. Van, "Process development of methane-hydrogen-argon-based deep dry-etching of InP for high aspect-ratio structures with vertical facet-quality sidewalls," *Journal of Vacuum Science & Technology B*, vol. 19, pp. 1694–1698, 2001.

[103] P. K. Tien, "Light waves in thin films and integrated optics," *Applied Optics*, vol. 10, pp. 2395–2413, 1971.

[104] G. Agrawal, *Nonlinear Fiber Optics*, Academic Press, San Diego, CA, 2nd edition, 1995.

[105] C. K. Madsen and J. H. Zhao, *Optical Filter Design and Analysis*, John Wiley & Sons, New York, NY, 1999.

[106] G. B. Hocker and W. K. Burns, "Mode dispersion in diffused channel waveguides by the effective index method," *Applied Optics*, vol. 16, pp. 113–118, 1977.

[107] J. Buus, "The effective index method and its application to semiconductor lasers," *IEEE Journal of Quantum Electronics*, vol. QE-18, pp. 1083–1089, 1982.

[108] H. A. Haus, *Waves and fields in optoelectronics*, Prentice-Hall, Englewood Cliffs, NJ, 1984.

[109] A. S. Sedra and K. C. Smith, *Microelectronic Circuits*, Oxford University Press, New York, NY, fourth edition, 1998.

[110] B. E. Little, S. T. Chu, H. A. Haus, J. Foresi, and J. P. Laine, "Microring resonator channel dropping filters," *Journal of Lightwave Technology*, vol. 15, pp. 998–1005, 1997.

[111] G. Barbarossa and A. M. Matteo, "Novel double-ring optical-guided-wave Vernier resonator," *IEE Proceedings (Optoelectronics)*, vol. 144, pp. 203–208, 1997.

[112] B. E. Little, S. T. Chu, J. V. Hryniewicz, and P. P. Absil, "Filter synthesis for periodically coupled microring resonators," *Optics Letters*, vol. 25, pp. 344–346, 2000.

[113] G. Griffel, "Vernier effect in asymmetrical ring resonator arrays," *IEEE Photonics Technology Letters*, vol. 12, pp. 1642–1644, 2000.

[114] A. Melloni, "Synthesis of a parallel-coupled ring-resonator filter," *Optics Letters*, vol. 26, pp. 917–919, 2001.

[115] S. M. Sze, *Physics of Semiconductor Devices*, John Wiley & Sons, second edition, 1981.

[116] M. B. Yairi and D. A. B. Miller, "Equivalence of diffusive conduction and giant ambipolar diffusion," *Journal of Applied Physics*, vol. 91, pp. 4374–4381, 2002.

[117] A. Miller, "Transient grating studies of carrier diffusion and mobility in semiconductors," in *Nonlinear Optics in Semiconductors II*, E. Garmire and A. Kost, Eds., vol. 59 of *Semiconductors and Semimetals*, pp. 287–312. Academic Press, San Diego, CA, 1999.

[118] C. H. Lee, P. S. Mak, and A. P. DeFonzo, “Optical control of millimeter-wave propagation in dielectric waveguides,” *IEEE Journal of Quantum Electronics*, vol. 16, pp. 277–287, 1980.

[119] J. D. Jackson, *Classical Electrodynamics*, John Wiley & Sons, New York, NY, third edition, 1999.

[120] R. W. Boyd, *Nonlinear Optics*, Academic Press, San Diego, CA, 1992.

[121] K. Djordjev, S.-J. Choi, S.-J. Choi, and P. D. Dapkus, “Active semiconductor microdisk devices,” *Journal of Lightwave Technology*, vol. 20, pp. 105–113, 2002.

[122] S. Adachi and K. Oe, “Linear electro-optic effects in zincblende-type semiconductors: Key properties of InGaAsP relevant to device design,” *Journal of Applied Physics*, vol. 56, pp. 74–80, 1984.

[123] S. Adachi and K. Oe, “Quadratic electro-optic (Kerr) effects in zincblende-type semiconductors: Key properties of InGaAsP relevant to device design,” *Journal of Applied Physics*, vol. 56, pp. 1499–1504, 1984.

[124] D. A. B. Miller, D. S. Chemla, and S. Schmitt-Ring, “Relation between electroabsorption in bulk semiconductors and in quantum wells: The quantum-confined Franz-Keldysh effect,” *Physical Review B*, vol. 33, pp. 6976–6982, 1986.

[125] J. P. Donnelly, H. Q. Le, E. A. Swanson, S. H. Groves, A. Darwish, and E. P. Ippen, “Nondegenerate four-wave mixing wavelength conversion in low-loss passive InGaAsP-InP quantum well waveguides,” *IEEE Photonics Technology Letters*, vol. 8, pp. 623–625, 1996.

[126] S. L. Chuang, *Physics of Optoelectronic Devices*, John Wiley & Sons, New York, NY, 1995.

[127] D. A. B. Miller, D. S. Chemla, T. C. Damen, A. C. Gossard, W. Wiegmann, T. H. Wood, and C. A. Burrus, "Band-edge electroabsorption in quantum well structures: the quantum-confined Stark effect," *Physical Review Letters*, vol. 53, pp. 2173–2176, 1984.

[128] M. Fetterman, C.-P. Chao, and S. R. Forrest, "Fabrication and analysis of high-contrast InGaAsP-InP Mach-Zehnder modulators for use at 1.55 μm wavelength," *IEEE Photonics Technology Letters*, vol. 8, pp. 69–71, 1996.

[129] L. A. Coldren, K. Furuya, B. I. Miller, J. A. Rentschler, A. H. Dayem, and P. Mankiewich, "Etched mirrors, grooves and surfaces for GaInAsP/InP integrated optical devices using stop-etch crystal planes," in *Topical Meeting on Integrated and Guided-Wave Optics*, Pacific Grove, CA, 1982.

[130] J. W. Coburn and H. F. Winters, "Plasma etching - A discussion of mechanisms," *Journal of Vacuum Science & Technology*, vol. 16, pp. 391–403, 1979.

[131] L. A. Coldren, K. Iga, B. I. Miller, and J. A. Rentschler, "GaInAsP/InP stripe-geometry laser with reactive-ion-etched facet," *Applied Physics Letters*, vol. 37, pp. 681–683, 1980.

[132] M. A. Bösch, L. A. Coldren, and E. Good, "Reactive ion beam etching of InP with Cl_2," *Applied Physics Letters*, vol. 38, pp. 264–266, 1981.

[133] L. A. Coldren, B. I. Miller, K. Iga, and J. A. Rentschler, "Monolithic two-section GaInAsP/InP active-optical-resonator devices formed by reactive ion etching," *Applied Physics Letters*, vol. 38, pp. 315–317, 1981.

[134] U. Niggebrügge, M. Klug, and G. Garus, "A novel process for reactive ion etching on InP, using CH_4/H_2," in *Gallium Arsenide and Related Compounds*, New York, NY, 1986.

[135] T. R. Hayes, M. A. Dreisbach, P. M. Thomas, W. C. Dautremont-Smith, and L. A. Heimbrook, "Reactive ion etching of InP using CH_4/H_2 mixtures: Mechanisms of etching and anisotropy," *Journal of Vacuum Science & Technology B*, vol. 7, pp. 1130–1140, 1989.

[136] T. R. Hayes, U. K. Chakrabarti, F. A. Baiocchi, A. B. Emerson, H. S. Luftman, and W. C. Dautremont-Smith, "Damage to InP and InGaAsP surfaces resulting from CH_4/H_2 reactive ion etching," *Journal of Applied Physics*, vol. 68, pp. 785–792, 1990.

[137] S. J. Pearton, U. K. Chakrabarti, and F. A. Baiocchi, "Electrical and structural changes in the near surface of reactively ion etched InP," *Applied Physics Letters*, vol. 55, pp. 1633–1635, 1989.

[138] S. J. Pearton, U. K. Chakrabarti, A. P. Kinsella, D. Johnson, and C. Constantine, "Electron cyclotron resonance plasma etching of InP in $CH_4/H_2/Ar$," *Applied Physics Letters*, vol. 56, pp. 1424–1426, 1990.

[139] S. J. Pearton, U. K. Chakrabarti, A. Katz, A. P. Perley, W. S. Hobson, and C. Constantine, "Comparison of $CH_4/H_2/Ar$ reactive ion etching and electron cyclotron resonance plasma etching of In-based III-V alloys," *Journal of Vacuum Science & Technology B*, vol. 9, pp. 1421–1432, 1991.

[140] C. Constantine, D. Johnson, S. J. Pearton, U. K. Chakrabarti, A. B. Emerson, W. S. Hobson, and A. P. Kinsella, "Plasma etching of III-V semiconductors in $CH_4/H_2/Ar$ electron cyclotron resonance discharges," *Journal of Vacuum Science & Technology B*, vol. 8, pp. 596–606, 1990.

[141] C. Constantine, C. Barratt, S. J. Pearton, F. Ren, and J. R. Lothian, "Smooth, low-bias plasma etching of InP in microwave $Cl_2/CH_4/H_2$ mixtures," *Applied Physics Letters*, vol. 61, pp. 2899–2901, 1992.

[142] J. W. McNabb, H. G. Craighead, H. Temkin, and R. A. Logan, "Anisotropic reactive ion etching of InP in methane/hydrogen based plasmas," in *Electron, Ion and Photon Beams*, New York, NY, 1991.

[143] A. Matsutani, F. Koyama, and K. Iga, "Measurement of sidewall roughness of InP etched by reactive ion beam etching," *Japanese Journal of Applied Physics*, vol. 33, pp. 6737–6738, 1994.

[144] A. Matsutani, F. Koyama, and K. Iga, "Surface temperature increase in reactive ion beam etch and improvement of profiles by multistep etching," *Japanese Journal of Applied Physics*, vol. 34, pp. 2053–2054, 1995.

[145] A. Matsutani, F. Koyama, and K. Iga, "Plasma characterization in chlorine-based reactive ion beam etching and chemically assisted ion beam etching," *Japanese Journal of Applied Physics*, vol. 37, pp. 2747–2751, 1998.

[146] A. Matsutani, F. Koyama, and K. Iga, "Low bias voltage dry etching of InP by inductively coupled plasma using $SiCl_4/Ar$," *Japanese Journal of Applied Physics*, vol. 37, pp. 6655–6656, 1998.

[147] A. Matsutani, H. Ohtsuki, F. Koyama, and K. Iga, "Vertical and smooth etching of InP by Cl_2/Xe inductively coupled plasma," *Japanese Journal of Applied Physics*, vol. 38, pp. 4260–4261, 1999.

[148] A. Matsutani, H. Ohtsuki, F. Koyama, and K. Iga, "Plasma diagnostics in inductively coupled plasma etching using Cl_2/Xe," *Japanese Journal of Applied Physics*, vol. 39, pp. 1435–1436, 2000.

[149] A. Matsutani, H. Ohtsuki, F. Koyama, and K. Iga, "Emission spectrochemical analysis in dry etching process of InP by Cl_2 inductively coupled plasma," *Japanese Journal of Applied Physics*, vol. 39, pp. 6109–6110, 2000.

[150] A. Matsutani, H. Ohtsuki, S. Muta, F. Koyama, and K. Iga, "Mass effect of etching gases in vertical and smooth dry etching of InP," *Japanese Journal of Applied Physics*, vol. 40, pp. 1528–1529, 2001.

[151] J. E. Schramm, D. I. Babic, E. L. Hu, J. E. Bowers, and J. L. Merz, "Anisotropy control in the reactive ion etching of InP using oxygen in methane/hydrogen/argon," in *Indium Phosphide and Related Materials*, Santa Barbara, CA, 1994.

[152] J. E. Schramm, D. I. Babic, E. L. Hu, J. E. Bowers, and J. L. Merz, "Fabrication of high-aspect-ratio InP-based vertical-cavity laser mirrors using $CH_4/H_2/O_2$/Ar reactive ion etching," *Journal of Vacuum Science & Technology B*, vol. 15, pp. 2031–2036, 1997.

[153] B. C. Qiu, B. S. Ooi, A. C. Bryce, S. E. Hicks, C. D. W. Wilkinson, N. M. De La Rue, and J. H. Marsh, "Low damage reactive ion etching process for fabrication of ridge waveguide lasers," in *Indium Phosphide and Related Materials*, Boston, MA, 1997.

[154] Y. Feurprier, C. Cardinaud, and G. Turban, "Surface modification and etch product detection during reactive ion etching of InP in CH_4-H_2

plasma," in *European Sectional Conference on Atomic and Molecular Physics of Ionized Gases*, Poprad, Slovakia, 1996.

[155] Y. Feurprier, C. Cardinaud, and G. Turban, "Influence of the gas mixture on the reactive ion etching of InP in CH_4-H_2 plasmas," *Journal of Vacuum Science & Technology B*, vol. 15, pp. 1733–1740, 1997.

[156] Y. Feurprier, C. Cardinaud, B. Grolleau, and G. Turban, "Etch product identification during CH_4-H_2 RIE of InP using mass spectrometry," *Plasma Sources, Science and Technology*, vol. 6, pp. 561–568, 1997.

[157] Y. Feurprier, C. Cardinaud, B. Groelleau, and G. Turban, "Proposal for an etching mechanism of InP in CH_4-H_2 mixtures based on plasma diagnostics and surface analysis," *Journal of Vacuum Science & Technology A*, vol. 16, pp. 1552–1559, 1998.

[158] Y. Feurprier, C. Cardinaud, and G. Turban, "X-ray photoelectron spectroscopy damage characterization of reactively ion etched InP in CH_4-H_2 plasmas," *Journal of Vacuum Science & Technology B*, vol. 16, pp. 1823–1832, 1998.

[159] B. E. Little and S. T. Chu, "Theory of polarization rotation and conversion in vertically coupled microresonators," *IEEE Photonics Technology Letters*, vol. 12, pp. 401–403, 2000.

[160] B.-T. Lee, D.-K. Kim, and J.-H. Ahn, "Observation of oxide films on CH_4H_2 reactive ion etch processed InP mesa sidewalls and surfaces," *Semiconductor Science and Technology*, vol. 11, pp. 1456–1459, 1996.

[161] B. A. Cruden, M. V. V. S. Rao, S. P. Sharma, and M. Meyyappan, "Detection of chamber conditioning by CF_4 plasmas in an inductively coupled

plasma reactor," *Journal of Vacuum Science & Technology B*, vol. 20, pp. 353–363, 2002.

[162] Z. Xiao and B. Nilsson, "Good selectivity between a NiCr mask and GaAs and AlGaAs by chemically assisted ion beam etching with Cl_2 gas," *Journal of the Electrochemical Society*, vol. 138, pp. 3086–3089, 1991.

[163] J. R. Lothian, F. Ren, and S. J. Pearton, "Mask erosion during dry etching of deep features in III-V semiconductor structures," *Semiconductor Science and Technology*, vol. 7, pp. 1199–1209, 1992.

[164] S. J. Pearton, U. K. Chakrabarti, F. Ren, C. R. Abernathy, A. Katz, W. S. Hobson, and C. Constantine, "New dry-etch chemistries for III-V semiconductors," *Materials Science & Engineering B*, vol. B25, pp. 179–185, 1994.

[165] B.-T. Lee, T. R. Hayes, P. M. Thomas, R. Pawelek, and J. Sciortino, P. F., "SiO_2 mask erosion and sidewall composition during CH_4-H_2 reactive ion etching of InGaAsP/InP," *Applied Physics Letters*, vol. 63, pp. 3170–3172, 1993.

[166] J. W. Lee, R. V. Crockett, and S. J. Pearton, "Comparison of masking materials for high microwave power $CH_4/H_2/Ar$ etching of III-V semiconductors," *Journal of Vacuum Science & Technology B*, vol. 14, pp. 1752–1757, 1996.

[167] Y. H. Qian, M. Owen, A. C. Bryce, J. H. Marsh, C. D. W. Wilkinson, R. V. Penty, I. H. White, S. Perrin, D. Drogers, and H. Robertson, "Process development on the monolithic fabrication of an ultra-compact 4×4 optical switch matrix on InP-InGaAsP material," in *Indium Phosphide and Related Materials*, Boston, MA, 1999.

[168] J. R. Lothian, J. M. Kuo, F. Ren, and S. J. Pearton, "Plasma and wet chemical etching of $In_{0.5}Ga_{0.5}P$," *Journal of Electronic Materials*, vol. 21, pp. 441–445, 1992.

[169] M. W. Pruessner, R. Grover, L. C. Calhoun, and R. Ghodssi, "Development of InP-based test structures for optical MEMS applications," in *International Semiconductor Device Research Symposium*, Washington, DC, 2001.

[170] M. W. Pruessner, T. King, D. P. Kelly, R. Grover, L. C. Calhoun, and R. Ghodssi, "Mechanical property measurement of InP-based MEMS for optical communications," *Journal of Sensors and Actuators A*, vol. 105, pp. 190–200, 2003.

[171] S. R. Sakamoto, C. Ozturk, Y. T. Byun, J. Ko, and N. Dagli, "Low-loss substrate-removed (SURE) optical waveguides in GaAs-AlGaAs epitaxial layers embedded in organic polymers," *IEEE Photonics Technology Letters*, vol. 10, pp. 985–987, 1998.

[172] P. P. Absil, *Microring resonators for wavelength division multiplexing and integrated photonics applications*, Ph. D. thesis, University of Maryland, College Park, 2000.

[173] J. E. Heebner, *Nonlinear Optical Whispering Gallery Microresonators for Photonics*, Ph. D. thesis, University of Rochester, 2003.

[174] T. A. Ibrahim, *Nonlinear optics with micro-rings*, Ph. D. thesis, University of Maryland, College Park, 2003.

[175] R. Williams, *Modern GaAs Processing Methods*, Artech House, Boston, MA, 1990.

[176] J. E. Zucker, I. Bar-Joseph, G. Sucha, U. Koren, B. I. Miller, and D. S. Chemla, “Electrorefraction in GaInAsP/InP multiple quantum well heterostructures,” *Electronics Letters*, vol. 24, pp. 458–460, 1988.

[177] M. J. Bloemer and K. Myneni, “Electro-optic properties near the absorption edge of GaAs/AlGaAs multiple-quantum-well waveguides,” *Journal of Applied Physics*, vol. 74, pp. 4849–4859, 1993.